Development of Novel Photocatalysts for Solar Hydrogen Production.

By

Craig D. Morton

BSc. (Hons), AMRSC

A thesis submitted in partial fulfilment of the requirements of the University of Greenwich for the degree of Doctor of Philosophy

March 2012

University of Greenwich

School of Science

Medway Campus

Chatham Maritime

Kent, ME4 4TB

DECLARATION

I certify that this work has not been accepted in substance for any degree, and is not concurrently being submitted for any degree other than that of Doctor of Philosophy being studied at the University of Greenwich. I also declare that this work is the result of my own investigations except where otherwise identified by references and that I have not plagiarised the work of others.

..... (Candidate)
(Craig D. Morton)

.....
(Date)

..... (Supervisor)
(Dr. Bruce D. Alexander)

.....
(Date)

..... (Supervisor)
(Dr. Alexander D. Coutroubis)

.....
(Date)

ABSTRACT

Photocatalysts, typically nanoparticulate semiconductors, can be used to split water into hydrogen and oxygen. If solar light is used for this, it opens the possibility of a renewable source of hydrogen. However, extension of photocatalytic response into the visible region of the solar spectrum is required. A new visible light activated photocatalyst is reported herein.

Iron vanadate, $FeVO_4$, was first synthesised using a low-temperature, aqueous precipitation reaction. The material prepared was found to be predominantly amorphous and required thermal treatment. The resultant material was characterised using XRD, SEM, IR spectroscopy, Raman spectroscopy and magnetic susceptibility measurements. Materials annealed above 600 °C were found to consist mainly of $FeVO_4$, although traces of hematite were found. Diffuse-reflectance UV spectroscopy and subsequent Tauc plots revealed a band gap of *ca.* 2.00 eV corresponding to an indirect transition. Photocurrent-voltage characteristics recorded under simulated solar illumination indicate that photocurrents are sensitive to annealing temperature and the thickness of the deposit. However, although photocurrent-voltage plots show that electrodes prepared from a suspension of nanoparticulate $FeVO_4$ powders were photo-responsive, these electrodes were found to be mechanically unstable.

Films were prepared directly onto the electrode by using a sol-gel approach. Raman spectroscopy, XRD and diffuse-reflectance UV-visible spectroscopy has revealed the electrode films to be crystalline in nature, significantly more stable, with an indirect band gap in the visible region of 2.00 eV. Higher photocurrent densities were observed for the sol-gel prepared electrodes compared to those deposited from aqueous suspensions of pre-formed powders. It was determined that these photocurrents were dependant on film thickness, annealing time and temperature, and sol pH.

ACKNOWLEDGEMENTS

There are many people who I wish to thank for making this PhD completion successful. First of all I wish to thank Mum, Dad, Paul, Chloé, Amber as well as the rest of my family for all of their endless love, support and help during this project period. Words are not enough for how thankful I will always be.

Additional thanks goes to Naomi, for her endless support during this PhD, listening to practise presentations, and just always being there for me. I would also like thank Kenneth, Hilary and Sophie, for taking me into their home during parts of my project, I am eternally grateful for their hospitality, kindness and support.

Huge thanks goes to Bruce Alexander for having the confidence in me to appoint me for this studentship. His expertise, humour, dedication, enthusiasm and guidance has helped me work through this project and also helped me to enjoy it too, it has been a pleasure to work with him. Thanks must also go to my 2nd supervisors during this project, Dr Michael Thomas and Dr Alec Coutroubis, for their additional guidance, expertise and enthusiasm for this project. I am grateful and honoured to have had them in the team.

Thanks also go to Dr Ian Slipper, the Laboratory technical staff, and the School of Engineering for all of their support, patience and assistance during this project, as well as Imperial College staff for their kind support and IPCE analysis.

And lastly but by no means least, I wish to thank all of the PhD and postdoctoral students within the School of Science and NRI who have come and gone during this project for all of their support, humour, parties, food, drinks and memorable times.

DEDICATION

This thesis is dedicated to my family and friends, for all of their endless love and support.

CONTENTS

LIST OF FIGURES

LIST OF TABLES

LIST OF ABBREVIATIONS

Acac	-	acetylacteonate
AM	-	Air mass
AE	-	Auger electrons
BSE	-	Back-scattered electrons
E_g	-	Band gap
CVD	-	Chemical vapour deposition
DMF	-	Dimethylformamide
EM	-	Electron microscopy
EDX	-	Energy-dispersive x-ray spectroscopy
$E_{p,d}$	-	Free enthalpy of oxidation
$E_{n,d}$	-	Free enthalpy of reduction
FTO	-	Fluorine-doped tin oxide
GC	-	Gas chromotography
IR	-	Infrared
ICE	-	Internal combustion engine
IPCE	-	Incident photon to current efficiency
PEMFC	-	Polymer electrolyte membrane fuel cell
PEC	-	Photo-electrochemistry
PES	-	Photo-electron spectroscopy
PV	-	Photovoltavic
PVD	-	Physical vapour deposition
PVDF	-	Polyvinylidene fluoride
rpm	-	rotations per minute
SCE	-	Saturated calomel electrode
SEM	-	Scanning electron microscopy

SE	-	Secondary electrons
SOFC	-	Solid oxide fuel cell
UV	-	Ultraviolet
Vis.	-	Visible
w/w	-	weight/weight
w/v	-	weight/volume
XPS	-	X-ray photo-emission spectroscopy
XRD	-	X-ray diffraction

1 – INTRODUCTION

The aim of this project is to develop a novel visible-light activated photocatalyst, namely iron vanadate, for solar hydrogen production through the photolysis of water.

1.1 – Energy

1.1.1 – Energetic problems

As the developed world becomes more populated and that population depends more on technology, energy demand is set to rise. This is illustrated by the rapid growth in energy consumption throughout the world. At the start of the millennium, global energy consumption was estimated to be at around 13 TW.[1, 2] This value is expected to double to almost 27 TW by 2050.[2] The majority of the current demand (around 85 %) is being met by fossil fuels,[3] such as coal and oil, which are decreasing in availability. It is clear from these two points alone that other energy sources are needed, not only to satisfy this increasing demand, but also to replace those sources which are depleting.

1.1.2 – Renewable energy

Another potential problem in the current age is that of global warming which is commonly accepted to be linked to an increase in the levels of greenhouse gases in the atmosphere. Although there are many greenhouse gases, water included, carbon dioxide attracts the most attention as since the 18th century and the time of the industrial revolution, CO_2 emissions have increased phenomenally, causing a 25 % increase in atmospheric levels.[4] It is being produced constantly from combustion of fossil fuels in power stations and in transport. Thus, there is a clear incentive for the development of processes and energy carriers that have reduced CO_2 emissions, as evidenced by UK government legislation as well as EU initiatives such as the 2020 target.

Alternatives have been investigated and implemented on smaller scales over the years. Various methods have used the naturally occurring phenomena, for example, wind, tidal or geothermal. However, due to comparatively low energy production or high cost, such methods can only provide a small percentage of the energy demand.[1] A larger scale and

more energy efficient process of energy production is that of nuclear energy. This, however, clearly has environmental implications of its own, namely the disposal of spent uranium and plutonium fuel, currently achieved by burying underground. There is also the high risk of operating nuclear reactors, highlighted by the Chernobyl disaster in Ukraine in 1986[5] and the Fukushima plant in Japan, following the 2011 earthquake.

1.2 – Hydrogen

Hydrogen has been identified as a possible clean alternative fuel to potentially lessen our dependence on fossil fuels,[6] due to the fact that its combustion only produces water, therefore rendering it carbon neutral.

$$H_2 + \tfrac{1}{2}O_2 \rightarrow H_2O \qquad (\Delta H = -286\ kJ) \qquad \text{(Equation 1.1)}$$

Hydrogen has a high calorific value, and this reaction does not produce any by-products. To use hydrogen as a fuel, it is usually implemented into a fuel cell. Simply burning hydrogen as a fuel leads to very high temperatures that, for example, standard combustion engines may have problems with and it is more practical to use hydrogen as a feed in fuel cells.

1.2.1 – Fuel cells

A fuel cell is an electrochemical cell in which the chemical energy of a fuel is converted directly into electrical energy[7] and the concept was first discovered over 160 years ago.[8] There are various types of fuel cells,[8] operating at high temperatures (*e.g.* molten carbonate fuel cell, solid oxide fuel cell at 600-700 °C and 700-1000 °C respectively) and low temperatures (*e.g.* proton exchange membrane fuel cell at 80-90 °C), using a number of fuels such as methanol, and producing varying electrical values. Despite these differences, they are generally laid out in the same way, containing an anode and cathode separated by an electrolyte. The anode and cathode are the electrodes used for the reactions in the fuel cell, an example is shown in figure 1.1.

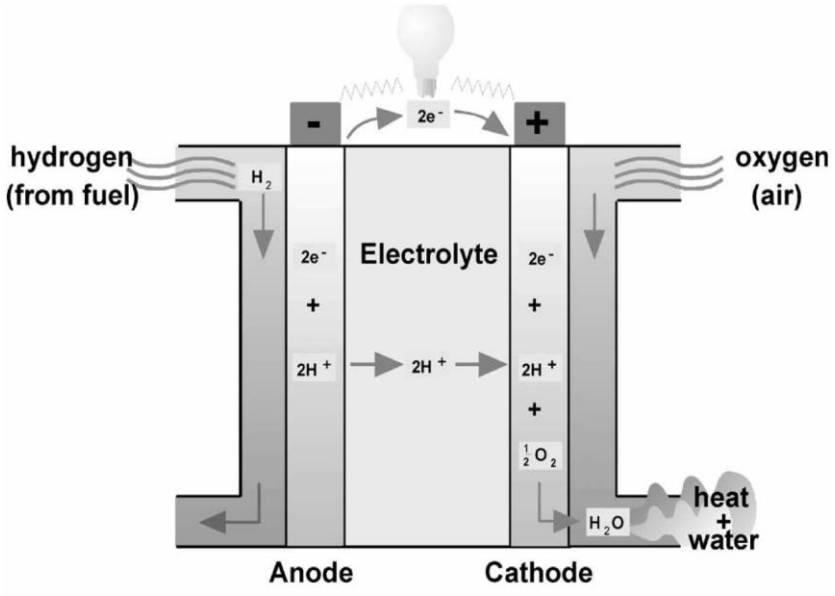

Fig. 1.1 – Schematic of a hydrogen fuel cell.[9]

When using hydrogen, a polymer exchange membrane fuel cells (PEMFCs) or solid oxide fuel cells (SOFCs) are often used, the schematic of which are shown in fig. 1.1. This fuel cell works on the basis of a simple redox reaction, described below in equations 1.2 and 1.3.

$$H_2 \rightarrow 2H^+ + 2e^- \quad \text{(Equation 1.2)}^{[10, 11]}$$

$$2e^- + 2H^+ + \tfrac{1}{2}O_2 \rightarrow H_2O \quad \text{(Equation 1.3)}^{[10, 11]}$$

As the hydrogen gas is fed in, the platinum coated anode catalyst catalyses its conversion protons and electrons. The electrolyte, in this case typically a polymer such as Nafion©,[12] then allows proton conduction to the cathode. At the same time, the electrolyte acts as an insulator, preventing short circuit, therefore creating a current. The electrons flow to the cathode where they recombine with the hydrogen ions and with oxygen supplied from air to form water. Although the theoretical fuel cell efficiency is 80-85%,[10] current PEM fuel cells have been known to produce efficiencies of 30-50%,[13, 14] which are still more efficient than internal combustion engines (ICE).[15, 16, 17]

However, Honda report that their hydrogen powered car produced an efficiency of *ca.* 60%, in converting the chemical energy into power.[18] Two major problems with using hydrogen as a fuel are the storage and production of the hydrogen.

1.2.2 – Hydrogen Storage.

Although hydrogen has about a quarter of the energy-per-volume density of that of petrol,[4, 16, 19] it has almost treble the energy-per-weight,[16, 20] (shown in table 1.1).

Energy source	Energy / WhL^{-1}	Energy / $Whkg^{-1}$
Gaseous H_2	579	33566
Liquid H_2	2368	33566
petrol	9057	12329

Table 1.1 – Comparison of energetic values of hydrogen and petrol.[21]

For this reason, a larger volume of hydrogen is needed in order to produce the same amount of energy as petrol, and therefore, storage of the hydrogen is a key challenge in current technologies. A wide range of methods have been researched in order to try and overcome this by reducing the volume required, either by increasing the pressure inside the storage vessel to compress the gas, or by using liquid hydrogen. However, both of these methods are difficult, as both require the use of highly pressurised containers.[7]

Storage media have been developed in order to improve the storage efficiencies. Metal hydrides, *e.g.* $NaAlH_4$, have the ability to absorb and release hydrogen,[4] and have been researched as a possible storage medium as they can store a high weight percent of hydrogen[22] of up to 18.5 %.[4] However, one drawback currently, is that a lot of energy is required to release the hydrogen for its application,[22] around 40 $kJmol^{-1}$, although some have suggested this is a positive safety feature.[4] Ammonia, NH_3, has also been investigated as a possible storage medium for H_2 due to the fact that the hydrogen can be released using catalytic reformation. Ammonia has been shown to be a promising solution on a small scale, as it has a high energy density.[23] Ammonia can also benefit from being amenable to the use of existing infrastructure for production and transport. However, problems still arise as the ammonia has to be held under high pressure and is toxic.[4] Formic acid has recently been investigated as a possible storage material, using

ruthenium catalysts to release the H_2.[24] Other organic compounds such as methanol have been investigated to release hydrogen through decomposition, however this requires temperatures above 250 °C and produces CO.[4] As well as the storage medium being researched, the vessel coating itself can also be modified. Nanostructured materials in the form of nanofibres and nanotubes have been investigated due to fact they can increase the surface area inside the vessel.[4] They are thought to expand on a micro-scale during the uptake of hydrogen, increasing its storage capacity.[4] However, the aspect ratio of *ca.* 1000 could cause a reduction in uptake efficiency, due to the long thin tubes not being completely saturated, leading to metal catalysts being required to increase it. Other porous frameworks such as zeolites are also under investigation for possible hydrogen storage,[4] but as of yet, no definite resolution for hydrogen storage has been determined. Switching all cars to fuel cell operated systems however, will not significantly contribute to CO_2 reduction unless a carbon neutral method of hydrogen production is implemented.[4]

1.2.3 – Hydrogen Production

Of the many routes to hydrogen production there are currently available, steam reformation from hydrocarbons (mostly natural gas) using a nickel-based catalyst is the most commonly employed.[4, 25, 26]

$$CH_4 + H_2O \rightarrow CO + 3H_2 \quad (\Delta H = +206\ kJmol^{-1}) \text{ (Equation 1.4)}^{25}$$

CO may further be converted to CO_2 during the water gas shift reaction: -

$$CO + H_2O \rightarrow CO_2 + H_2 \quad (\Delta H = -41.1\ kJmol^{-1}) \text{ (Equation 1.5)}^{25}$$

Although this process is widely used, it requires highly elevated temperatures of around 900 °C,[4, 27] which is not energy efficient. Nor does the production of the CO_2 and CO coincide with the 'clean fuel' objective.[28] Although the possibility of using solar concentrators to provide the thermal energy required for steam reformation has been investigated,[4] the process still requires a finite feedstock, *e.g.* CH_4. Other methods have been researched for hydrogen production. In the last decade, algae has been investigated

as a possible source. Algae bioreactors produce hydrogen,[29] when not exposed to sulphur.[29, 30] However currently only 28% of the products are as hydrogen (others being glucose), and photosynthesis itself is only around 1% efficient with available photons,[31] maximum in plants being 6.7 %.[1] Use of the iodine-sulphur cycle, in which HI is formed and dissociates to form I_2 and H_2, has a number of problems including the production of H_2SO_4 and also the release of sulphur dioxide into the atmosphere. High temperatures are also required.[4]

Given the natural abundance of water, it is therefore an ideal source. Direct electrolysis of water can be used to split water into oxygen and hydrogen, however, a large amount of electrical energy is required (1–10 kAm^{-2}, 4–4.9 kWh m^{-3}),[6] and therefore more energy is required to generate hydrogen than would be supplied by its combustion. Thermal decomposition of water is particularly unfavourable as it requires extremely high temperatures of up to 3000 K, however, attempts have been made to reduce this to *ca.* 800 °C using heterogeneous catalysts.[32] An alternative to this is the use of photocatalysts.

1.3 – Photocatalysis

The earliest work that suggested photocatalytic behaviour can be dated back to the 1920s, when it was discovered that titania was partially reduced under illumination with sunlight in the presence of an organic compound such as glycerol, and turned from white to grey, blue or black.[33] This showed that these materials were responding to light and changing their electronic structure accordingly. Photocatalysts have been researched more and more in the last 40 years due to the prospective applications in sustainable hydrogen production,[34] first reported by Fujishima and Honda in 1972,[35] and in the degradation of organic matter.[33] There are now more than 130 reported photocatalytic materials and derivatives, although the most widely reported and researched is TiO_2.[36]

1.3.1 – Principles

Photocatalysts are typically semiconductor materials and are dependent on the band structure of semiconductors. The valence and conduction bands of a semiconductor are formed as molecular orbitals overlap as more molecules come together to form clusters, and then particles, shown in figure 1.2.

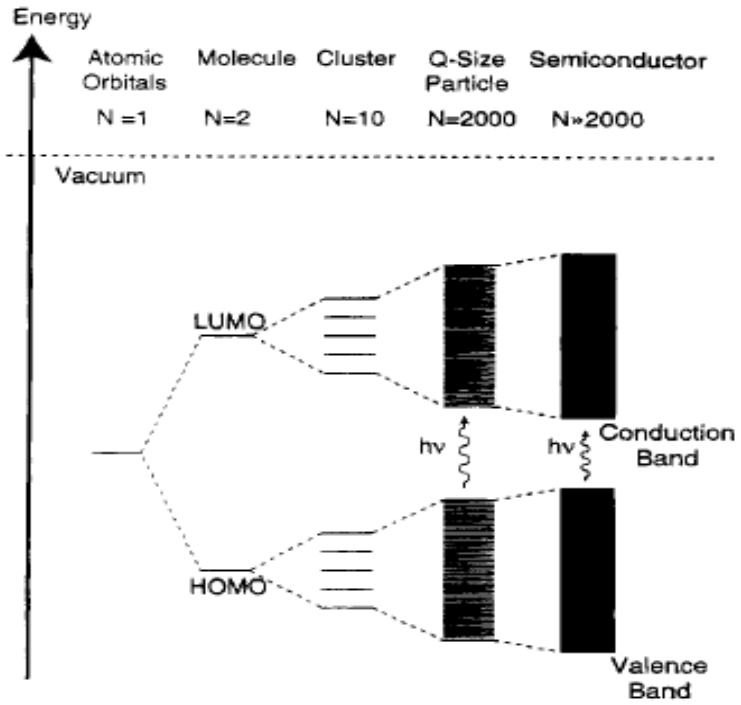

Fig. 1.2 – Schematic diagram showing the relationship of valence and conduction bands to molecular orbitals.[37]

The difference in energy between the conduction and valence bands is known as the band gap and an electron can be promoted from the valence band to the conduction band following an optical transition if a photon of energy equal (or greater) than the band gap is absorbed. Photocatalytic reactions occur as when a photocatalytic material absorbs a photon, an electron is promoted from valence band to the conduction band. When this occurs, a positive electron vacancy (hole, h^+) is left in the valance band.

The electrons and holes can then migrate to the surface of the catalyst and undergo oxidation and reduction. For example, in the degradation of organic matter, and for hydrogen production, shown below:

$$H_2O + 2\,h^+ \rightarrow 2\,H^+ + \tfrac{1}{2}\,O_2 \qquad \text{(Equation 1.6)}$$

$$2\,H^+ + 2\,e^- \rightarrow H_2 \qquad \text{(Equation 1.7)}$$

This can be summarised as:

$$2h\nu + H_2O \rightarrow H_2 + \tfrac{1}{2}\,O_2 \qquad \text{(Equation 1.8)}$$

1.3.2 – Applications

As described above, photocatalysts can be used in hydrogen production by absorbing solar energy to split water into oxygen and hydrogen, but photocatalysts also have other applications. For example, antibacterial treatments[38] in the degradation of organic matter. Photocatalysts are also used in water purification, using other similar methods to degrade the organic species.[39, 40] Titanium dioxide has been reported to have been incorporated into operating theatre tiles in hospitals, as it can reduce absorbed bacteria.[41] Similarly, it has been used in self-cleaning glass and mirrors[33] *e.g.* the glass roof at St. Pancras Station, London. This is beneficial in glass because when it is cleared of organic matter, moisture droplets on the surface can spread out thereby preventing misting.[42]

1.4 – Suitability of a photocatalyst

1.4.1 – Band Positions.

The suitability of a photocatalyst for solar hydrogen production depends on a number of factors. For example, the band positions of the photocatalyst must be in suitable positions, with respect to the electrochemical potentials for hydrogen and oxygen evolution, as demonstrated in fig. 1.3. In order for a reaction to occur with a semiconductor, the potential of the conduction band must be more negative that the

hydrogen evolution potential, and similarly, the potential of the valence band must more positive than the redox couple for oxygen evolution.

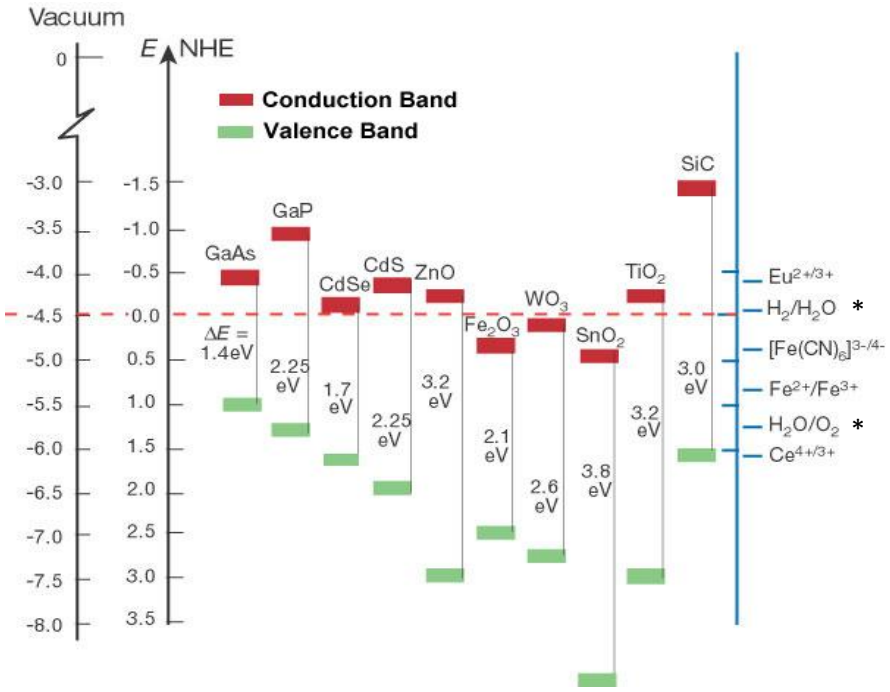

Fig. 1.3 – Band positions of selected semiconductor photocatalysts. Redox potentials are given for comparison.[43]

fig. 1.3 shows that titanium dioxide has bands that are energetically favourable with respect to the oxygen and hydrogen evolution potentials.

However, in contrast, Fe_2O_3 is not ideal for hydrogen production if band energies alone are considered, as its conduction band occurs at a more positive potential than is required for hydrogen evolution, therefore an external bias is required to overcome this. Similarly, GaAs has a valence band at a more negative potential than that required for the oxygen evolution reaction.

1.4.2 – Band gap energy

Although titanium dioxide is currently the most commonly used photocatalysts, one major hindrance is its comparatively large band gap, which as can be seen from fig. 1.3, is 3.2 eV. The thermodynamic potential required to electrolyse water is 1.23 eV,[35] with

reference to a normal hydrogen electrode. If the band gap of the photocatalyst is too large, it greatly limits the portion of photons in sunlight that can be converted into electrons and holes when the photocatalyst is irradiated. The band gap of 3.2 eV in TiO_2, corresponds to 387 nm in wavelength. This means that in order for water splitting to occur using TiO_2, only high energy photons of 387 nm and below are adequate. Unfortunately, this corresponds to only around 4% of the solar spectrum, and furthermore corresponds only to UV radiation as demonstrated below (fig. 1.4).

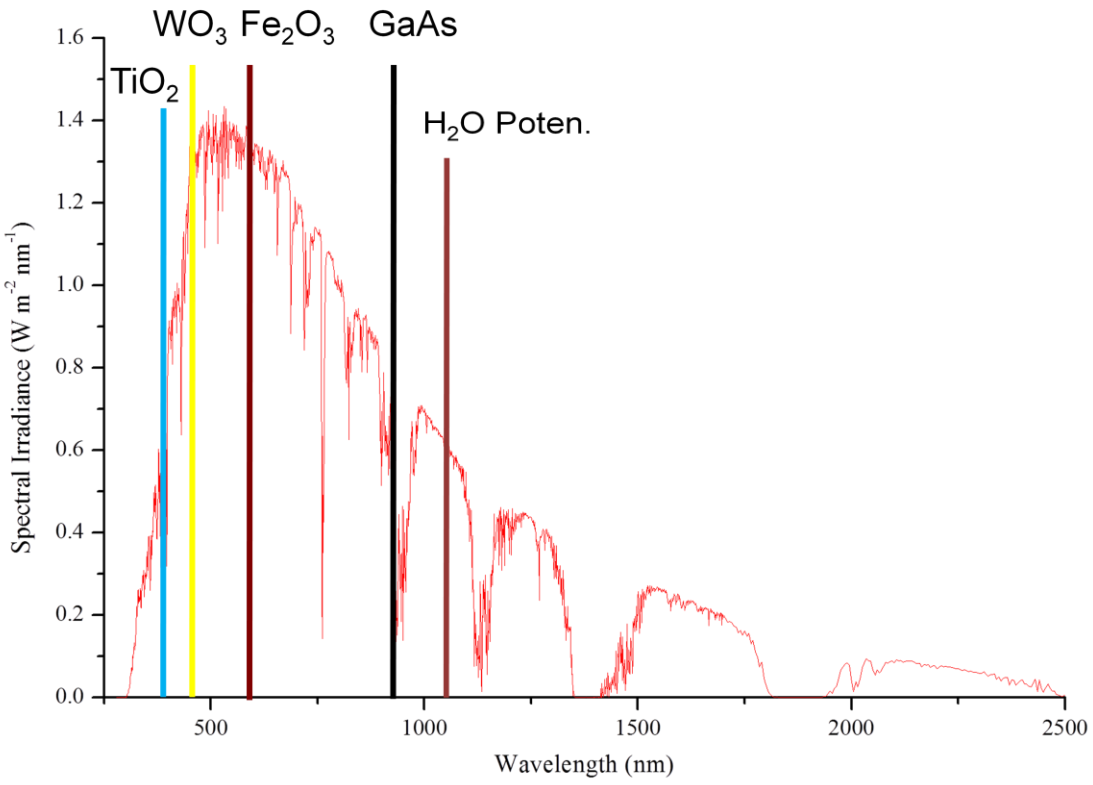

Fig. 1.4 – Typical equatorial solar spectrum.[44] Also shown are the band gaps of some photocatalysts and the thermodynamic splitting potential of water.

It is not just the band gap which dictates if a semiconductor is sufficient for its function, as explained earlier.

1.4.3 – Degradation.

As shown in fig 1.3, a number of semiconductor materials possess band gaps that are sufficiently low to be of interest. Furthermore, their valence and conduction bands suggest favourable thermodynamics for water splitting. Nevertheless, these materials,

such as CdS, are not routinely used for water splitting, as they are unstable under the reaction conditions. There are a number of ways that these instabilities can present themselves, such as degradation, photo-degradation and delamination (on thin films). Degradation and photo-degradation can occur when the material is unstable in the electrolyte, and undergoes corrosion. This is caused by electrochemical processes involving charge transfer at the solid/liquid interface.[26] For stability in the aqueous environment, the free enthalpy of oxidation ($E_{p,d}$) of the material must be greater than the energy of the water oxidation reaction, and the free enthalpy of reduction of the material ($E_{n,d}$) must be lower than the energy of water reduction,[26] as shown in figure 1.5.

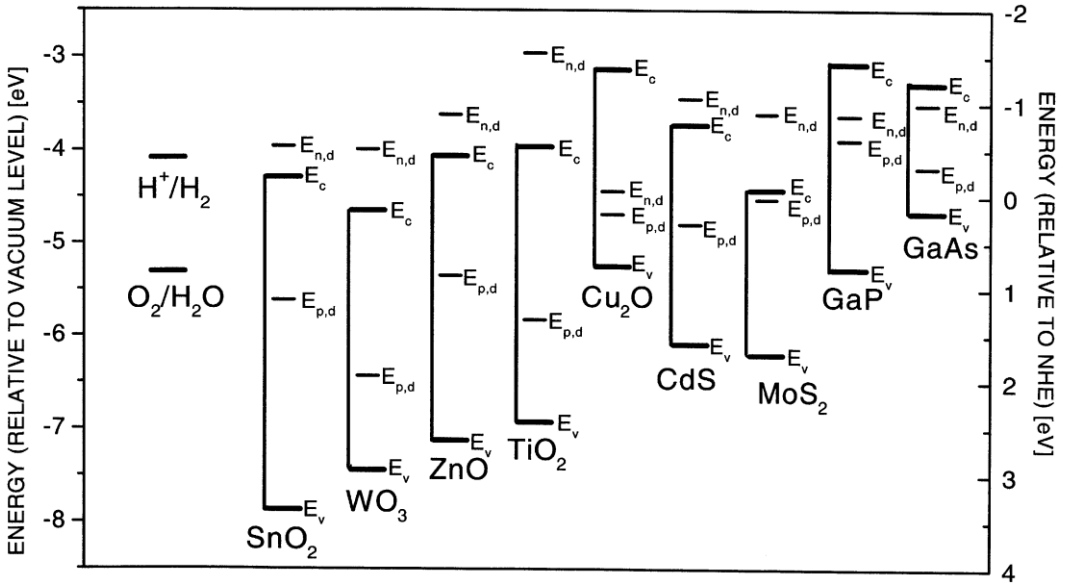

Fig. 1.5 – Position of decomposition potentials with respect to band potions and water splitting potentials of stated materials.[26] Where E_v is the energy of the valence band, E_c is the free energy of the conduction band, $E_{p,d}$ is the enthalpy of oxidation of the material, and $E_{n,d}$ is the free enthalpy of reduction of the material.

Photo-degradation consequently occurs in materials such as CdS, ZnO[45] and GaAs (shown in equation 1.9), while materials such as SnO_2, WO_3 and TiO_2 are much more resistant to corrosion.

$$GaAs + 6\,H_2O + 6\,h^+ \rightarrow Ga(OH)_3 + As(OH)_3 + 6\,H^+ \quad \text{(Equation 1.9)}$$

Delamination occurs when the material comes off of the electrode substrate due to poor mechanical adhesion to a substrate. This is more an intrinsic property of the semiconductor and can be controlled, or at least mitigated, during the synthesis process.

1.4.4 – Charge generation and recombination.

Not every photon that is incident on a semiconductor is converted to charge carriers, for example, as discussed previously, not all photons are of sufficient energy to generate electron-hole pairs. Another key issue is recombination. Recombination is the process in which the electron and hole recombine with each other due to the fact they are oppositely charged and so attract each other. This can happen in two ways, they can either recombine before reaching the catalyst surface (volume or bulk recombination), or they recombine at the surface before they can cross the interface into the surrounding medium (surface recombination), due to the fact that surface reactions are not instantaneous. This is shown in fig. 1.6.

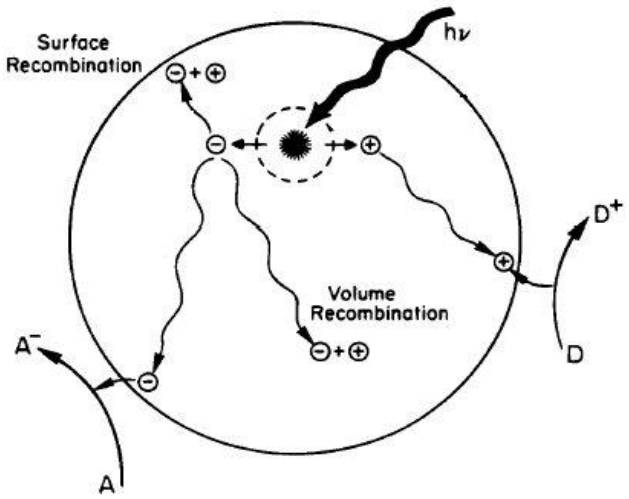

Fig. 1.6 – Different recombination processes and surface reactions.[46]

Incident-photon-to-current efficiency (IPCE) is a method of determining the current-producing efficiency of the catalyst. It indicates how many electrons per photon adsorbed, generate current.

There are a number of methods to limit the effect of recombination. For example, a decrease in particle size reduces the distance in which the generated charges need to

migrate to reach the surface of the catalyst to react. Although this greatly reduces the likelihood of volume recombination, it does not reduce surface recombination. One way to do this is to add additional catalysts to the surface, which increases the rate of surface reactions, so the charges can react before they can recombine.

1.4.5 – Physical nature of catalyst.

Once the photophysical and chemical properties of a photocatalyst material have been considered, it remains to decide the physical form the photocatalyst might be employed, for example photolysis of water. There are two principal ways of using a photocatalyst: one is in suspensions and slurries, the other is with a catalyst immobilised on a surface and the choice will influence how easy it is to recover catalyst material, the efficiency of its use and how to overcome any problems associated with band positions. With slurries and suspensions, the dispersed catalyst would have a large surface area in direct contact with the reaction medium, however it can be difficult and time consuming to separate. One difficulty arises as when the catalyst is in a suspension: uniform illumination throughout the suspension is difficult, particularly at high catalyst loadings, which would also limit the efficiency of the catalyst as much of the light may be absorbed by the first few micrometers of the reaction suspension. The band positions of the catalyst with respect to the redox potentials involved would also have to be taken into account in order for the reaction to occur. For example, sacrificial agents would be required to allow WO_3 to be used to split water. Without these, electrons would be promoted to the conduction band but would not be able to transfer into the reaction medium due to the unfavourable position of the hydrogen evolution potential.

Immobilised catalysts, such as thin films on an electrode, are easier to separate from a reaction mixture as they are directly attached to a solid electrode, more stable and can be easily moved into a position where photo-illumination is possible. Another advantage of using electrodes is that it increases the choice semiconductor used, limitations relating to unfavourable band energetics can be overcome by applying a bias. For example, polarisation in an electrolyte causes a change on the surface potential of the semiconductor, resulting in band bending.[26] However, drawbacks of electrodes are that they are less efficient due to less surface area, as particle-particle contacts in the film mean that less of the catalyst material is in intimate contact with the surrounding

solution. Immobilised catalysts also exist in materials such self-cleaning glass and mirrors also, by being incorporated into their surface. These functions do not require the removal of the material, but do require that band positions are favourable.

1.5 – Alternative photocatalytic materials

Although there are over 130 known photo-active materials and derivatives,[36] from the discussion above, it is clear that a careful balance must be reached between considerations of stability, optimum band gap and efficiency.[26] This is highlighted by the fact that although TiO_2 continues to be the most publicised and researched photocatalytic material,[34] predominately due to its high corrosion resistance,[26] however, its large band gap, causes inefficient photon absorption. After TiO_2, iron oxide, Fe_2O_3, and tungsten trioxide, WO_3 have received considerable attention. Although Fe_2O_3 and WO_3 have much smaller band edge separations than that of TiO_2, (2.1 and 2.6 eV, respectively),[43] meaning photons in the visible region of the solar light spectrum can be absorbed, the position of their conduction bands make them only suitable for oxygen production,[26] while the former is also susceptible to corrosion[26] and poor charge transport.[47] Most recent research has tried to alter the properties of these materials by changing synthesis conditions and with doping. Changing the synthesis method of the material can modify the morphology of it and possibly increase its stability, and also, by altering properties such as particle size, can increase the efficiency of charge transfer.

Doping of an intrinsic semiconductor, by introducing another element into the structure can affect its photo-electrochemical performance for a number of reasons. Firstly, the addition of these impurities into the structure can interact with band structures, shifting them either positively or negatively (*i.e.* this is not always beneficial). The other way that dopants can affect the photo-electrochemical properties, is that they can act as a source of trapped electrons or holes.

1.5.1 - An alternative visible light-activated catalyst

Iron oxide, Fe_2O_3, has been extensively researched for the role as a water-splitting photocatalyst, and highlights the possibility of being able to utilize a cheap and readily available material. Iron oxide has been previously shown to be stable under controlled pH conditions,[26] and possess a favourable band gap of *ca.* 2.1-2.3 eV,[26, 43, 48] and is consequently, a visible light activated catalyst. Iron oxide however, unfortunately does not undergo hydrogen production without additional bias due to the conduction band being energetically unfavourable with respect to the hydrogen evolution potential.[43] Despite this, numerous research groups continue to research water-splitting abilities of iron oxide, using different synthesis and deposition methods such as spray pyrolysis,[49] sol-gel,[50] chemical vapour deposition,[51] and microwave synthesis[47] producing photon-induced current densities up to 2 $mAcm^{-2}$ using 50 mW light intensity.[51] Iron oxide has been has been identified as a material of interest for tandem cells.[43, 51]

1.5.2 – Tandem cells

There are a number of well-documented photocatalysts, such as Fe_2O_3 and WO_3, which contain suitable band-edge separations for absorbing visible light but possess unfavourable band energetics for hydrogen production, and therefore require an additional bias. Such additional bias can come from the use of a photovoltaic cell[34] (or a semiconductor[52] with a lower band gap) into the photo-electrochemistry system, to form a tandem cell,[34] which will absorb light not absorbed by the photocatalyst,[53] as shown in figure 1.7

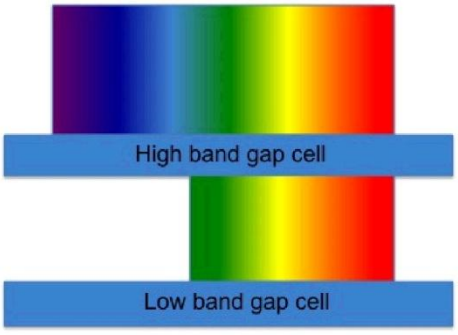

Fig. 1.7 – Light absorbances by layers of the tandem cell.[54]

This additional light absorbance at the photovoltaic cell produces additional photovoltage,[52] which provides the required bias. Conventionally, this is done by

overlaying (stacking) the photocatalyst on top of the photovoltaic material and so exposed to the light. This PEC/PV (photo-electrochemistry/photovoltaic) hybrid cell is then immersed into an electrolyte along with a counter electrode,[52] and exposed to light to induce photocatalytic water splitting.

1.6 – Vanadates.

Vanadium was first found to be present in Mexican ores by Andreas Manuel del Rio in 1801, and it was then detected in Swedish iron by Nils Gabriel Sefstrom in 1831 before finally being identified as a new element and isolated by Henry Enfield Roscoe in 1869.[55] Vanadium can be found in a range of oxidation states including +2 (violet), +3 (green), +4 (blue) and +5 (yellow).[55] Therefore, it has interesting properties, particularly in catalysis,[56] which has been used since the fifties[55] for applications such as dehydrogenation of alkanes,[57] due to the fact that a large variety of different solid structures can be formed.[58]

Some metal vanadates such as bismuth vanadate ($BiVO_4$) and indium vanadate ($InVO_4$) have been identified as having photo-catalytic activity, especially $BiVO_4$, which has been recognized as a strong visible-light photocatalyst for organic pollutant decomposition.[59] $BiVO_4$ has a band gap of 2.4 eV, and its conduction band position is unfavourable for hydrogen production.[60] The use of iron rather than bismuth or indium could not only further lower the band gap, but can also avoid using precious metals such as indium. Previous studies of iron-based binary oxides suggest that iron vanadate is expected to be a photo-electrocatalytically active material.[40, 61]

1.6.1 – Iron Vanadate.

Not much is known about the applications of iron (III) vanadate (V) ($FeVO_4$), with regards to photocatalysts as these have not been reported to date. So far, synthesis of iron vanadate has been at high temperatures, of around 980 °C, by melting and homogenising solutions for around 10 hours,[62] or at lower temperatures of around 70 °C,[58] using a wet-chemical synthesis for 72 hours. Iron vanadate is usually obtained as orange/brown solid.

Four different polymorphs of $FeVO_4$ have been reported in the last fifty years,[63-65] known as type I, II, III and IV. $FeVO_4$-I has a triclinic structure and consists of bent iron oxide chains, containing FeO_6 octahedra and FeO_5 distorted trigonal bipyramidal structures, shown in figure 1.8. These chains are then arranged in layers which are linked by VO_4 tetrahedra.[66] $FeVO_4$-II is thought to have an orthorhombic $CrVO_4$ structure containing FeO_6 octahedra linked by VO_4 tetrahedra,[66] shown in fig. 1.9, $FeVO_4$-III, an orthorhombic α-PbO_2 structure, and $FeVO_4$-IV is shown to have a monoclinic $NiWO_4$ wolframite structure.[62, 66]

It was proposed that these polymorphs transform with increasing temperature and pressure, in the order: I → 10–20 kbar at 800 ˚C → II → 20–80 kbar at 800–1300 ˚C →III → IV.[66, 67]

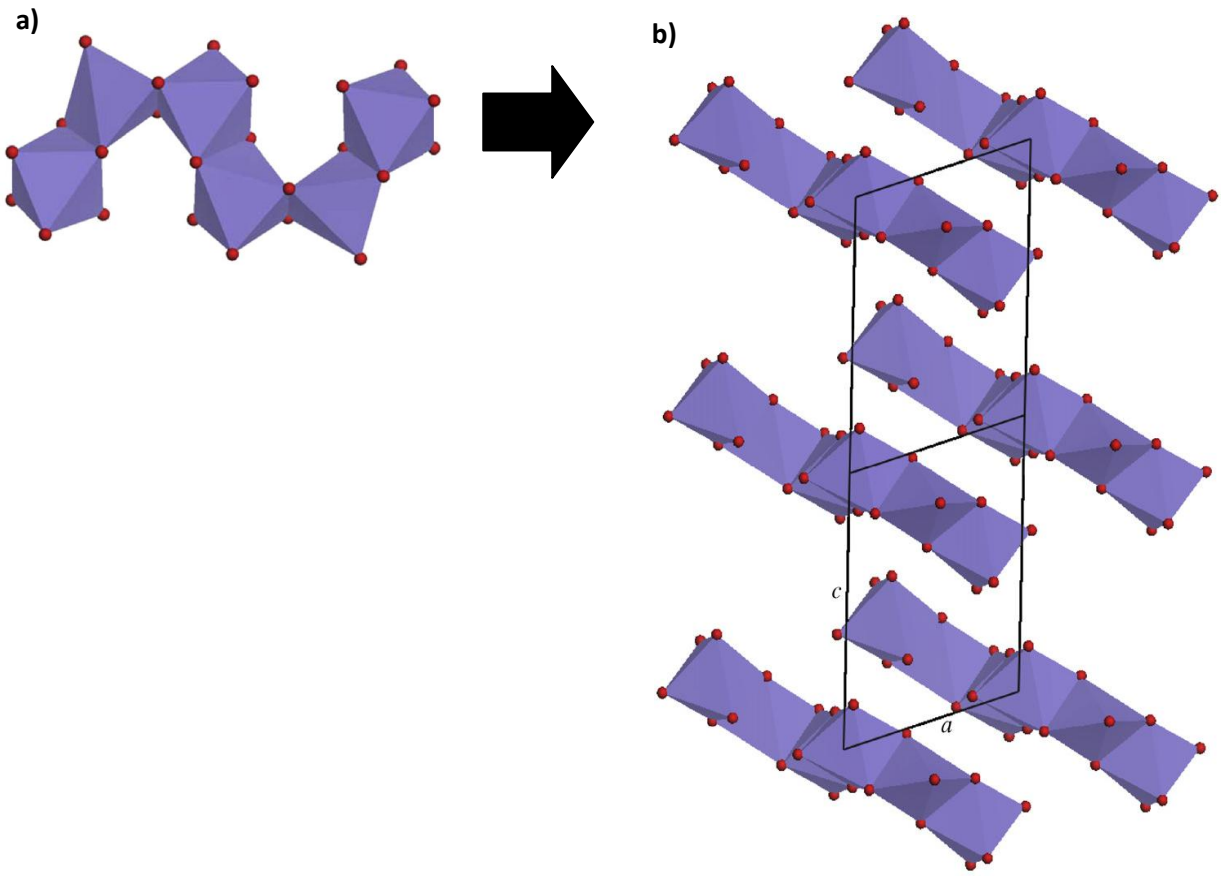

Fig. 1.8 – The two pictures from He *et al*, show the how the iron oxide chains are arranged in $FeVO_4$ - I. 1.8a shows the bent chains containing FeO_6 octahedra and FeO_5 distorted trigonal bipyramids. fig. 1.8b shows how the chains are arranged in their layers which are linked with VO_4 tetrahedra.[62]

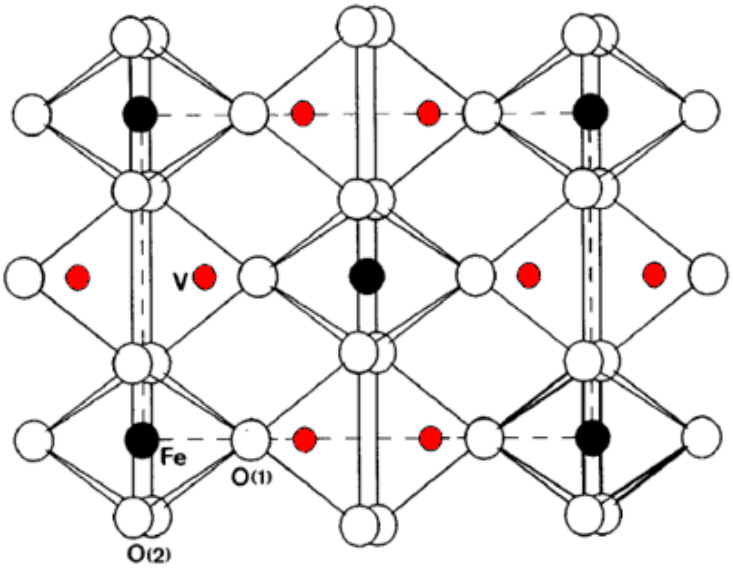

Fig. 1.9 – The schematic structure of $FeVO_4$ – II. The red dots are vanadium atoms, the larger black dots are iron atoms and the white circles are oxygen atoms.[66]

1.6.2 – Applications.

Currently, there are few reports of applications of iron vanadate. Iron vanadate already has an application in catalysis, in the oxidation of hydrocarbons.[68] $FeVO_4$ has also been used as a gas sensor material for detecting traces of H_2S in air environment.[57] This works as the $FeVO_4$ semiconductor chemisorbs oxygen from the air, which reduces its electrical conductivity.[69] When it is exposed to H_2S, it reacts with the chemisorbed oxygen and releases electrons, increasing the conductivity in the sensor.[69]

More recently, iron vanadate has be proposed as a suitable material as a anode for rechargeable lithium batteries,[57] with Denis *et al.*[70] showing promising results as the lithium reacts with large amounts of vanadium at a low mean voltage. However, one problem is that during the discharge, the material becomes amorphous.[70] Iron vanadate has also been investigated for other catalytic reactions, such as in the degradation of orange II,[61, 71] however, none of these processes concern the use of photocatalysis.

1.7 – Catalyst synthesis.

1.7.1 – Aqueous precipitation synthesis

Material may first be prepared in powder or nanoparticulate form before being deposited onto a substrate. Controlled precipitation of iron vanadate out of an aqueous reaction mixture, when solutions contain soluble salts, it allows formation of a typically amorphous form an insoluble product (precipitate).[72] Agitation and often heating are implemented to ensure thorough mixing to maximise product yield. This solid can then be dispersed in a suitable solvent to form a suspension of the powder, ready to apply as a thin film.

Advantages of this method include the ability to analyse and characterise the product quality, morphology and yield before application to the electrode or slurry set-up. This gives the user the ability to change the properties of the powder by easily changing the solution parameters or by changing the annealing temperature and time, before implementing them into the system. Disadvantages of this method can include long synthesis times (*e.g.* in the case of current literature, three days) and that the method does not typically produce crystalline products.

1.7.2 – Sol-gel synthesis

Sol-gel synthesis is defined as the formation of a stable suspension of particles within a porous three-dimensionally interconnected network in a liquid medium.[73, 74] Another reactant can be added if required in order produce a desired product in the interconnected framework. The deposited gelled sol would then be heated to obtain the final product. This heating will remove the solvent, induce formation of oxides (dependent on the annealing atmosphere), and increase crystallinity.[73]

Advantages of this type of synthesis are that the particles are dispersed more evenly and that the synthesis is usually quicker than an aqueous synthesis. Another advantage which it has over the creation of a suspension, is that it is a one-step process unlike the suspension of a precipitate, which obviously requires the synthesis of the precipitate first. One disadvantage of the sol-gel method is that the materials are often expensive.[74, 75]

1.7.3 – Ceramic synthesis.

This is currently a commonly used method for the preparation of solid materials including mixed metal oxides.[76] This method involves slow reactions of solid reagents in the correct molar ratio at an elevated temperature over a relatively long period of time, and therefore requiring a number of strict conditions.[76] For example, control of stoichiometry is critical as post-reaction purification is almost impossible. These reactions involve high temperatures and long synthesis times due to the fact that they require the diffusion across the points of contact.[76] Due to cations usually being smaller than the anions, they consequently take the role of the mobile ions in the reaction and migrate and form the new structure at the phase boundary. The reaction rate decreases over time due to the increasing distances in which the reactants need to migrate to react, as the number of products increases.[76]

Measures are taken to ensure the diffusion distance is as small and as efficient as possible, including milling and increased energy input respectively.[76] The main advantage of this method is that one can potentially obtain a pure product, without having to purify it, and at a potentially high yield. Another advantage is that it is easier to produce powders, which are otherwise difficult to create, such as silicides and carbides.[77] There are also various problems with this method, including the large temperatures and synthesis times required, as well as impurities being introduced from the milling system.[77] Often also, it is the case that the reaction completion will rarely be 100 %.

1.8 – Thin film deposition techniques.

There are numerous methods currently of applying a sol or suspension to the electrode substrate. The most suitable technique for this is determined predominately from the nature of the resultant suspension or sol. After the application of the precursor sol or suspension the deposited material can be either dried or annealed, or spun first (spin coating). The simplest method for applying a sol or suspension to the substrate is to use drop-coating. This method involves using a dropper, such as a syringe or pipette to apply a particular quantity of material to the surface of the electrode. This method is useful as it is quick and cheap, and is therefore ideal for small scale synthesis for research and development. This method also allows us to control the quantity of material applied in

each layer, *i.e.* the number of drops. Spin coating is a spreading technique, used to uniformly distribute the coating on the electrode surface. This method also removes excess coating on the electrode and films can be gelled by controlled removal of solvent which is dependent on the spinning rate.

The deposition method chosen for a particular film aims to satisfy a number of requirements to control the properties of the electrode, most notably the film thickness and uniformity from electrode to electrode, *i.e.* the reproducibility. The application of the electrode is also taken into account, for example, if it is a small electrode for film research, it is uneconomic for large, costly equipment to be used, but for a larger scale, such as industrial solar panels, smaller scale deposition methods would cause complications.

During spin coating, the amount of material left on the substrate depends on the viscosity of the suspension or sol. Another method is dip coating, which, as the name suggests, involves dipping the electrode into the coating material and withdrawing it at a particular rate, meaning that uniform coating can potentially be achieved, although this allows a controlled deposition of material based on surface tension and adhesion/wetting forces, comparatively small quantities are deposited each time. Other methods for deposition include using sprays, such as spray pyrolysis and spray deposition. Spray pyrolysis involves using a sol or suspension (although a suspension is more problematic due to coagulations of particles blocking the spray nozzle). The sol or suspension is then forced through a nebulizer, creating a spray of fine droplets onto the desired surface. The main limitations of both of these methods is that uniform distribution on the substrate surface is difficult, more so with the spray pyrolysis, as uneven distribution of particles can occur, as control of drop size and distribution can vary between different nebulizers.

CVD (chemical vapour deposition) and PVD (physical vapour deposition) are the other most commonly used coating methods for both research and in industry. CVD is commonly defined as a process of depositing solid materials at high temperature as a result of a chemical reaction of gaseous species that are in a reaction chamber with a heated substrate. The reaction proceeds depending on the vapour pressure and the temperature of the substrate which allows control of product formation. PVD is slightly different; the reactant precursor is a solid, forced into a gaseous state, sometimes by heating, but most

commonly involving ion-bombardment. The gaseous deposition requires relatively low temperatures.[78] There are, as always, both advantages and disadvantages to both of these methods. For example, with both CVD and PVD, a wide range of materials can be used.[78, 79] With CVD, the deposition rate can be altered, however PVD is limited to a low rate, and also CVD does not require an ultra-high vacuum, unlike PVD. With PVD, a low substrate temperature can be used, unlike in CVD.[78, 79]

1.9 – Analytical methods

1.9.1 – X-ray Diffraction (XRD)

X-ray diffraction (XRD) is an analytical technique based on the theory proposed by Max von Laue in 1912, that x-rays may be diffracted through a crystal, and that their wavelengths are comparable to the separation of lattice structure.[80] X-ray electromagnetic radiation is usually created by accelerating high energy electrons at a metal.[80] The deceleration of the electrons generates radiation of a continuous range of wavelengths, known as a 'Bremsstrahlung',[80] German for 'deceleration ray'. William Bragg then focused a monochromatic beam of x-rays at a single rotating crystal. Reflections were detected at angles due to diffraction from the different atomic planes in the crystal.

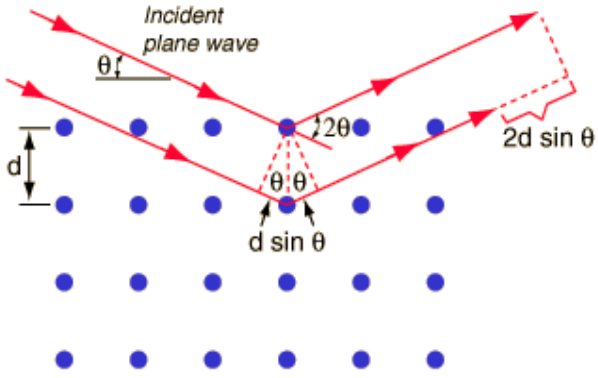

Fig. 1.10 – Diagram to illustrate x-ray diffraction.[81]

The diagram above, in figure 1.10, shows the interaction of the x-rays with the crystal lattice. The lower x-ray beam travels a total distance of 2d sinθ further than the beam that interacts with the plane above it and therefore the spacing between the crystal planes,

d, can be calculated by recording the angles, θ, at which the x-rays are diffracted at, using the Bragg equation, in equation 1.10.

$$n\lambda = 2d \sin\theta \qquad \text{(Equation 1.10)}$$

Where *n* is the integer order of wavelength and λ is the incident wavelength.
The results are presented as peaks, which correspond to the angles at which the diffracted x-rays are detected, an example of which is shown in fig. 1.11.

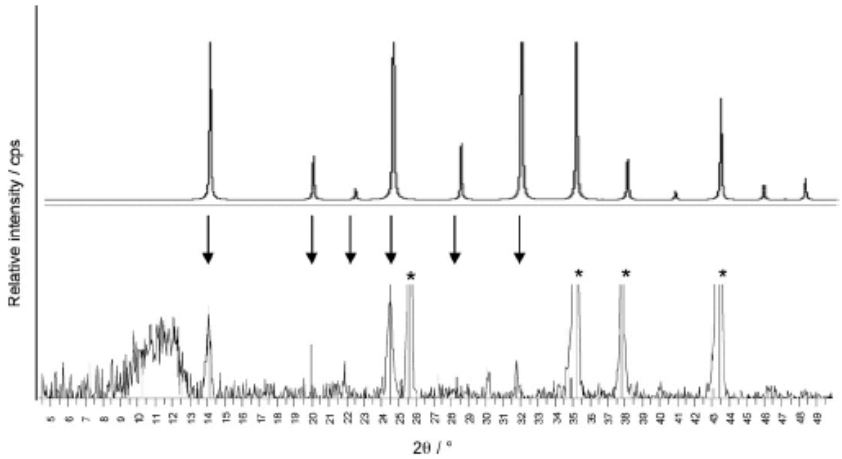

Fig. 1.11 – Example of an XRD pattern.[82]

The peak positions correspond to reflections of the x-rays, from which lattice plane separations can be calculated, which in turn provide information about the cell unit of the material. Each full pattern of peaks corresponds to a particular structure, which is able to assist in characterising the material. From these patterns, it can be observed if the desired product has been synthesized, and in what crystal phase (*i.e.* triclinic, monoclinic *etc.*). Peaks corresponding to impurities can also be detected, and the degree in which they populate the material can be calculated, if the impurity identification is known. Also, the collective peak intensities from sample to sample of the same material can be used to compare relative crystallinities of samples.

The main advantage with this technique is that sample preparation is not difficult; however, some problems can arise with very thin samples, such as thin films, due to the penetration depth of the x-rays, resulting in detected x-rays attributed to the substrate used, whether it is metal or conductive glass. One way to minimise this is to use grazing incidence diffraction.[83] This method differs from conventional XRD, which uses a

constantly changing angle of the incident x-ray, by keeping the x-ray source at a single, critical angle, and only changing the position of the detector, to measure the different angles of diffraction. This critical angle limits the amount of x-rays which will penetrate the sample, to the surface underneath, due to the acute angle of the impact. The limitation of this however is that, clearly, less information will be gathered due to only one incident angle being analysed, meaning decreased peak intensity and clarity. Another disadvantage of this method is if there are any impurities below the reduced penetration depth, they will not be detected.

1.9.2 – Scanning electron microscopy (SEM)

Scanning electron microscopy is a technique used to view samples under high magnifications, in order to determine particle size and morphology. Electrons are directed at high voltage at the surface of the sample, and interactions are recorded to form an image.[84] In order for a clear image to be constructed, the sample needs to be electrically conductive (when the sample charges because it is poorly conductive, the electronic charge interacts with the beam to defocus it). If the material being analysed is not naturally conductive, the sample is generally sputter coated with a conductive material such as gold or chromium.

There are a number of interactions between the electron beam and the sample that generate scattered electrons or x-rays. Each of these will provide different information relating to the sample. They are secondary electrons (SE), back-scattered electrons (BSE) and radiated x-rays.[85] Secondary electrons are generated by inelastic interactions at high energy levels, which excite electrons to such a level that they can overcome the work function, be emitted and detected.[84] Back-scattered electrons are electrons from the beam that are reflected from the sample. The time delay and angle of reflection allows the electron microscope to build an image of the sample. BSEs are easier to detect as they tend to keep most of the energy they had in the beam, which can vary between 50 eV up to a few thousand eV, whereas SE only have energy of up to 50 eV, as shown in figure 1.12.

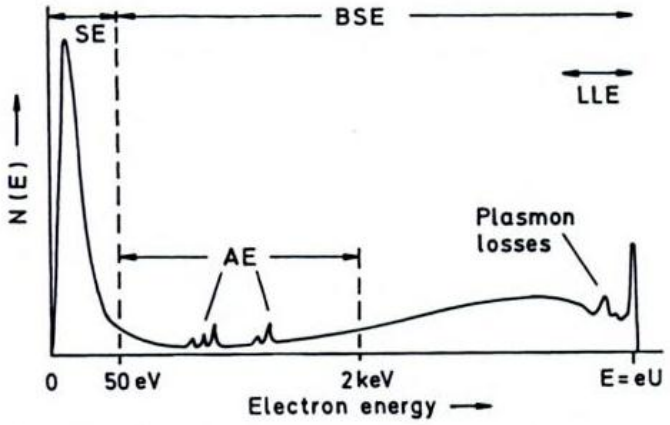

Fig. 1.12 – Energy spectrum of electrons used in SEM.[84]

Figure 1.12 demonstrates the difference in energy level ranges of the electrons detected. Clearly, it shows the broader range of energy levels for the BSEs.

The Auger electrons (AE) are produced when the incident electrons ionise the k-shell of an atom, producing an electron vacancy. The energy of this ionised atom is then reduced by an electron falling into this vacancy from another shell and by a second electron being emitted from that same outer shell, or by an even more weakly bounded shell,[86] shown in figure 1.13a.

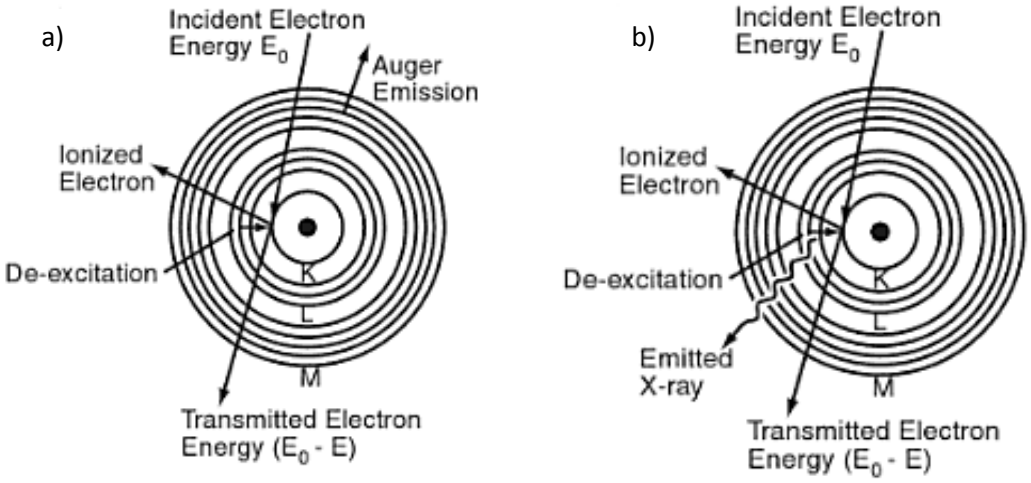

Fig. 1.13 – a) Auger emission from atomic orbitals,[87] b) X-ray emission from electron relaxation in atomic orbitals.[87]

The energy of these emitted electrons reveal information about the atomic composition of the material surface. Another analytical method for doing this is energy-dispersive x-ray spectroscopy (EDX).

1.9.3 – Energy dispersive x-ray spectroscopy (EDX)

Energy dispersive x-ray spectroscopy (EDX) is a technique used to estimate the elemental composition of a particular material. As discussed in section 1.9.1, x-rays are generated when a high energy electron is relaxed and releases its energy.[88] When an electron beam is focused at the sample, inner electrons are emitted from the atoms in the sample, meaning an electron vacancy is produced. An electron from the next shell will then fall into its place, and in doing so, releases energy as an x-ray.[88] This then produces more holes for further outer electrons to fall in, producing more x-rays. This is shown in figure 1.13b.

As these electrons are held by a binding energy that is characteristic of the element, they will in turn release an x-ray of a frequency that is dependent on this binding energy.[88] This data can also be collected quantitatively in order to estimate the ratios of the elements observed. The disadvantages to this technique are that it analyses an area of around 1 μm^2, and so cannot focus on a particular area smaller than that. The other disadvantage is that not all elements can be detected. Elements with an atomic number lower than boron or greater than uranium cannot be detected.

1.9.4 – UV/Vis Spectroscopy.

UV/Vis spectroscopy as an analytical technique which relies on the fact that certain molecules undergo electronic transitions under irradiation from the ultraviolet and visible regions of the electromagnetic spectrum. This usually applies to wavelengths in the region 200-800 nm (UV light being in the 200-400 nm range).[89] Although some groups do absorb below 200 nm, detection is usually difficult due to the fact that oxygen and water also absorb in this region.[90]

Due to the fact that UV and visible radiation is lower in energy than x-rays, transitions between electronic energy levels typically involve electrons in the outer molecular orbitals, rather than core shells. The difference in energy involved in electronic transitions is shown in fig 1.14 in comparison to vibrational transitions and rotational levels.[90]

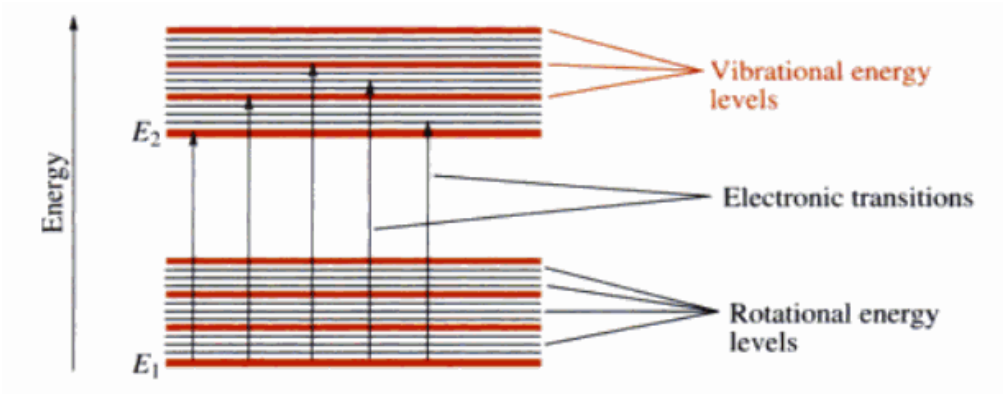

Fig. 1.14 – Transitions involved in UV spectroscopy.[90]

As can be observed, as well as electronic transitions, vibrational transitions can also occur, which accounts for the fact that the produced spectra are usually broad peaks. Spectra are broad predominantly due to solvent effects (i.e. collisions between solvent and solute molecules) rather than vibrational transitions (although these do contribute). Diffuse reflectance spectroscopy detects reflections from rough surfaces that reflect uniformly in all directions, such as films and powders, and contains spectral information of the electronic transitions present in the sample.[91] It determines the absorbance wavelengths responsible for an electronic transition. With specific reference to semiconductors, diffuse reflectance allows estimations of band edge separations to be made in semiconducting materials using Tauc plots derived from the following method.[92-94]

It is important to first take into consideration the scattering[95] and reflection of light, which can be done using the Kubelka-Munk[96, 97] equation (equation 1.11).

$$(1 - T)^2 \ / \ 2T = \text{Kubelka-Munk unit} \qquad \text{(Equation 1.11)}^{96, 97}$$

Where T is transmittance.

Tauc plots are used in order to estimate the band gap by extrapolation of a plot of $\alpha h\nu^n$ against photon energy, $h\nu$.[95] The value n is typically either 1/2 or 2, and depends on the nature of the band gap.

To determine n, plots of $\alpha h\nu^{1/2}$ and $\alpha h\nu^2$ against photon energy are constructed.[92, 98, 99] A comparison of both plots is required to determine which is most linear, and therefore

most applicable. For n = 1/2, the optical band gap corresponds to an indirectly allowed electronic transition, in contrast, when n = 2, the electronic transition is a directly allowed transition.[94]

Direct electronic band gap transitions occur when the k-vectors of the valence and conduction energy bands are aligned. However, when they are not aligned,[100] transition becomes possible as it is mediated through coupling to lattice vibrations, e.g. phonons.[101]

1.9.5 – Infrared Spectroscopy (IR).

Infrared spectroscopy (IR) is an analytical method which can aid in determining a molecular structure. The frequency vibration of chemical bonds depend on the bond order, and the mass of the atoms involved, as seen in equation 1.12.

$$\bar{\upsilon} = \frac{1}{2\pi c}\sqrt{\frac{k}{\mu}} \qquad \text{(Equation 1.12)}[102]$$

Where $\bar{\upsilon}$ is the vibrational frequency in wavenumber, k is the force constant, c is the speed of light, and μ is the reduced mass.[102] IR works on the basis that molecules absorb light at frequencies corresponding to transitions between vibrational energy levels, characteristic to the bond environment, therefore the wavenumbers of IR radiation absorbed by the molecule can give the user information as to the molecular bonds present. For these vibrations to be IR active, they must involve the change in dipole moment during vibration.

1.9.6 – Raman Spectroscopy.

Raman spectroscopy is another analytical technique used to analyse molecular vibrations, although less widely used than IR. The Raman Effect is a very weak effect and only around 1 photon per million is detected. The mechanism for Raman spectroscopy differs to IR spectroscopy, in that it is concerned with the scattering of the light by the sample (shown in fig. 1.15), rather than the absorption.

Excitation in Raman spectroscopy is based on an electronic transition. Raman spectroscopy can access shorter wavenumbers as electronic transitions can obscure data in the region below 400 cm^{-1} in IR spectroscopy. Raman spectroscopy is an ideal technique for inorganic oxide characterisation because the electronic transitions that can obscure IR signals up to 1000 cm^{-1} would obscure most vibrational transitions and so data that would not be seen in IR, would be seen in Raman spectroscopy.

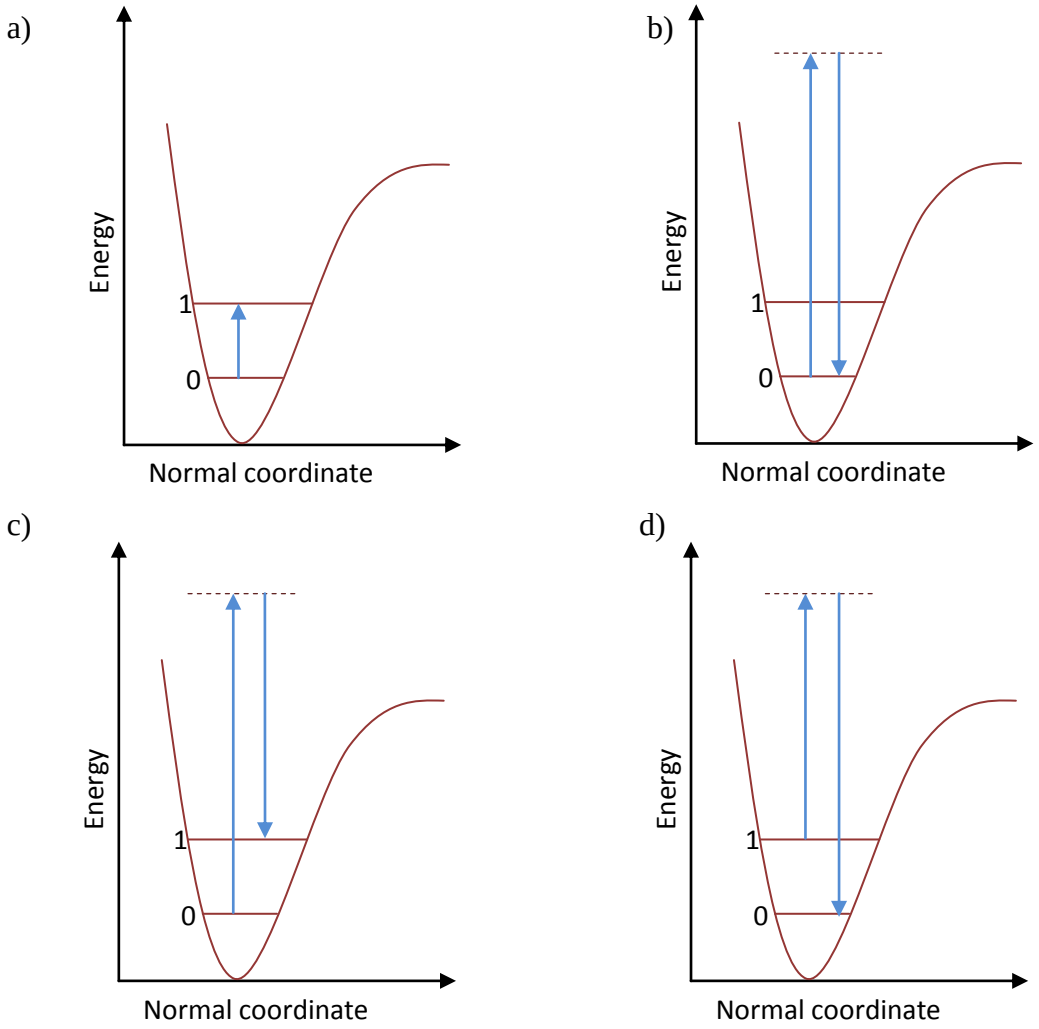

Fig. 1.15 – Morse curves schematically showing transitions that underpin a) IR, b) Rayleigh scattering, c) Raman Stokes scattering and d) Raman anti-Stokes scattering.

In Raman scattering there is an exchange in energy between the photon and the sample. When the incident laser energy interacts with the electron cloud it distorts it into a virtual state (indicated in fig. 1.15 by the dotted lines, the blue arrows show the direction of the energy of the electron cloud). This state is not stable, and is quickly stabilised back to the lower energy levels, emitting energy as a photon.[103] This differs greatly from IR

spectroscopy, which is only concerned with the absorption to the next vibrational energy level, shown in figure 1.15*a*. When the energy is released, it can either leave the molecule at the same vibrational level as before (Rayleigh scattering, figure 1.15b), at a higher level than before, so releasing less energy than absorbed (figure 1.15c), or at a lower energy than before and so releasing more energy (figure 1.15d). The photons detected in Raman spectroscopy have either more or less energy than incident energy and the difference in energy corresponds to a molecular vibration.

For a band to be active in a Raman spectrum, there must be a change in polarisability (*i.e.* a changing dispersion of the electron cloud) in the molecule during the vibration. This is due to the fact that the oscillating electric field of an incident photon causes charged particles in the molecule to oscillate. This leads to an induced electric dipole moment, *P*, shown in equation 1.13.

$$P = \alpha E \qquad \text{(Equation 1.13)}^{[104]}$$

Where E is the strength of the electric field and α is the polarisability.[104] The intensity of this Raman interaction is dependent on the change in polarisability.[103]

Raman spectroscopy does have certain advantages over IR spectroscopy. Molecules containing transition metals are easier to see using Raman spectroscopy than in IR. This is due to the fact the electronegativities of most transition metals are similar so the permanent dipole moments will also be similar, and not easily distinguishable. Another advantage of Raman spectroscopy is that the spectra will not contain any peaks corresponding to water, as this is Raman-inactive, meaning that aqueous solutions can also be analysed. Disadvantages can include fluorescence, sample degradation.[103]

1.9.7 – Photo-electrochemistry

Photo-electrochemistry is used to establish how charge transfer across an interface is enhanced (or otherwise) when an electrode is irradiated. This is particularly useful given that photocatalytic water splitting involves redox reactions.[52] In semiconductors, the conductivity of a material will change when a photon is absorbed, as electron-holes are generated,[52] thus, the extent of an electrochemical reaction, and how it responds to

changes in irradiation can be easily monitored. This method is most commonly used to determine whether a material produces photo-induced electron-hole pairs, and to what extent. An electrochemical measurement is first performed in absence of light to establish if there are any underlying electrochemical reactions in the potential range of interest. The experiment is then repeated under illumination and any change in current observed is indicative of electrochemical reactions induced by the presence of light, in the case of a semiconductor this is most likely due to the generation of electron-hole pairs which then react at the surface of the electrode. In the case of hydrogen generation, the observed current is due to an electron transferred from the electrode to the surrounding media to reduce water.

Variations of measurement illumination conditions can also tell the user more about performance properties of the material. Photo-electrochemistry, typically photocurrent-voltage plots, tend to use broad spectrum irradiation such as simulated sunlight. Thus it is difficult to tell exactly what the observed photocurrent arises from, i.e. which parts of the electromagnetic spectrum are responsible for the majority of the photocurrent. Incident-photon-to-current-efficiency (IPCE) measurements directly measure efficiency of conversion of a photon to current, as the name suggests, at a particular wavelength. This wavelength dependence is additional useful information that can help characterise the response of the semiconductor to UV light as opposed to visible light. The conversion efficiency at a given wavelength can be calculated by:

$$\boldsymbol{IPCE}\ (\%) = \frac{\mathbf{1240} \times \boldsymbol{current\ density}\ (\mu \boldsymbol{A cm^{-2}})}{\boldsymbol{wavelength}\ (\boldsymbol{nm}) \times \boldsymbol{power\ input}\ (\mu \boldsymbol{W cm^{-2}})} \times 100 \quad \text{(Equation 1.14)}^{52}$$

The electrochemistry measurements of the material can also provide information as to the nature of the semiconductor. For example, capacitance measurements such as Mott-Schottky analysis where the response of capacitance to an applied potential can uncover information on the photo-physical nature of the semiconductor such as flat-band potential (*i.e.* the potential of the valence band),[105] whether it is a p-type or n-type semiconductor (electron accepting or donating, respectively), and its charge acceptor or donor density.[105, 106]

1.10 – Aims of the project herein

Iron vanadate will be investigated for its potential in photo-induced water-splitting for hydrogen production. Iron vanadate was selected based on the comparatively low band gap of iron oxide,[47, 51, 107] and the known photocatalytic activity of other metal vanadates,[60, 108-113] Iron vanadate powder will firstly be synthesised using a low temperature, aqueous precipitation reaction.[57] The effect on the product of annealing temperature and atmosphere will be investigated. Characterisation will aim to determine how crystallinity, particle size and morphology, structural properties and band gap change with increasing annealing temperatures, and also with a change in annealing atmosphere. The photocatalytic activity of these materials will then be examined by creating thin films of the iron vanadate, and using photo-electrochemistry to assess the extent to which the iron vanadate electrodes are photocatalytically active. Full characterisation will allow establishment of any links between processing conditions, electrode composition and crystallinity, and photocurrent. The effect of solution processing *i.e.* using a sol-gel synthesis, rather than deposition of pre-formed powders, will be investigated to assess the effect on film stability and efficiency.

1.11 - References

1. N. Armaroli and V. Balzani, *Angewandte Chemie-International Edition*, 2007, **46**, 52-66.

2. R. van de Krol, Y. Q. Liang and J. Schoonman, *Journal of Materials Chemistry*, 2008, **18**, 2311-2320.

3. N. S. Lewis and D. G. Nocera, *Proceedings of the National Academy of Sciences of the United States of America*, 2006, **103**, 15729-15735.

4. D. A. J. Rand, R. M. Dell and R. Dell, *Hydrogen Energy: Challenges and prospects*, Royal Society of Chemistry, Cambridge, UK, 2008.

5. N. Parmentier and J. C. Nenot, *Atmospheric Environment*, 1989, **23**, 771-775.

6. M. Pagliaro, A. G. Konstandopoulos, R. Ciriminna and G. Palmisano, *Energy & Environmental Science*, 2010, **3**, 279-287.

7. *Oxford dictionary of Chemistry*, Oxford University Press, Oxford, UK, 2000.

8. B. C. H. Steele and A. Heinzel, *Nature*, 2001, **414**, 345-352.

9. Furman's Enivironmental and Society class, What Is A Hydrogen Fuel Cell?, http://biodiesel.environmentalactiongroup.org/hydrogen.html, Accessed 21/06/12, 2012.

10. F. Barbir, *PEM fuel cells: Theory and practice*, Academic Press, London, UK, 2005.

11. S. M. Haile, *Acta Materialia*, 2003, **51**, 5981-6000.

12. L. Wang, A. Husar, T. H. Zhou and H. T. Liu, *International Journal of Hydrogen Energy*, 2003, **28**, 1263-1272.

13. F. Barbir and T. Gomez, *International Journal of Hydrogen Energy*, 1996, **21**, 891-901.

14. B. Sorensen, *International Journal of Hydrogen Energy*, 2007, **32**, 683-686.

15. A. Kazim, *Renewable Energy*, 2002, **26**, 479-488.

16. B. K. Boggs and G. G. Botte, *Journal of Power Sources*, 2009, **192**, 573-581.

17. V. Ganesan, *Internal combustion engines*, Tata McGraw-Hill Education, New York, USA. 2002.

18. Honda, Fuel Cell Comparison, **http://automobiles.honda.com/fcx-clarity/fuel-cell-comparison.aspx**, Accessed 20/06/12, 2012.

19. D. N. Prater and J. J. Rusek, *Applied Energy*, 2003, **74**, 135-140.

20. K. Rajeshwar, R. D. McConnell and S. Licht, *Solar hydrogen generation: toward a renewable energy future*, Springer, New York, USA, 2008.

21. National Research Council (U.S.). Committee on Soldier Power/Energy Systems, *Meeting the energy needs of future warriors*, National Academies Press, Washington DC, USA, 2004.

22. M. Termtanun, P. Rangsunvigit, B. Kitiyanan, S. Kulprathipanja and W. Tanthapanichakoon, *Science and Technology of Advanced Materials*, 2005, **6**, 348-351.

23. V. Alagharu, S. Palanki and K. N. West, *Journal of Power Sources*, 2010, **195**, 829-833.

24. H. Junge, A. Boddien, F. Capitta, B. Loges, J. R. Noyes, S. Gladiali and M. Beller, *Tetrahedron Letters*, 2009, **50**, 1603-1606.

25. Y. Z. Chen, H. Y. Xu, Y. Z. Wang and G. X. Xiong, *Catalysis Today*, 2006, **118**, 136-143.

26. T. Bak, J. Nowotny, M. Rekas and C. C. Sorrell, *International Journal of Hydrogen Energy*, 2002, **27**, 991-1022.

27. A. P. Simpson and A. E. Lutz, *International Journal of Hydrogen Energy*, 2007, **32**, 4811-4820.

28. European Commission, *Concentrating solar power: From research to implementation*, 2007, 1-39.

29. A. Melis, M. Seibert and M. L. Ghirardi, *Adv Exp Med Biol*, 2007, **616**, 110-121.

30. S. K. Deb, *Solar Energy Materials and Solar Cells*, 2008, **92**, 245-258.

31. M. S. Dresselhaus and I. L. Thomas, *Nature*, 2001, **414**, 332-337.

32. B. Sorensen, *Hydrogen and fuel cells*, Academic Press, Oxford, UK, 2005.

33. A. Fujishima, X. T. Zhang and D. A. Tryk, *Surface Science Reports*, 2008, **63**, 515-582.

34. B. D. Alexander, P. J. Kulesza, L. Rutkowska, R. Solarska and J. Augustynski, *Journal of Materials Chemistry*, 2008, **18**, 2298-2303.

35. A. Fujishima and K. Honda, *Nature*, 1972, **238**, 37-38.

36. F. E. Osterloh, *Chemistry of Materials*, 2008, **20**, 35-54.

37. M. R. Hoffmann, S. T. Martin, W. Y. Choi and D. W. Bahnemann, *Chemical Reviews*, 1995, **95**, 69-96.

38. C. C. Trapalis, P. Keivanidis, G. Kordas, M. Zaharescu, M. Crisan, A. Szatvanyi and M. Gartner, in *12th International Conference on Thin Films*, Elsevier Science, Bratislava, Slovakia, 2002.

39. R. Molinari, L. Palmisano, E. Drioli and M. Schiavello, *Journal of Membrane Science*, 2002, **206**, 399-415.

40. T. Arai, Y. Konishi, Y. Iwasaki, H. Sugihara and K. Sayama, *Journal of Combinatorial Chemistry*, 2007, **9**, 574-581.

41. A. Fujishima and X. T. Zhang, *Comptes Rendus Chimie*, 2006, **9**, 750-760.

42. T. L. Thompson and J. T. Yates, *Chemical Reviews*, 2006, **106**, 4428-4453.

43. M. Gratzel, *Nature*, 2001, **414**, 338-344.

44. NREL, Reference Solar Spectral Irradiance: Air Mass 1.5, http://rredc.nrel.gov/solar/spectra/am1.5/, Accessed 19/06/12, 2012.

45. D. Chatterjee and S. Dasgupta, *Journal of Photochemistry and Photobiology C-Photochemistry Reviews*, 2005, **6**, 186-205.

46. A. L. Linsebigler, G. Q. Lu and J. T. Yates, *Chemical Reviews*, 1995, **95**, 735-758.

47. S. Saremi-Yarahmadi, K. G. U. Wijayantha, A. A. Tahir and B. Vaidhyanathan, *Journal of Physical Chemistry C*, 2009, **113**, 4768-4778.

48. K. Sivula, F. Le Formal and M. Graetzel, *Chemsuschem*, 2011, **4**, 432-449.

49. C. J. Sartoretti, M. Ulmann, B. D. Alexander, J. Augustynski and A. Weidenkaff, *Chemical Physics Letters*, 2003, **376**, 194-200.

50. N. Özer and F. Tepehan, *Solar Energy Materials and Solar Cells*, 1999, **56**, 141-152.

51. A. A. Tahir, K. G. U. Wijayantha, S. Saremi-Yarahmadi, M. Mazhar and V. McKee, *Chemistry of Materials*, 2009, **21**, 3763-3772.

52. *On Solar Hydrogen & Nanotechnology*, John Wiley & Sons, Chichester, UK, 2009.

53. Stored Solar Limited, Solar assisted electrolysis, http://www.storedsolar.com/solarelectrolyser.html, Accessed 18/06/12, 2012.

54. B. L. Oliva and A. R. Barron, An Introduction to Solar Cell Technology, http://cnx.org/content/m41217/latest/, Accessed 20/06/12, 2012.

55. J. Haber, *Catalysis Today*, 2009, **142**, 100-113.

56. E. Baudrin, S. Denis, F. Orsini, L. Seguin, M. Touboul and J. M. Tarascon, *Journal of Materials Chemistry*, 1999, **9**, 101-105.

57. P. Poizot, E. Baudrin, S. Laruelle, L. Dupont, M. Touboul and J. M. Tarascon, *Solid State Ionics*, 2000, **138**, 31-40.

58. P. Poizot, S. Laruelle, M. Touboul and J. M. Tarascon, *Comptes Rendus Chimie*, 2003, **6**, 125-134.

59. L. Ge, *Materials Letters*, 2008, **62**, 926-928.

60. K. Sayama, A. Nomura, T. Arai, T. Sugita, R. Abe, M. Yanagida, T. Oi, Y. Iwasaki, Y. Abe and H. Sugihara, *Journal of Physical Chemistry B*, 2006, **110**, 11352-11360.

61. C. D. Morton, I. J. Slipper, M. J. K. Thomas and B. D. Alexander, *Journal of Photochemistry and Photobiology A:Chemistry*, 2010, **216**, 209-214.

62. Z. Z. He, J. I. Yamaura and Y. Ueda, *Journal of Solid State Chemistry*, 2008, **181**, 2346-2349.

63. F. Laves, Acta Cryst., 1964, 1476-1477.

64. A. P. Young and C. M. Schwartz, Acts Cryst., 1962, 1305.

65. J. Muller and J. C. Joubert, *Journal of Solid State Chemistry*, 1975, **14**, 8-13.

66. Y. Oka, T. Yao, N. Yamamoto, Y. Ueda, S. Kawasaki, M. Azuma and M. Takano, *Journal of Solid State Chemistry*, 1996, **123**, 54-59.

67. Y. Hotta, Y. Ueda, N. Nakayama, K. Kosuge, S. Kachi, M. Shimada and M. Koizumi, *Journal of Solid State Chemistry*, 1984, **55**, 314-319.

68. K. Melghit and A. S. Al-Mungi, *Materials Science and Engineering B-Solid State Materials for Advanced Technology*, 2007, **136**, 177-181.

69. G. Mangamma, E. Prabhu and T. Gnanasekaran, *Bulletin of Electrochemistry*, 1996, **12**, 696-699.

70. S. Denis, E. Baudrin, F. Orsini, G. Ouvrard, M. Touboul and J. M. Tarascon, *Journal of Power Sources*, 1999, **81**, 79-84.

71. J. H. Deng, J. Y. Jiang, Y. Y. Zhang, X. P. Lin, C. M. Du and Y. Xiong, *Applied Catalysis B-Environmental*, 2008, **84**, 468-473.

72. D. D. Ebbing and S. D. Gammon, *General Chemistry*, Cengage Learning, Kentucky, USA, 2007.

73. L. Smart and E. Moore, *Solid State Chemistry: An Introduction*, CRC Press, Florida, USA, 1995.

74. A. C. Pierre, *Introduction to sol-gel processing*, Springer, Massachusetts, USA, 1998.

75. S. Sakka, *Handbook of sol-gel science and technology: processing, characterization and applications*, Springer, New York, USA, 2005.

76. S. E. Dann, *Reactions and characterization of solids*, Royal Society of Chemistry, 2000.

77. M. N. Rahaman, *Ceramic processing and sintering*, CRC Press, Florida, USA. 2003.

78. E. F. Vansant, P. Voort and K. C. Vrancken, *Characterization and chemical modification of the silica surface*, Elsevier, Amsterdam, The Netherlands, 1995.

79. X.-T. Yan and Y. Xu, *Chemical Vapour Deposition: An Integrated Engineering Design for Advanced Materials*, Springer, London, UK, 2010.

80. P. Atkins and J. De Paula, *Atkins' Physical Chemistry*, Oxford University Press, Oxford, UK, 2006.

81. S. T. Thornton and A. Rex, Bragg's Law, http://hyperphysics.phy-astr.gsu.edu/hbase/quantum/bragg.html, Accessed 21/06/12, 2012.

82. A. van Niekerk, J. Zah, J. C. Breytenbach and H. M. Krieg, *Journal of Membrane Science*, 2007, **300**, 156-164.

83. *Powder diffraction*, Allied Publishers, New Delhi, India, 2002.

84. L. Reimer, *Scanning electron microscopy: physics of image formation and microanalysis*, Springer, Derlin, Germany, 1998.

85. JEOL Ltd., *Scanning Electron Microscope A to Z: Basic knowledge for Using the SEM*.

86. M. Prutton and M. M. El Gomati, *Scanning Auger electron microscopy*, John Wiley and Sons, Chichester, UK, 2006.

87. A. Kirkland, J. Hutchison and J. L. Hutchison, *Nanocharacterisation*, Royal Society of Chemistry, Cambridge, UK, 2007.

88. A. J. Garratt-Reed and D. C. Bell, *Energy-Dispersive X-Ray Analysis in the Electron Microscope*, BIOS Scientific Publishers Ltd., Oxford, UK, 2003.

89. W. H. Brown, C. S. Foote, B. L. Iverson, E. V. Anslyn and B. M. Novak, *Organic Chemistry*, Cengage Learning, California, USA, 2011.

90. R. J. Anderson, D. J. Bendell and P. W. Groundwater, *Organic spectroscopic analysis*, Royal Society of Chemistry, Cambridge, UK, 2004.

91. V. M. Sellitto, R. B. A. Fernandes, V. Barron and C. Colombo, *Geoderma*, 2009, **149**, 2-9.

92. Z. G. Zou, J. H. Ye and H. Arakawa, *Topics in Catalysis*, 2003, **22**, 107-110.

93. B. Yang, P. R. F. Barnes, W. Bertram and V. Luca, *Journal of Materials Chemistry*, 2007, **17**, 2722-2729.

94. W. Yao, H. Iwai and J. Ye, *Dalton Transactions*, 2008, 1426-1430.

95. A. B. Murphy, *Solar Energy Materials and Solar Cells*, 2007, **91**, 1326-1337.

96. K. Ichimura, A. Funabiki, K. I. Aoki and H. Akiyama, *Langmuir*, 2008, **24**, 6470-6479.

97. J. J. Li, K. Chatterjee, A. Medek, E. Shalaev and G. Zografi, *Journal of Pharmaceutical Sciences*, 2004, **93**, 697-712.

98. P. K. Pandey, N. S. Bhave and R. B. Kharat, *Electrochimica Acta*, 2006, **51**, 4659-4664.

99. S. Y. Ryu, W. Balcerski, T. K. Lee and M. R. Hoffmann, *Journal of Physical Chemistry C*, 2007, **111**, 18195-18203.

100. A. C. Jones, P. O'Brien and P. O'Brien, *CVD of compound semiconductors: precursor synthesis, development and applications*, John Wiley and Sons, Chichester, UK, 1997.

101. C. S. Solanki, *Solar Photovoltaics: Fundamentals Technologies And Applications*, PHI Learning Pvt. Ltd., New Delhi, India, 2009.

102. C. E. Housecroft and A. G. Sharpe, *Inorganic Chemistry*, Pearson Education, Harlow, UK, 2007.

103. D. G. Smith E., *Molecular Raman Spectroscopy: A practical approach*, John Wiley & Sons Ltd, Chichester, UK, 2005.

104. K. Nakamoto, *Infreared and Raman spectra of inorganic and coordination compounds, Part A*, John Wiley & Sons, Chichester, UK, 1997.

105. P. Knauth and Y. Massiani, *Journal of Electroanalytical Chemistry*, 1998, **442**, 229-234.

106. A. A. Tahir, K. G. U. Wijayantha, M. Mazhar and V. McKee, *Thin Solid Films*, 2010, **518**, 3664-3668.

107. S. R. Pendlebury, M. Barroso, A. J. Cowan, K. Sivula, J. W. Tang, M. Gratzel, D. Klug and J. R. Durrant, *Chemical Communications*, 2011, **47**, 716-718.

108. C. S. Enache, D. Lloyd, M. R. Damen, J. Schoonman and R. V. de Krol, *Journal of Physical Chemistry C*, 2009, **113**, 19351-19360.

109. G. S. Li, D. Q. Zhang and J. C. Yu, *Chemistry of Materials*, 2008, **20**, 3983-3992.

110. S. S. Dunkle, R. J. Helmich and K. S. Suslick, *Journal of Physical Chemistry C*, 2009, **113**, 11980-11983.

111. H. Jiang, H. Endo, H. Natori, M. Nagai and K. Kobayashi, *Journal of the European Ceramic Society*, 2008, **28**, 2955-2962.

112. H. B. Fang, M. X. Xu, L. Ge and Z. Y. He, *Transactions of Nonferrous Metals Society of China*, 2006, **16**, S373-S376.

113. L. W. Zhang, H. B. Fu, C. Zhang and Y. F. Zhu, *Journal of Solid State Chemistry*, 2006, **179**, 804-811.

2 – EXPERIMENTAL

2.1 – List of Chemicals

Acetone – Fisher Scientific, >99%

Acetylacetonate – Fluka – 99.5%

Ammonium metavanadate – Alfa Aesar, 99% minimum

Deionised water (16.3 MΩ)

DMF – Sigma Aldrich – 99%

Glacial acetic acid – GPR – 100%

Iron acetylacetonate – Fluka - >97%

Iron (II) chloride – Sigma Aldrich – 98%

Iron (III) chloride – Sigma Aldrich – 97%

Iron ethoxide – Alfa Aesar – 99.6%

Iron nitrate nonohydrate – Riedel-de Haën, 98-100%

Mineral oil – Sigma Aldrich

Potassium bromide Spectrosol - Fluka

PVDF – Sigma Aldrich

Sodium hydroxide – Fisher - >98%

Triethylamine - Fisher

Vanadyl acetyl-acetonate – Sigma Aldrich, 98%

2.2 – Powder synthesis

Iron vanadate was synthesised using a known 'chimie douce' method.[1, 2] Ammonium metavanadate (750 ml, 4.27 x 10^{-3} M) was placed in round bottomed flask and heated to 70 °C on an oil bath under continuous stirring. The flask was fitted with an air condenser to prevent loss of solvent during the reaction. Iron nitrate solution (12.25 ml, 0.26M) was then added slowly, and instantly, a suspension of orange particles was observed. The reaction was left to proceed for 72 hours, at 70 °C with constant stirring. The pH was monitored throughout and remained at 3 during the reaction.

Upon cooling to room temperature, the reaction mixture was removed and centrifuged for 15 minutes at 4000 rpm. This resulted in a brown solid at the bottom of a clear supernatant liquid. This brown solid was washed by decanting the supernatant before suspension in deionised water and centrifuging for 15 minutes at 4000 rpm. The supernatant was then removed and the solid was washed with acetone and centrifuged again. The acetone was then removed and the solid was left to dry in air at room temperature overnight. The following day, the solid was placed in an oven at 50 °C for 7 hours to dry fully. After this, the brown solid was removed and weighed, and was typically between 0.5 and 0.6 g. The percentage yield ranged from 86 and 96 %.

2.3 – Annealing

The products of repeated reactions were combined and then split into portions of around 0.2 g. Samples were then annealed a particular temperature, either 250, 350, 450, 550, 600, 650 or 700 °C, in atmospheres of air, nitrogen or oxygen, in an alumina crucible in a tube furnace. The samples were annealed for 50 minutes.

2.4 – Deposition of thin films from powder suspensions

0.5 g of the amorphous product of the precipitation reaction described in section 2.2 was suspended in a solution, of 2 g of PVDF dissolved in 10 ml DMF. Electrodes were prepared by drop-coating the suspension onto glass electrodes with an F-doped SnO_2 overlayer (Solaronix, CH). One layer was made following the deposition of the suspension onto the conducting glass substrate, which was then dried in air at room temperature for 10 minutes and the excess material removed by the doctor-blading technique. The electrode was then annealed at a given temperature between 250 and 700 °C, in oxygen atmosphere. This process was repeated to deposit additional layers (*e.g.* three or six layers) of approximately 2.0 x 1.0 cm in dimension. The effect on the film morphology and other properties were investigated by annealing for 10 and 30 minutes and gelling for 10 minutes or by annealing the sample directly after deposition.

2.5 – Acetyl acetonate based sol method

Iron vanadate thin films were created using a similar method reported by Sayama *et al.*[3] for producing bismuth vanadate. A 0.2 M solution of iron nitrate nonohydrate in acetic acid, and 0.03 M solution of vanadyl acetyl acetonate in acetyl acetone were mixed in equimolar proportions. This red coloured solution was then deposited onto conducting glass electrodes. The layer was then either left to gel for 10 minutes or not at all, then spun at 1000 rpm for 15 seconds to remove excess material. The electrode was then immediately transferred to a furnace and heated at the desired temperature in oxygen for ten minutes. After the electrode had been removed and left to cool, the process was repeated to deposit additional layers. Layers produced were of *ca.* 1.0 x 2.0 cm in dimensions.

2.6 – Analysis

2.6.1 – X-ray diffraction

XRD analysis of the iron vanadate powder was performed using a Siemens Kristalloflex 810 X-ray diffractometer and CuKα source. A small amount (~0.05 g) of sample was placed on a clean sample holder, a few drops of acetone were dropped on and allowed to evaporate in order to spread the sample evenly over the holder. When the sample had dried, it was placed in the diffractometer and set to scan at 0.5° 2θ per minute.

XRD of the thin films was performed using a Bruker AXS D8 Advance X-ray diffractometer using Cu Kα radiation. A Goebel mirror was used to produce a parallel beam of X-rays and remove CuKβ radiation. An energy dispersive SolEx detector was used with a window set to accept CuKα energies, rejecting fluorescence due to iron and vanadium. Scans were run from 3-70º 2θ, with a step size 0.02º 2θ, and a count time 2 seconds/step. The anti-scatter slit was set at 0.5, and a knife edge was used to remove high backgrounds at low 2θ values. All samples were rotated at 15 revolutions per minute for increased homogeneity.

2.6.2 – EDX

Samples were analysed under a JEOL JSM 5310LV SEM, with an Oxford Instruments ISIS 300 EDX detection system, using a working distance of 15 mm and an accelerating voltage of 20 kV. Samples were first carbon coated to eliminate surface charging and because carbon peaks are easier to distinguish than those corresponding to gold.

2.6.3 – Scanning electron microscopy.

Scanning electron micrographs were recorded on a Cambridge Institutes Stereoscan 360, with an accelerating voltage of *ca.* 30 kV and a working distance of around 4 mm. A conductive carbon film was positioned on each sample platform. On this sticky surface, a few grains of sample were scattered, with any unattached excess blown off. They were then sputter coated with gold.

2.6.4 – Infrared spectroscopy

A Perkin Elmer Paragon 1000 FT-IR spectrometer was used for the IR spectroscopy. Sample discs were prepared by mixing dry KBr (spectroscopic grade stored at 100 °C) with the iron vanadate sample (0.4% w/w %). Samples were then pressed into a disc, using *ca.* 7 bar of pressure for *ca.* 60 seconds. The disc was then placed in the spectrometer and each spectrum was the result of an average of 10 scans over the range of 4000-450 cm^{-1}.

2.6.5 – Raman spectroscopy

Raman spectra were recorded using a LabRam I Raman spectrometer (Horiba Jobin Yvon). This spectrometer has a 1800 lines/mm holographic grating, and a D2 neutral density filter was used to sufficiently limit the power. A holographic long-pass filter was used to prevent Rayleigh scattering, a CCD used for detection and an Olympus BX40 microscope for focusing on the sample, up to 50 x magnification. A frequency doubled Nd : YAG laser (532 nm) was used for excitation. The instrument was calibrated using silicon. A slit-width of 100 μm, and a pin hole-width of 900 μm were used. Samples

were placed on a glass microscope slide and a video image was used to select a sample area and then to focus the beam. The focus was then finely adjusted to attain the maximum strength of the spectrum possible before the data was collected, using an average of 5 scans, at a rate of 1 scan per 20 seconds.

2.6.6 – UV/Vis spectroscopy.

Powder samples were analysed by diffuse reflectance spectroscopy using an Agilent UV/Vis spectrophotometer. This was coupled with a Labsphere RSA-HP-8453 integrating sphere. All of the powder samples were prepared in the same way. The sample was placed in the sample holder, and held in place by a glass slide. A Spectralon© disk was used as a reference for the spectrometer.

For the electrodes, the spectra were taken using a Jasco V-650 spectrophotometer with a high sensitivity photomultiplier tube detector. The electrode was placed in the sample holder with the reference material (Spectralon©) behind it. The blank was the conductive glass substrate with the reference behind it.

2.6.7 – Magnetic susceptibility.

Magnetic susceptibility measurements were taken using a Johnson Matthey Magnetic Susceptibility Balance. A known mass of reference sample, $Hg[Co(SCN)_4]$, was used to determine the instrumental constant. From the susceptibility measurements of the known masses (0.05-0.09 g) of sample in the sample tube (~5 mm diameter) the mass susceptibility could be calculated, and from this, the molar susceptibility and the magnetic moment, μ, were calculated.

2.6.8 – Photo-electrochemistry

For the photo-electrochemical measurements, the working electrodes were immersed in an electrolyte in a custom-built Teflon cell, fitted with a quartz window. The counter electrode was a platinum sheet and reference electrode was a saturated calomel electrode. Samples were irradiated from the electrolyte-semiconductor interface by simulated solar irradiation from a 150 W Xe lamp (Oriel, 6253) housed in an Oriel 66907, fitted with

AM1.5 and IR filters. AM1.5 filters are designed to provide standard illumination that simulates solar irradiation. The light intensity, measured at the sample using Newport 818P thermopile sensor attached to a Newport 1918-C hand-held optical power meter, was 100 $mWcm^{-2}$. A microAutolabIII potentiostat was used for all electrochemical measurements.

2.6.9 – IPCE

Films were placed into 0.5M NaOH electrolyte in a custom-built Teflon cell, and exposed to monochromatic light from a monochromator (Optical Building Blocks), regulated by a MD-1000 monochromator shutter controller containing a 75 watt Xe lamp, operated by Labview MoCo program (Optical Building Blocks). The reference electrode was Ag/AgCl, and platinum was used as a counter electrode. Photocurrent measurements were taken using an Autolab PGstat12 using a constant voltage of 0.45 V, and the power of the incident light was measured with PM100 universal console, with a range of 200-1100 nm, using a silicon sensor.

2.7 – References

1. P. Poizot, E. Baudrin, S. Laruelle, L. Dupont, M. Touboul and J. M. Tarascon, *Solid State Ionics*, 2000, **138**, 31-40.

2. F. Orsini, E. Baudrin, S. Denis, L. Dupont, M. Touboul, D. Guyomard, Y. Piffard and J. M. Tarascon, *Solid State Ionics*, 1998, **107**, 123-133.

3. K. Sayama, A. Nomura, T. Arai, T. Sugita, R. Abe, M. Yanagida, T. Oi, Y. Iwasaki, Y. Abe and H. Sugihara, *Journal of Physical Chemistry B*, 2006, **110**, 11352-11360.

3 – PRECURSOR POWDER SYNTHESIS AND CHARACTERISATION

Given that the product resulting from the precipitation reaction detailed in section 2.2 was going to be used for the deposition of thin film electrodes followed by annealing of the film, it was considered useful to first characterise how the resulting powder responds to annealing at a given temperature and in a particular atmosphere. This was performed to aid the interpretation of the analysis of the thin film electrodes in the following chapter as it is anticipated that analysis of bulk powder samples will provide richer data, *e.g.* in terms of signal to noise, than analysis of thin film electrodes. This is particularly the case for x-ray diffraction.

The solid product obtained from the low-temperature aqueous synthesis was annealed at temperatures between 250-700 °C, in atmospheres of oxygen, air and nitrogen. Here the effect of annealing conditions on crystallinity, composition and particle size will be investigated.

3.1 – X-ray diffraction

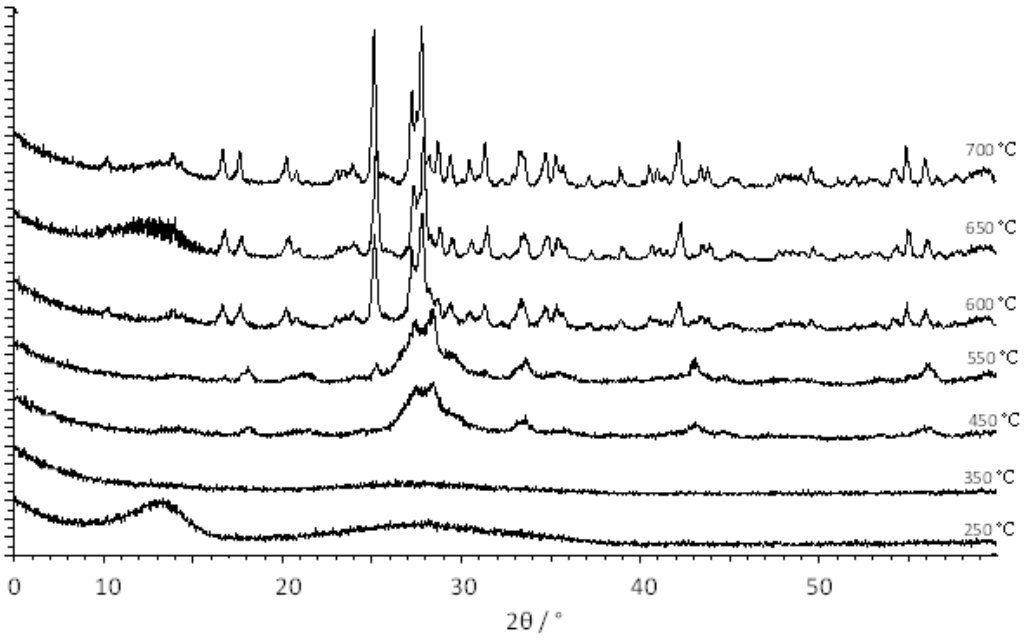

Fig. 3.1 – XRD diffractograms of iron vanadate samples annealed for 50 minutes in air.

The obtained XRD diffractograms shown in figure 3.1 visibly change upon increasing the annealing temperature. The increased peak intensity and decreased peak width with increasing annealing temperature is evidence of an increase in crystallinity. It can be seen that the samples annealed at 250 and 350 °C show no clear peaks, and therefore are amorphous. Peaks are more visible for other samples, therefore they are more crystalline. The samples annealed at 450 and 550 °C were slightly more crystalline due to peaks being visible, corresponding to triclinic $FeVO_4$ (shown at 18º, 22.5º, 27.4º, 28.5º, 29.5º, 33.5º and 43.2º *2θ*) (ICDD pattern no. 038-1372).[1] The samples annealed at 600, 650 and 700 °C produced many additional peaks for triclinic $FeVO_4$ (shown at 10.1º, 13.8º, 14.2º, 16.6º, 20.2º, 23º, 23.3º, 24º, 25.1º, 27.8º, 28.1º, 30º, 30.4º, 31.3º, 32.8º, 32.8º, 34.7º, 35.4º, 37.1º, 38.1º, 38.5º, 39º, 40.1º, 40.5º, 40.9º, 41.5º, 42.1º, 42.9º, 43.8º and 45º *2θ*),[1] and a small number of peaks that correspond to hematite, α-Fe_2O_3 (shown at 24º, 33.1º, 36.5º, 41.9º and 52.2º *2θ*) (ICDD pattern no. 033-0664).[1]

To investigate the effect of annealing atmosphere, the product of the precipitation reaction was annealed in nitrogen and oxygen atmospheres. The results of x-ray diffraction analysis for samples annealed in nitrogen are shown in fig. 3.2.

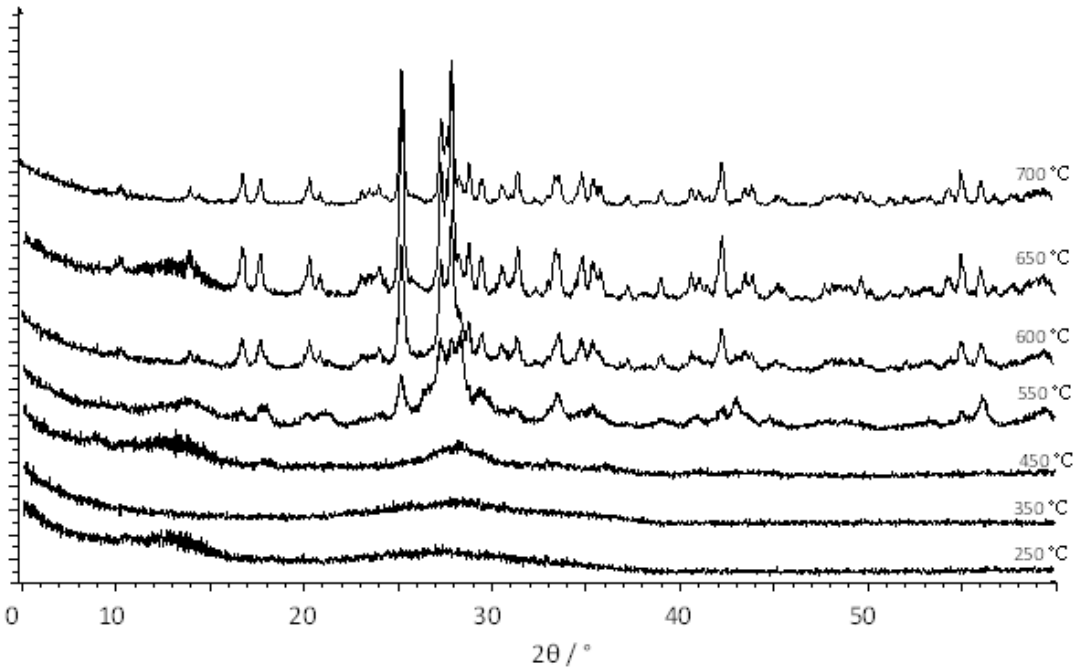

Fig. 3.2 – XRD diffractograms of iron vanadate samples annealed for 50 minutes in nitrogen.

Fig. 3.2 shows that the patterns of the nitrogen annealed samples are very similar to those of samples annealed in air. The only discernible difference is in the sample annealed at 450 °C, which seems to be slightly more amorphous than the corresponding sample annealed in air, indicated by the fact that the diffraction pattern consists of peaks that are less defined than those in fig. 3.1. No new peaks appear in fig. 3.2 compared to fig. 3.1 and so the same assignments of the diffraction patterns apply.

It is not inconceivable that oxygen will influence the crystallisation of iron vanadate, or the photocatalytic performance. Samples were annealed in oxygen and the resulting x-ray analysis is presented in fig. 3.3.

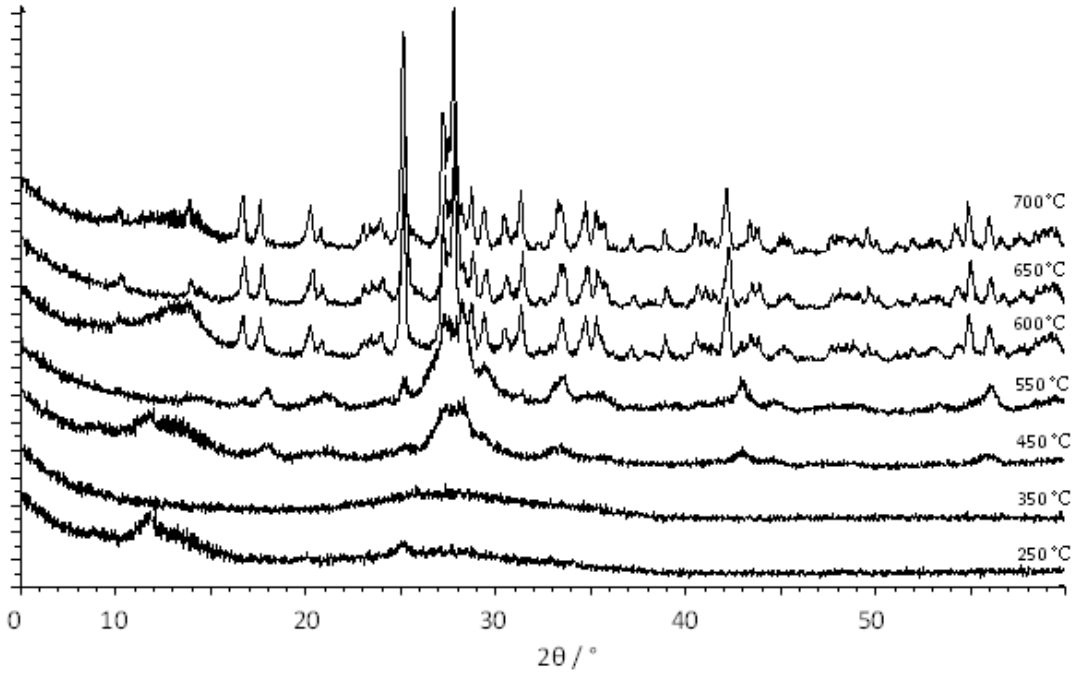

Fig. 3.3 – XRD diffractograms of iron vanadate samples annealed for 50 minutes in oxygen.

As can be seen from fig. 3.3, that all of the XRD patterns of the oxygen annealed samples are similar to the air annealed samples, with regards to the same peak positions, and at what temperatures the peaks appear in those patterns.

For clarity, a comparison of samples annealed at 650 °C in different annealing atmospheres is shown in fig. 3.4 for a clearer comparison between annealing atmospheres. This temperature was chosen in part because it was found that crystalline samples could be produced but lower temperatures afforded samples that were less crystalline.

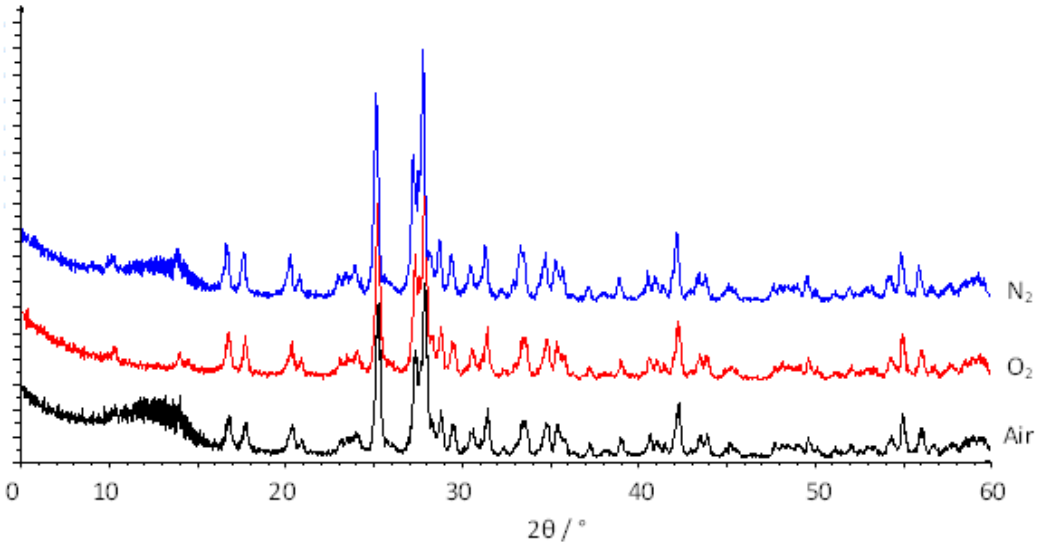

Fig. 3.4 - XRD patterns for iron vanadate powders annealed at 650 °C in oxygen, nitrogen and air for 50 minutes.

Fig. 3.4 shows that all three of the samples annealed at 650 °C produce patterns containing almost identical peak positions and relative intensities, regardless of annealing atmosphere. This similarity was seen regardless of annealing temperature, deducing that the annealing atmosphere did not have a noticeable effect on the sample produced.

3.2 – Infrared Spectroscopy

The products resulting from annealing at set temperatures for 50 minutes in air were analysed by infrared spectroscopy to provide complimentary information to the XRD analysis. The results are shown in fig. 3.5.

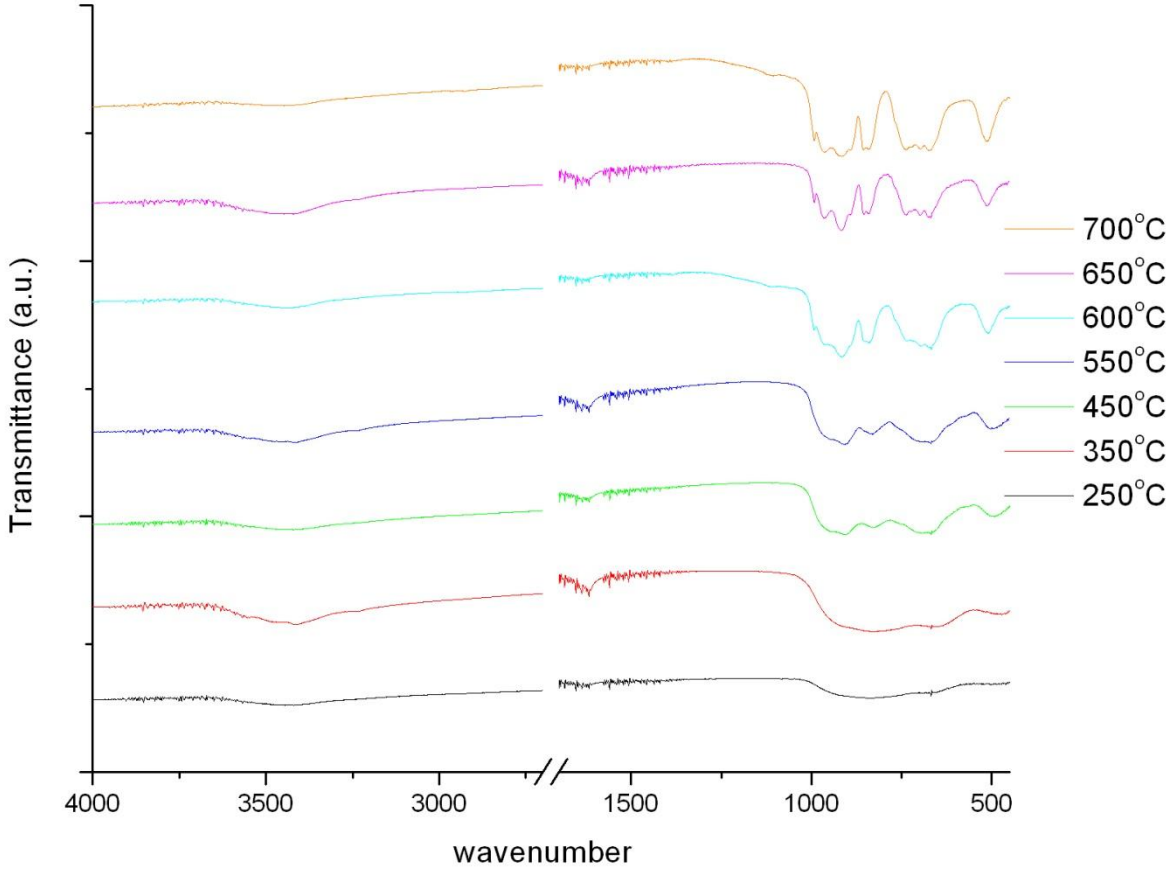

Fig. 3.5 – IR spectra of iron vanadate powders annealed in air for 50 minutes at temperatures between 250-700 °C.

Fig. 3.5 clearly shows a change in chemical composition indicated by a change in spectral profile and intensity as annealing temperature increases, in the temperature ranges of 250-350 °C, 450-550 °C and 600-700 °C, the same as observed in the XRD. The broad peak at *ca.* 3500 cm^{-1} is characteristic of O-H vibrations of H_2O in the sample. The samples annealed at 450 and 550 °C have closely similar spectra indicating the same chemical composition. The region at wavelengths lower than 1300 cm^{-1} seems to contain the majority of the peaks in these spectra. The main peaks being centred around 950 cm^{-1}, which corresponds to VO_4 tetrahedra.[2] The remaining three have similar patterns to each other. There is a general increase in signal intensity with annealing temperature, the most

intense peaks being in samples annealed at 600, 650 and 700 °C. Peaks from FeO_5 and FeO_6 become more apparent at *ca.* 700 cm^{-1}.[2] The strong peaks at *ca.* 500 cm^{-1} in the 600, 650 and 700 ºC, may be α-Fe_2O_3,[3] usually seen at 570 cm^{-1}.[4]

To observe the effect of annealing atmosphere, the precipitation products annealed in nitrogen and oxygen were analysed. The results of IR spectroscopy for samples annealed in nitrogen are shown in fig. 3.6.

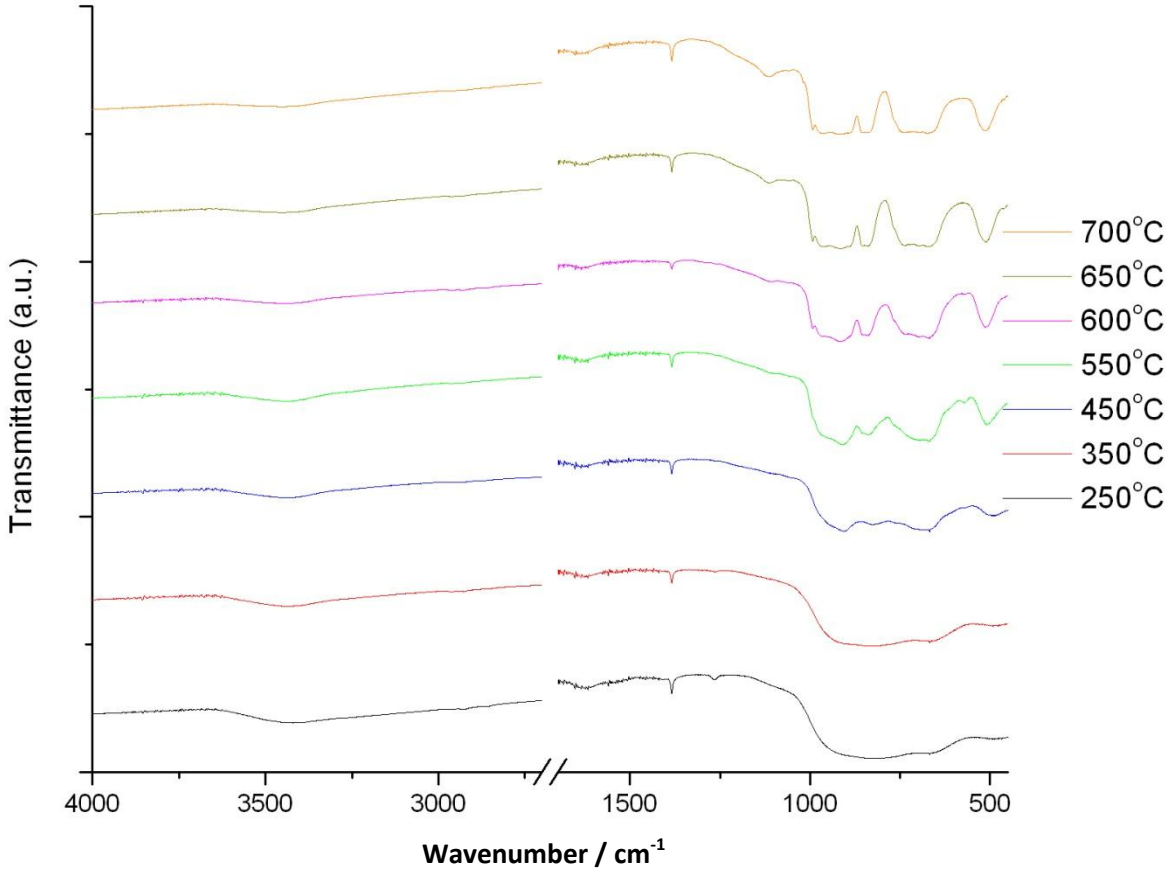

Fig. 3.6 – IR spectra of iron vanadate powders annealed in nitrogen for 50 minutes at temperatures between 250-700 °C.

Fig. 3.6 shows that the IR spectra of the nitrogen annealed samples are very similar to those of the air annealed samples (fig. 3.5). They show that the spectra of the samples annealed at 250 and 350 °C and the spectra of the samples annealed at 450 and 550 °C, mainly contain the peak at *ca.* 950 cm^{-1} corresponding to VO_4 tetrahedra.[2] Finally, the samples annealed at the highest temperatures (600-700 °C) produced IR spectra containing the peak at *ca.* 950 cm^{-1}, as well as peaks from FeO_5 and FeO_6 at *ca.*

700 cm^{-1}.[2] The peak at *ca.* 500 cm^{-1} possibly corresponds to α-Fe_2O_3, usually seen at 570 cm^{-1}.[3, 4]

Once again, the effect of annealing the samples in oxygen on the final iron vanadate product was analysed, this time using IR spectroscopy. The resulting IR spectra are presented in fig. 3.7.

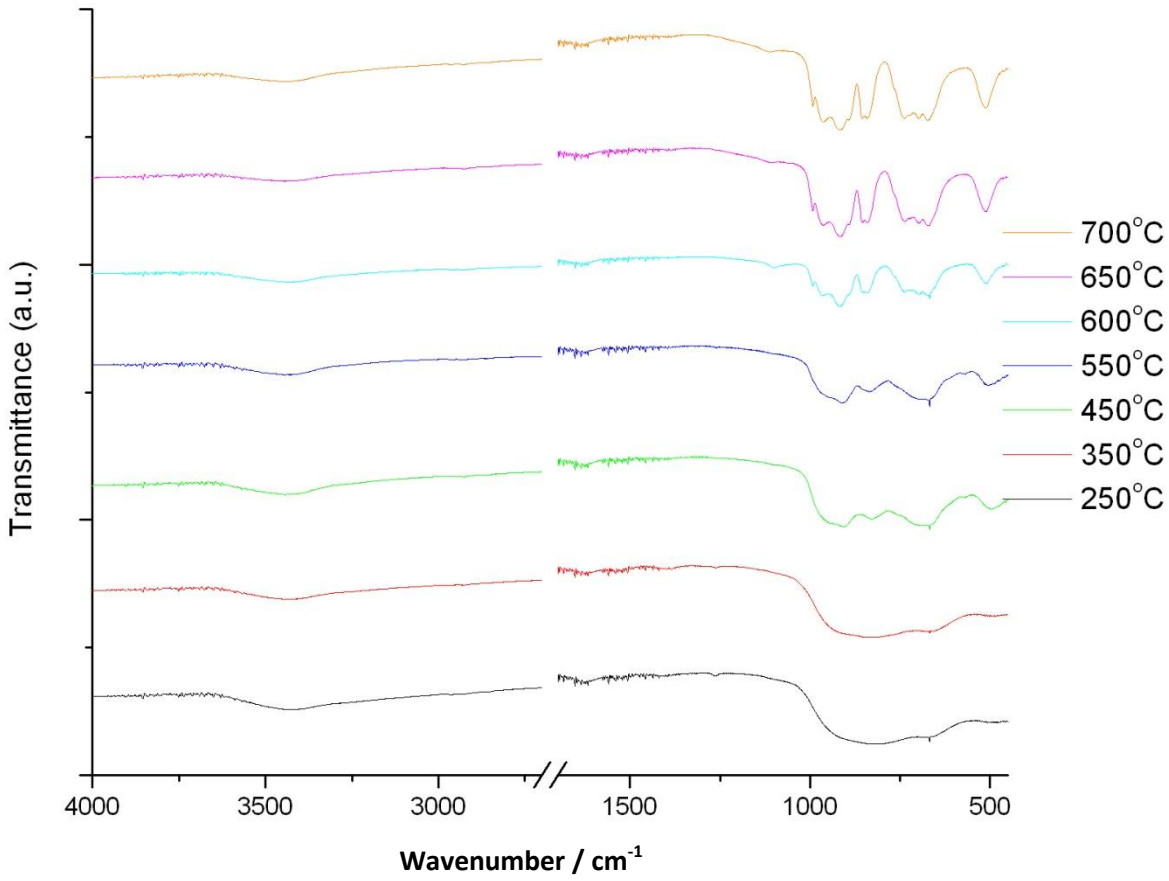

Fig. 3.7 – IR spectra of iron vanadate powders annealed in oxygen for 50 minutes at temperatures between 250-700 °C.

Fig. 3.7 shows that the IR spectra of the oxygen annealed samples are very similar to those of the air and nitrogen annealed samples (fig. 3.5 and fig. 5.6, respectively). The interpretation is therefore similar to that of fig. 3.5 and fig. 3.6. That is, VO_4 tetrahedra present all temperatures,[2] FeO_5 and FeO_6 becoming more visible at temperatures of 450 °C and above, at *ca.* 700 cm^{-1},[2] as well as peaks at *ca.* 500 cm^{-1} possibly due to α-Fe_2O_3.[3, 4] Overall, it appears that there is little, if any difference between the spectra with regards to change of annealing atmosphere.

3.3 – Raman Spectroscopy

As the overall aim was first to characterise the powders produced under particular annealing conditions in order to compare them to thin film electrodes made from deposition of amorphous material followed by annealing, infrared spectrosocpy may be difficult to perform on thin films. As such, Raman microscopy will provide useful information regarding sample crystallinity and composition and has been extensively used to analyse semiconductor thin films.[5-8] To aid interpretation of the films prepared later (see section 2.3), the resulting powder from the precipitiation reaction was annealed first in an air atmosphere for 50 minutes. The results of analysis by Raman microsopy are shown in fig. 3.8.

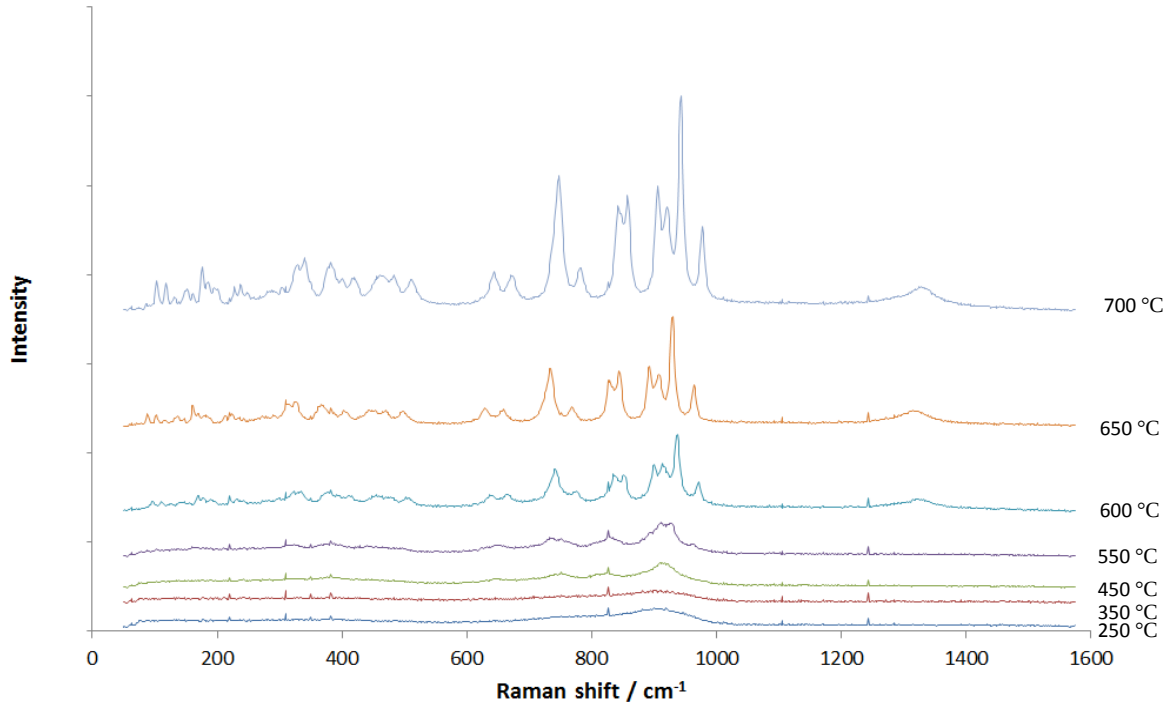

Fig. 3.8 – Raman spectra of iron vanadate powders annealed for 50 minutes in air at the stated temperature.

Fig. 3.8 shows the Raman spectra of air annealed samples. It can be seen that the spectra of the samples annealed at 250 and 350 °C look similar. The broad peak at 912 cm^{-1} may correspond to terminal V-O stretching vibrations in VO_4 tetrahedra,[9] and the shoulder at 760 cm^{-1} correlates to bridging V-O---Fe stretches.[9] The broad nature of the spectral features in these two spectra indicate that the amorphous nature of the product. The samples annealed at 450 and 550 °C produce similar spectra, however there is increased

resolution with the increased annealing temperature. The peak at 395 cm^{-1} can start to be seen which corresponds to V-O-V deformation in $FeVO_4$.[9] A defined peak at 650 cm^{-1} corresponds to mixed bridging V-O---Fe and V---O---Fe stretching[9] and Fe-O-Fe stretching vibrations in FeO_5 distorted trigonal bipyrimidal structures and FeO_6 octahedra in $FeVO_4$.[2] The peaks around 757 and 830 cm^{-1} have also been previously observed in $FeVO_4$,[9, 10] in bridged V-O---Fe stretches. Lastly, there is a peak at 915 cm^{-1} which seems to show the presence of terminal V-O stretching in VO_4 tetrahedra.[2, 9] The Raman spectra from samples annealed at 600, 650 and 700 °C, are similar in peak position. Peaks around 371, 407 and 500 cm^{-1} correspond to V-O-V deformations in $FeVO_4$ tetrahedra.[9, 10] The peaks in the region of 800-600 cm^{-1} correspond to Fe^{3+}-O modes in FeO_6 and FeO_5.[2] Peaks at around 631, 661, 731 and 770 cm^{-1} all seem to correspond to mixed bridging V-O---Fe and V---O---Fe stretching vibrations in $FeVO_4$,[2, 9] while the peaks at 830 and 845 cm^{-1} also correspond to bridging V-O---Fe stretching.[9] Peaks at around 894, 910, 930 and 967 cm^{-1}, correspond to terminal V-O stretching vibrations.[9] Finally, the broad peak at 1325 cm^{-1} is a noticeable characteristic of hematite, α-Fe_2O_3.[3, 11, 12] There may also have been other hematite peaks present, but may not be observable given the number of bands already present from the $FeVO_4$ that may obscure the hematite spectrum. Hematite is expected to display Raman bands at 227, 246, 293, 412, 498 and 610 cm^{-1}.[12] Nevertheless, it should be noted that the band at 1325 cm^{-1} is the strongest band in the hematite spectrum.[11, 12] Therefore the results shown in fig. 3.8 suggest that the quantity of hematite in these samples is comparatively small. These results are summarised in the tables in tab. 3.1. Also, it can be seen that there is a general increase in intensity with increasing annealing temperature, implying that the $FeVO_4$ becomes more crystalline as the annealing temperature increases, which is consistent with the observations derived from the infrared and x-ray diffraction data.

A similar trend was observed when samples were annealed in oxygen or nitrogen atmospheres: the crystallisation of $FeVO_4$ could be followed as a function of temperature and similar spectral profiles were observed. To highlight this, data is presented for $FeVO_4$ annealed at 650 °C for 50 minutes in different annealing atmospheres is shown in fig. 3.9.

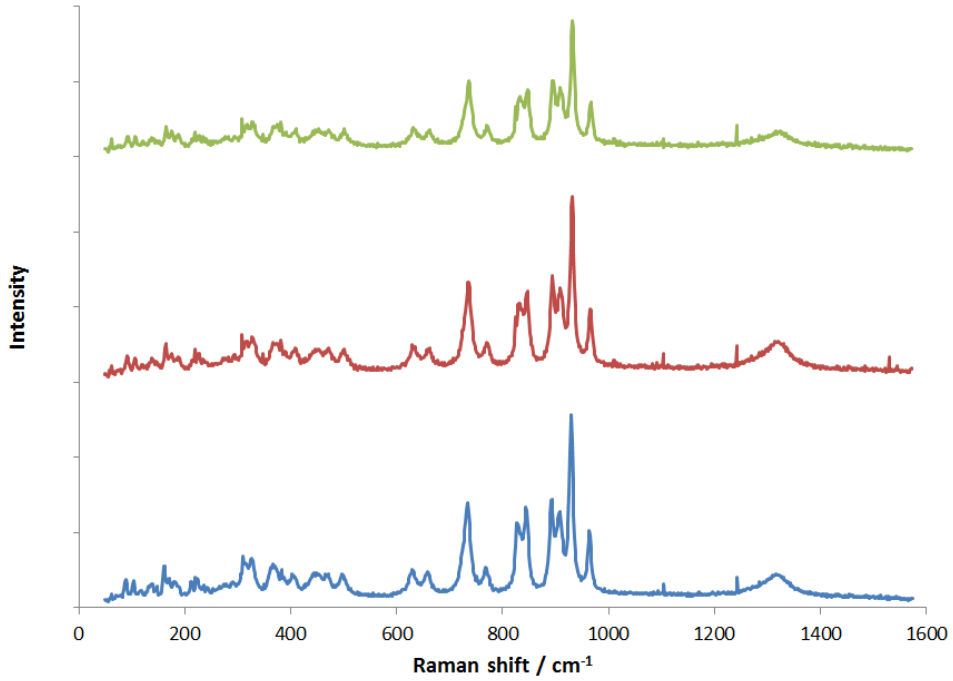

Fig. 3.9 – Raman spectra of iron vanadate annealed in air (*blue*), oxygen (*red*) and nitrogen (*green*) at 650 °C for 50 minutes.

Figure 3.9 demonstrates that the Raman spectra of the iron vanadate powder indicate the similar chemical composition as each other, regardless of annealing atmosphere. The intensity for the sample annealed in nitrogen, however, appears to be slightly less than the others. This could be due to slightly lower crystallinity of the material when annealed in nitrogen. Furthermore, the relative intensity of the hematite band at 1325 cm^{-1} compared to the iron vanadate bands in this sample was slightly less than those observed in atmospheres containing oxygen and air.

3.3.1 – Raman interpretation

Annealing temperature / °C	Band position / cm^{-1}	Assignments	Reference
250 - 350	912	Terminal V-O stretch	**4**
	760	Bridging V-O--Fe Stretching	**4**
450 - 550	915	Terminal V-O stretch	**2, 4**
	830	Bridging V-O--Fe Stretching	**4**
	757	Bridging V-O--Fe Stretching	**4, 5**
	650	Mixed bridging V--O--Fe and V-O--Fe Stretching	**2, 4**
	395	Fe-O Stretching	**4**
600 - 700	1325*	2^{nd} order magnon scattering of α-Fe_2O_3	**3, 6, 7**
	967	Terminal V-O stretch	**4**
	930	Terminal V-O stretch	**4**
	910	Terminal V-O stretch	**4**
	894	Terminal V-O stretch	**4**
	845	Bridging V-O--Fe Stretching	**4**
	830	Bridging V-O--Fe Stretching	**4**
	770	Mixed bridging V--O--Fe and V-O--Fe Stretching	**2, 4**
	731	Mixed bridging V--O--Fe and V-O--Fe Stretching	**2, 4**
	661	Mixed bridging V--O--Fe and V-O--Fe Stretching	**2, 4**
	631	Mixed bridging V--O--Fe and V-O--Fe Stretching	**2, 4**
	500	V-O-V deformations	**4, 5**
	407	V-O-V deformations	**4, 5**
	371	V-O-V deformations	**4, 5**

Tab. 3.1 – Peak assignments of Raman spectra of iron vanadate annealed in air for 50 minutes. All of the peaks reported corresponded to iron vanadate, except that indicated by *, which correspond to hematite, α-Fe_2O_3.

3.4 – Magnetic Susceptibility

Magnetic susceptibility was used in order to determine whether the oxidation state of the iron was what would be expected for iron vanadate, 3+. This was important due to the fact that other iron-containing materials have been observed in previous analysis. From magnetic moment measurements on a Gouy-Chapman balance, it was possible to determine the number of unpaired electrons in a sample. This requires calculation of the magnetic susceptibility, which in turn requires calculation of the molar susceptibility. To do this, it was first necessary to assume that the sample consisted of iron vanadate. The molar susceptibility was calculated from the mass susceptibility by assuming the product was iron vanadate. Following correction for the susceptibilities of the constituent atoms, the magnetic moment was calculated using equation 3.1.[13]

$$\mu = 2.84 (\chi_m \times T)^{1/2} \qquad \text{(Equation 3.1)}$$

where T is temperature (K), μ is the magnetic moment and χ_m is the molar susceptibility.

In order to facilitate comparison between the experimental data, theoretical magnetic moments, μ, were calculated: -

$$\mu = (4S(S+1))^{1/2} \qquad \text{(Equation 3.2)}$$

where S is the spin quantum number. The iron species present in iron vanadate is Fe^{3+},[2, 14-18] and is expected to be of high spin due to its high, extensive coordination within the structure. Given the assumptions above, the number of unpaired electrons should be 5. The theoretical maximum magnetic moment was calculated to be 5.92 B.M.

The results can be summerised in table 3.2.

Annealing temperature / °C	χ_m / x10^{-3} gmol^{-1}	μ / B.M
250	3.806	3.0
350	5.119	3.5
450	8.548	4.5
550	14.02	5.8
600	13.73	5.7
650	9.737	4.8
700	10.30	5.0

Tab. 3.2 – Molar susceptibilities, χ_m and magnetic moments, μ of samples annealed in air.

This can be more clearly seen in fig. 3.10.

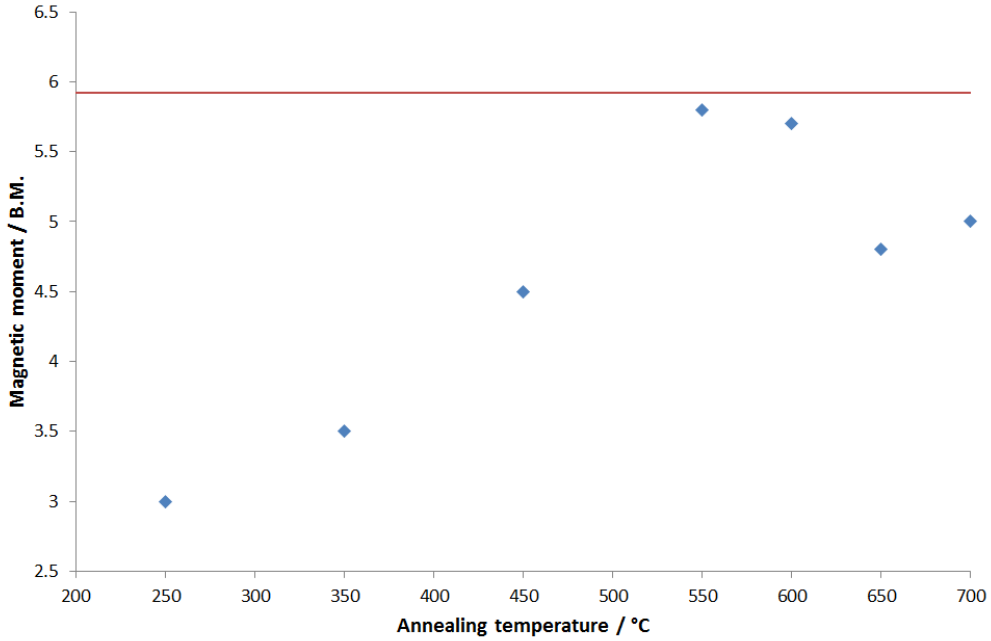

Fig. 3.10 – Change in magnetic moment of iron vanadate powders annealed for 50 minutes in oxygen atmosphere. The theoretical magnetic moment for Fe^{3+} is indicated by the red line.

Fig. 3.10 shows that the magnetic moments increase with annealing temperature until 550 ºC at 5.8 B.M, after which they begin to decrease. The expected magnetic moment for $FeVO_4$ is indicated by the red line, which has a moment of 5.92 B.M. The magnetic moment of other Fe/V systems has shown decrease as well as increase with increasing annealing temperature at lower temperature ranges (50 °C – 250 °C).[19, 20] It has also

previously been reported that the magnetic moment of Fe/V systems reaches a maximum when annealed at 610 °C,[21] slightly higher than the iron vanadate reported in fig. 3.10.

3.5 – Scanning electron microscopy

The characterisation detailed in the previous sections was aimed at determining crystallinity and chemical composition of the resulting powders, both of which will affect the photocatalytic performance of the material.[5, 6, 22] It is equally important to assess the particle size and morphology. To this end, scanning electron microscopy was performed. The results of samples annealed at 350 °C for 50 minutes are detailed in fig. 3.11

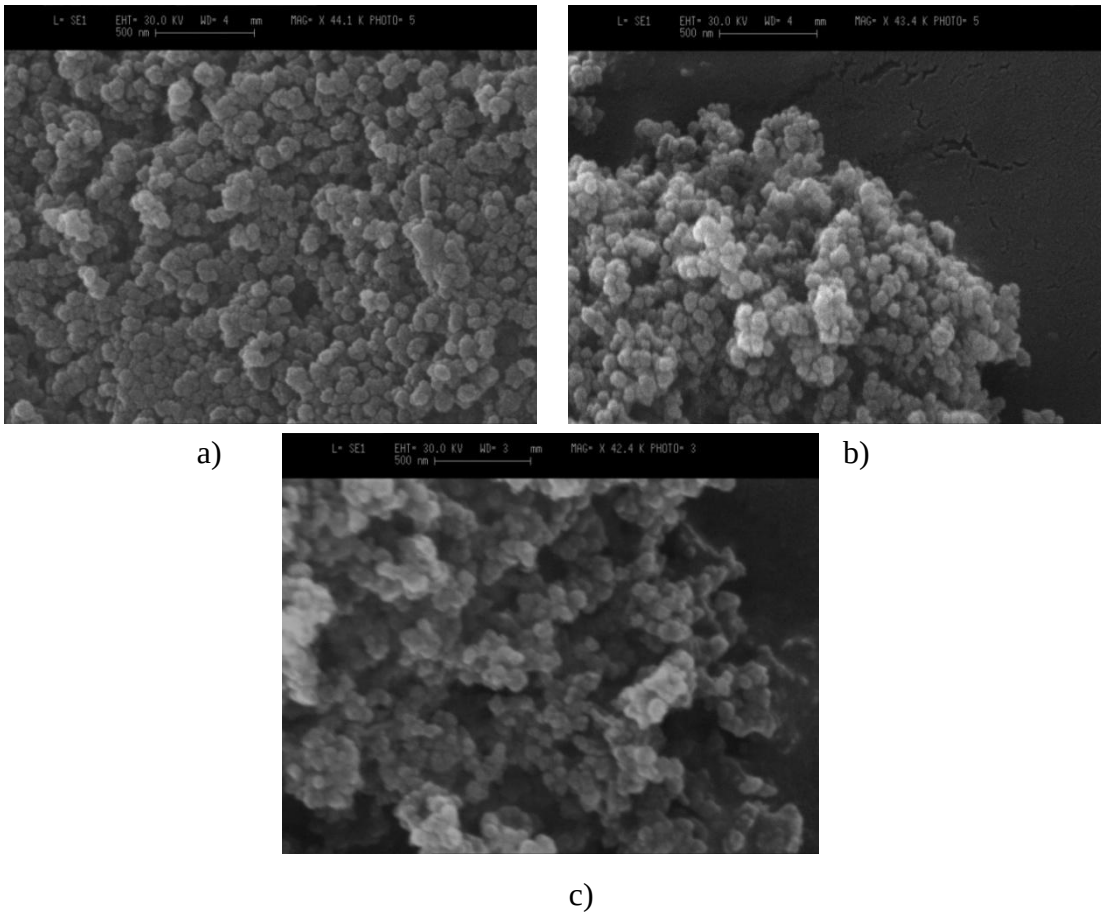

Fig. 3.11 – Micrographs of iron vanadate samples annealed at 350 °C for 50 minutes in a) air, b) nitrogen and c) oxygen.

Fig. 3.11 shows the SEM micrographs of the samples annealed at 350 °C in air, oxygen and nitrogen atmospheres. Particles of between 50-100 nm in diameter were observed in each case. There was no change in the particle size between samples annealed in

different atmospheres. The annealing atmosphere did not appear to influence the observed morphology at any of the annealing temperatures. The response to particle size and morphology to temperature is shown in fig. 3.12 for samples annealed for 50 minutes in air.

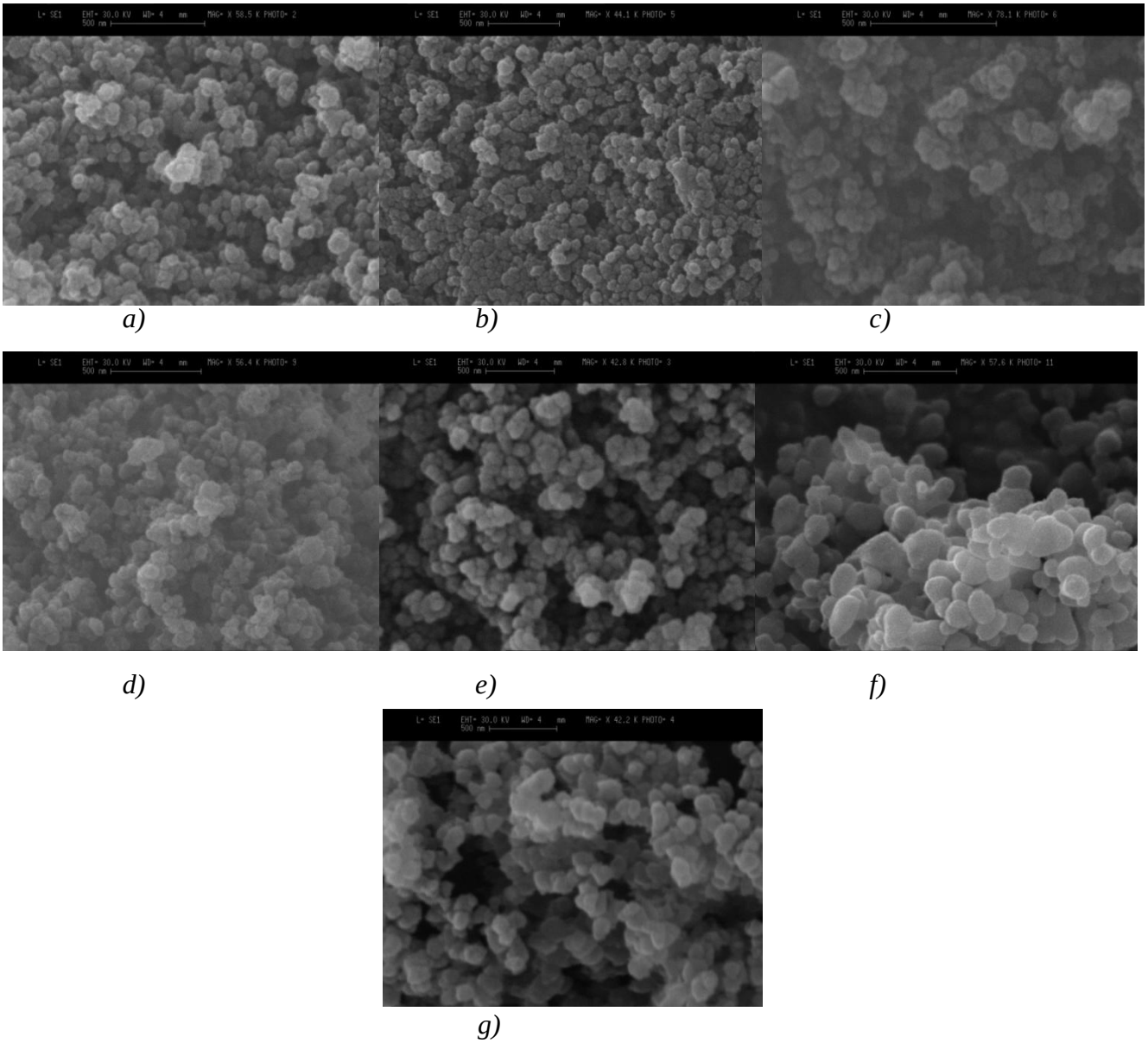

a) *b)* *c)*

d) *e)* *f)*

g)

Fig. 3.12 – Micrographs of iron vanadate samples annealed in air for 50 minutes at a) 250 °C, b) 350 °C, c) 450 °C, d) 550 °C, e) 600 °C, f) 650 °C and g) 700 °C.

Fig. 3.12 above shows how the morphology changes with annealing temperature. Although the particle shape does not appear to change, remaining as rough spherical particles and that the samples are all between 50 and 100 nm in diameter, higher

annealing temperatures caused an increase in the number of particles around 100 nm in diameter, particularly at temperatures above 550 °C, which is evidence of sintering.[23]

3.6 – Diffuse reflectance UV/Vis spectroscopy

One of the most essential characteristics of semiconductors for a particular redox reaction is that of the band gap, both the size of it and the nature of the transition. Once again, crystallinity and chemical composition of the resulting powders, can alter photocatalytic properties of the material, including the band gap.[24] Diffuse reflectance spectroscopy was firstly performed in order to derive Tauc plots, which can be used to determine the nature of the band gap. The results of samples annealed in air, oxygen and nitrogen for 50 minutes at 650 °C are shown in fig. 3.13.

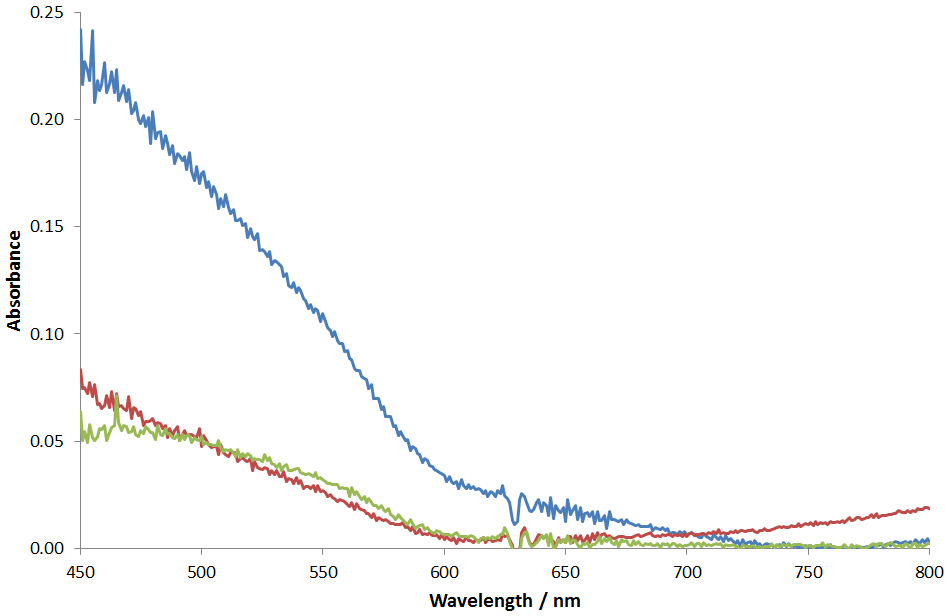

Fig. 3.13 – Diffuse reflectance spectra for iron vanadate samples annealed at 650 °C in air (blue), oxygen (red) and nitrogen (green) for 50 minutes.

Figure 3.13 shows that annealing atmosphere does not appear to affect wavelength range at which the iron vanadate samples absorb light, at below 620 nm. There does, however, appear to be a difference in the absorbance values, but this could be a consequence of different quantities of material in the sample holder.

It is more appropriate to present diffuse reflectance spectra in terms of Kubelka-Munk units, which take scattering into consideration.[25] This was done using the following formula: -

$$Kubelka\ Munk\ unit = \frac{(1-T)^2}{2T} \qquad \text{(Equation 3.3)}^{[26, 27]}$$

where T is transmittance.

The absorbance spectra for iron vanadate samples annealed in air at specific temperatures after conversion to Kubelka-Munk units is shown in fig. 3.14.

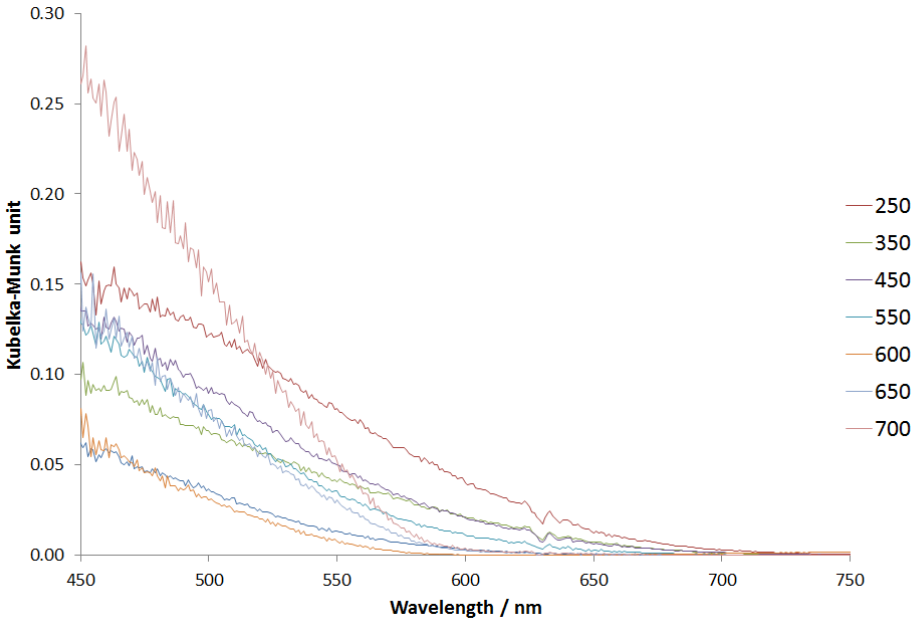

Fig. 3.14 – Diffuse reflectance spectra for iron vanadate samples annealed air for 50 minutes at the stated temperatures (°C), the absorbance has been converted to Kubelka-Munk units.

The Kubelka-Munk plots can then be further used to produce Tauc plots.

The analysis of the data through the use of Tauc plots can offer an estimate of the band gap and an indication into the nature of the optical transition responsible. For example, an extrapolation to the x-axis of the linear portion a plot of $\alpha h\nu^n$ against $h\nu$ will give an estimate of the band gap energy.[25] The nature of the band gap can be determined by examining the most linear Tauc plot for different values of n, where n = ½ for an indirectly allowed electronic transition, and n = 2 for a directly allowed transition.[28] As there are no prior reports of the band gap of iron vanadate, plots of $\alpha h\nu^{1/2}$ and $\alpha h\nu^2$ against photon energy were compared.[29]

Fig. 3.15 and fig. 3.16 show the typical Tauc plots obtained for $\alpha h\nu^2$ and $\alpha h\nu^{1/2}$ respectively. The Tauc analysis has been performed on an un-annealed iron vanadate powder for example.

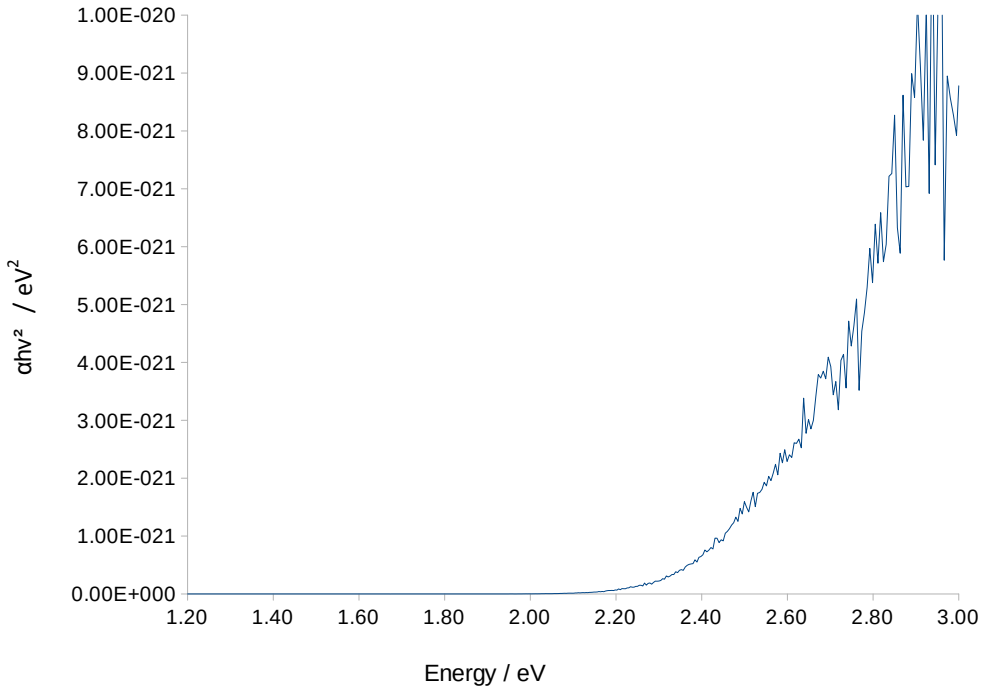

Fig. 3.15 – Typical Tauc plot assuming a direct band gap. The data shown is for a sample prior to annealing.

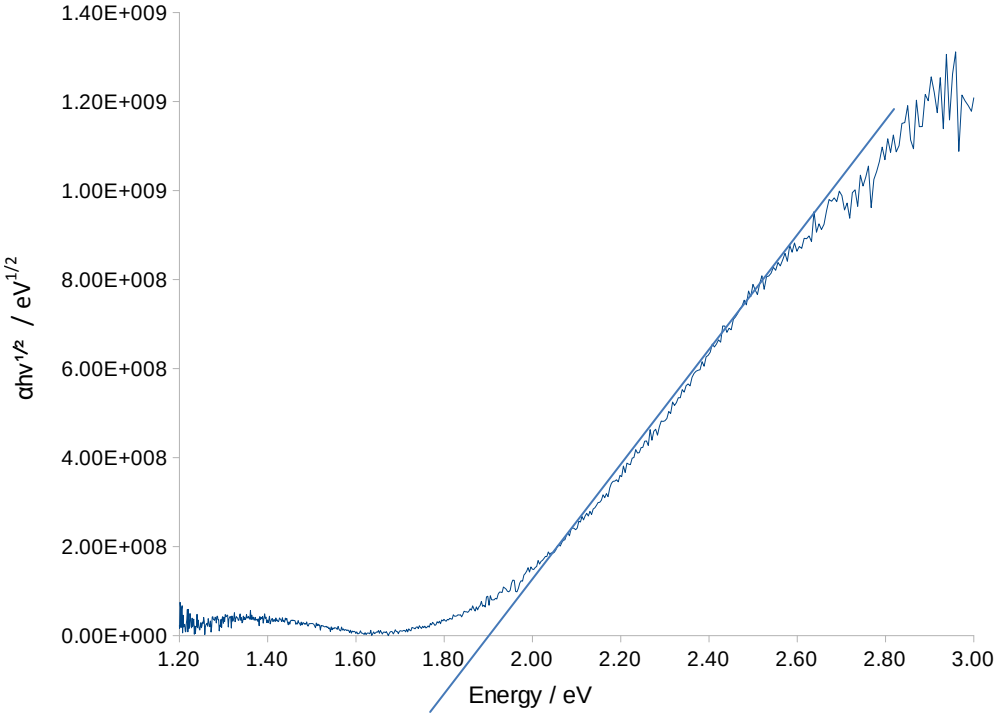

Fig. 3.16 – Tauc plot assuming an indirect band gap. The data shown is for a sample prior to annealing. Extrapolation of the linear region to the x-axis gives an indication of band gap energy.

It can be clearly seen from fig. 3.16 and fig. 3.16 that the Tauc plot using $\alpha h\nu^{1/2}$ gives the most linear region of two, indicating that the band arises from an indirectly allowed optical transition. Indeed, this was the case for all of the samples analysed. To obtain the band gap from the $\alpha h\nu^{1/2}$ Tauc plots, the linear region on the plot were extrapolated down to the x-axis, as shown in fig. 3.16. The band gap is determined by where this extrapolation intercepts the x-axis.

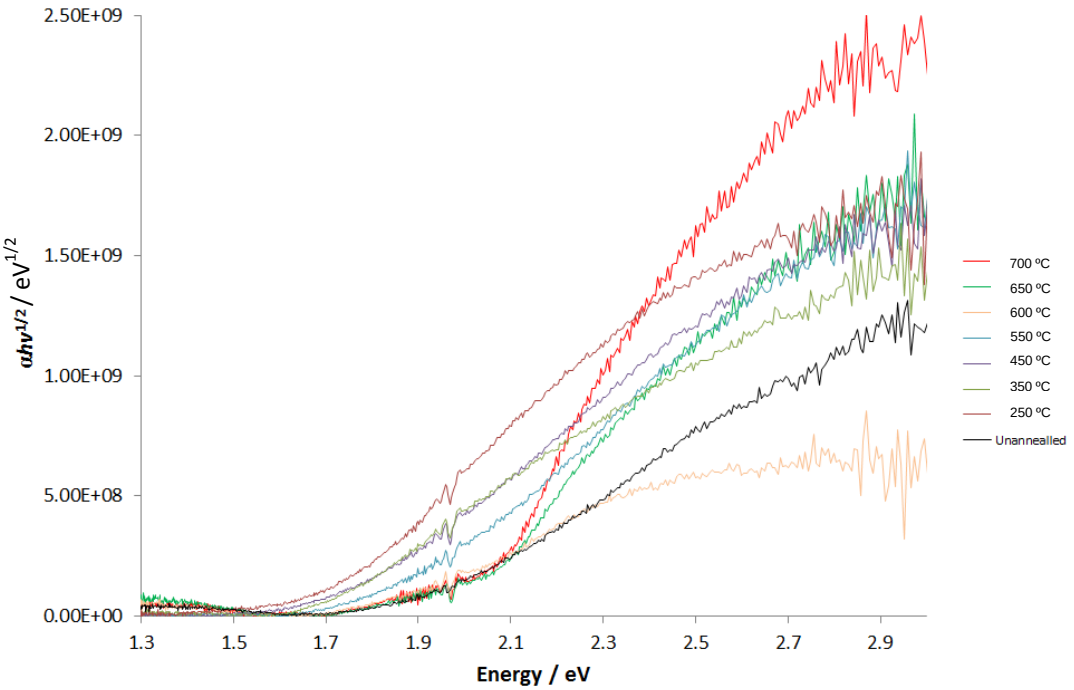

Fig. 3.17 – Tauc plots assuming an indirect band gap for iron vanadate powders annealed in air for 50 minutes at stated temperatures.

Following a similar analysis to that shown in fig 3.16, the optical band gap was determined for all temperatures, *e.g.* all temperatures annealed in air, from the spectra in Fig. 3.17. In addition, the same analysis was performed for powders annealed in oxygen and in nitrogen. The results are detailed in Table 3.3. Band gap energies are given in electron-volts and a corresponding photon wavelength for comparison.

Annealing temperature / °C	Band gap / eV			λ / nm		
	Oxygen	Air	Nitrogen	Oxygen	Air	Nitrogen
none	1.88	1.88	1.88	659	659	659
250	1.77	1.65	1.70	700	751	729
350	1.70	1.63	1.65	729	761	751
450	1.70	1.70	1.68	729	729	738
550	1.77	1.81	1.72	700	685	721
600	1.92	2.03	1.98	646	611	626
650	2.10	1.98	2.07	590	626	599
700	2.09	2.03	2.07	593	611	599

Tab. 3.3 – Band gap energies for iron vanadate samples annealed for 50 minutes.

For easier visual comparison, the data are summarised in fig. 3.18.

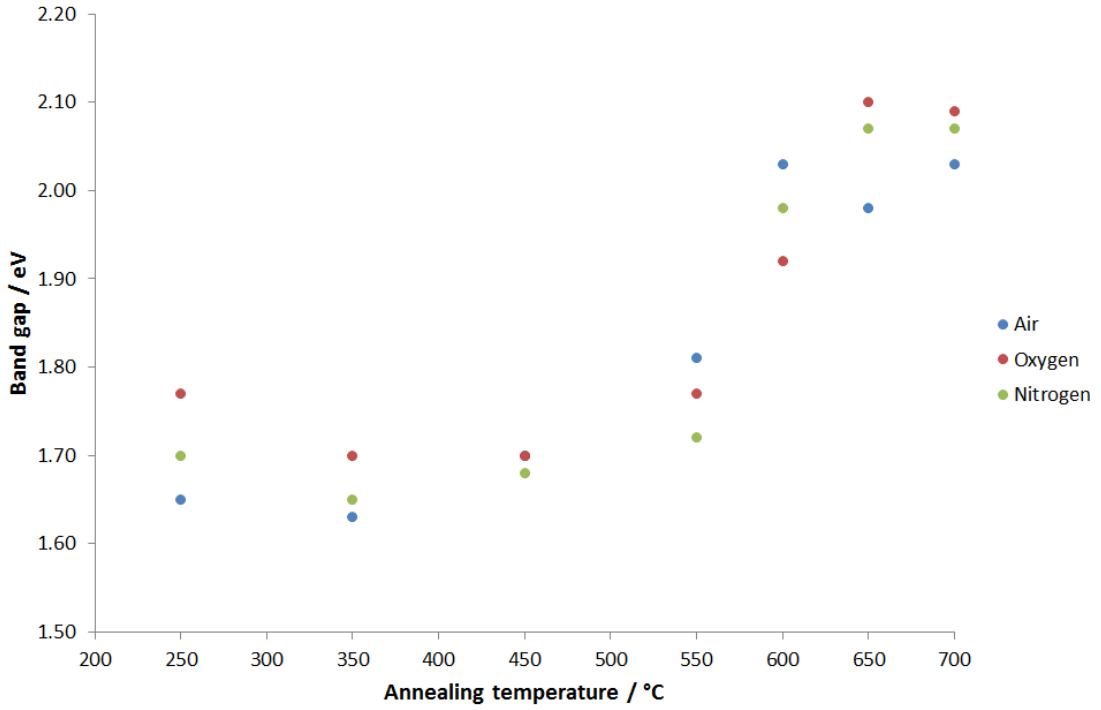

Fig. 3.18 – Summary of band gap energies for iron vanadate samples annealed for 50 minutes. The atmosphere of annealing is given in the legend.

Taking into account the possible errors with extrapolation, it appears from fig. 3.18 that the band gap energies are fairly constant at annealing temperatures below 550 °C, where there is an increase, coinciding with change in phase as shown in the Raman spectroscopy and XRD. It therefore appears that the estimated band gap energy is dependent on the

apparent crystallinity of the material, which has been widely reported in semiconductors.[30-34]

The band gap of the most crystalline materials is within the desirable range required for water-splitting, when taking losses in the system into account.[35] These band gap energies are smaller than some of the most researched and reported photocatalysts in literature, TiO_2 (3.2-3.1 eV),[35-37] WO_3 (2.7-2.6 eV)[35-37] and Fe_2O_3 (2.3-2.1 eV),[35-37] as well as other vanadates, $BiVO_4$ (2.6-2.4 eV)[5, 7, 34, 38] and $InVO_4$ (3.2 eV),[6] indicating that $FeVO_4$ has the potential rival them.

3.7 – Conclusions

Iron vanadate powder was made from a low temperature aqueous precipitation synthesis. It was then annealed at specific temperatures in different atmospheres, before being characterised by XRD, Infrared spectroscopy, Raman spectroscopy and SEM to determine the structural properties. Crystallinity, band gap and particle size of the material increased with annealing temperature. At lower temperatures, the material is amorphous and contains VO_4 tetrahedra. At higher temperatures, *e.g.* above 550 °C, the material was more crystalline and contained VO_4 tetrahedra, FeO_5 distorted triganol bipyramids, FeO_6 octahedra in triclinic iron vanadate. Small quantities of Fe_2O_3 were also observed in some samples. The most crystalline materials were shown to have an indirect band gap of *ca.* 2.00 eV.

3.8 – References

1. *PDF-2 Release 2008*, Kabekkodu, S.N., Ed.; International Centre for Diffraction Data: Newtown Square, PA, 2008.

2. S. Bencic, B. Orel, A. Surca and U. L. Stangar, *Solar Energy*, 2000, **68**, 499-515.

3. V. C. Farmer, *The Infrared Spectra of Minerals*, Mineralogical Society, Middlesex, UK, 1974.

4. A. S. Al-Kady, M. Gaber, M. M. Hussein and E.-Z. M. Ebeid, *Spectrochimica acta. Part A, Molecular and biomolecular spectroscopy*, 2011, **83**, 398-405.

5. M. T. Li, L. A. Zhao and L. J. Guo, *International Journal of Hydrogen Energy*, 2010, **35**, 7127-7133.

6. C. S. Enache, D. Lloyd, M. R. Damen, J. Schoonman and R. V. de Krol, *Journal of Physical Chemistry C*, 2009, **113**, 19351-19360.

7. B. D. Alexander, P. J. Kulesza, L. Rutkowska, R. Solarska and J. Augustynski, *Journal of Materials Chemistry*, 2008, **18**, 2298-2303.

8. X. Chen and S. S. Mao, *Chemical Reviews*, 2007, **107**, 2891-2959.

9. A. S. Vuk, B. Orel, G. Drazic, F. Decker and P. Colomban, *Journal of Sol-Gel Science and Technology*, 2002, **23**, 165-181.

10. G. S. Li, D. Q. Zhang and J. C. Yu, *Chemistry of Materials*, 2008, **20**, 3983-3992.

11. D. L. A. de Faria, S. V. Silva and M. T. de Oliveira, *Journal of Raman Spectroscopy*, 1997, **28**, 873-878.

12. D. L. A. de Faria and F. N. Lopes, *Vibrational Spectroscopy*, 2007, **45**, 117-121.

13. P. N. Kotru and K. K. Raina, *Journal of Physics D-Applied Physics*, 1986, **19**, 9-11.

14. D. Klissurski, R. Iordanova, D. Radev, S. Kassabov, M. Milanova and K. Chakarova, *Journal of Materials Science*, 2004, **39**, 5375-5377.

15. M. Kurzawa and E. Tomaszewicz, *Spectrochimica Acta Part a-Molecular and Biomolecular Spectroscopy*, 1999, **55**, 2889-2892.

16. Z. Z. He, J. I. Yamaura and Y. Ueda, *Journal of Solid State Chemistry*, 2008, **181**, 2346-2349.

17. Y. Oka, T. Yao, N. Yamamoto, Y. Ueda, S. Kawasaki, M. Azuma and M. Takano, *Journal of Solid State Chemistry*, 1996, **123**, 54-59.

18. K. Melghit and A. S. Al-Mungi, *Materials Science and Engineering B-Solid State Materials for Advanced Technology*, 2007, **136**, 177-181.

19. D. Labergerie, K. Westerholt, H. Zabel and B. Hjorvarsson, *Journal of Magnetism and Magnetic Materials*, 2001, **225**, 373-380.

20. J. Cieslak, B. F. O. Costa, S. M. Dubiel, M. Reissner and W. Steiner, *Journal of Magnetism and Magnetic Materials*, 2009, **321**, 2160-2165.

21. J. F. M. Borges, M. I. da Costa, J. B. M. da Cunha and M. C. M. Alves, *Journal of Magnetism and Magnetic Materials*, 2001, **226**, 1761-1763.

22. A. A. Tahir, K. G. U. Wijayantha, M. Mazhar and V. McKee, *Thin Solid Films*, 2010, **518**, 3664-3668.

23. O. R. Camara and S. Trasatti, *Electrochimica Acta*, 1996, **41**, 419-427.

24. A. Zhang and J. Zhang, *Spectrochimica Acta Part a-Molecular and Biomolecular Spectroscopy*, 2009, **73**, 336-341.

25. A. B. Murphy, *Solar Energy Materials and Solar Cells*, 2007, **91**, 1326-1337.

26. J. J. Li, K. Chatterjee, A. Medek, E. Shalaev and G. Zografi, *Journal of Pharmaceutical Sciences*, 2004, **93**, 697-712.

27. K. Ichimura, A. Funabiki, K. I. Aoki and H. Akiyama, *Langmuir*, 2008, **24**, 6470-6479.

28. W. Yao, H. Iwai and J. Ye, *Dalton Transactions*, 2008, 1426-1430.

29. Z. G. Zou, J. H. Ye and H. Arakawa, *Topics in Catalysis*, 2003, **22**, 107-110.

30. G. Tian, H. Fu, L. Jing and C. Tian, *Journal of Hazardous Materials*, 2009, **161**, 1122-1130.

31. J.-W. Jeon, D.-W. Jeon, T. Sahoo, M. Kim, J.-H. Baek, J. L. Hoffman, N. S. Kim and I.-H. Lee, *Journal of Alloys and Compounds*, 2011, **509**, 10062-10065.

32. T. P. Kumar, S. Saravanakumar and K. Sankaranarayanan, *Applied Surface Science*, 2011, **257**, 1923-1927.

33. R. Elilarassi and G. Chandrasekaran, *Materials Chemistry and Physics*, 2010, **121**, 378-384.

34. H. Jiang, H. Endo, H. Natori, M. Nagai and K. Kobayashi, *Journal of the European Ceramic Society*, 2008, **28**, 2955-2962.

35. T. Bak, J. Nowotny, M. Rekas and C. C. Sorrell, *International Journal of Hydrogen Energy*, 2002, **27**, 991-1022.

36. M. Gratzel, *Nature*, 2001, **414**, 338-344.

37. K. Sivula, F. Le Formal and M. Graetzel, *Chemsuschem*, 2011, **4**, 432-449.

38. K. Sayama, A. Nomura, T. Arai, T. Sugita, R. Abe, M. Yanagida, T. Oi, Y. Iwasaki, Y. Abe and H. Sugihara, *Journal of Physical Chemistry B*, 2006, **110**, 11352-11360.

4 – PHOTOANODES PREPARED FROM PRE-FORMED NANOPARTICLES

4.1 – Optimisation of synthesis method

Nanoparticles of $FeVO_4$ precursor material made as the result of a low-temperature precipitation reaction[1, 2, 3] were suspended in a 20 w/v % solution of PVDF in DMF.[4] This suspension was then dropped onto a substrate, and the excess removed, producing a film, which was then annealed. In the first case, the film was annealed at 550 °C whilst the effect of annealing time and number of depositions was investigated.

4.1.1 – Raman spectroscopy

Raman microscopy will once again provide useful information regarding sample crystallinity and composition and has been extensively used to analyse semiconductor thin films previously.[5-8] Five areas of each electrode film were analysed, in order to observe the uniformity of the films. The results of analysis by Raman microsopy are shown in fig. 4.1.

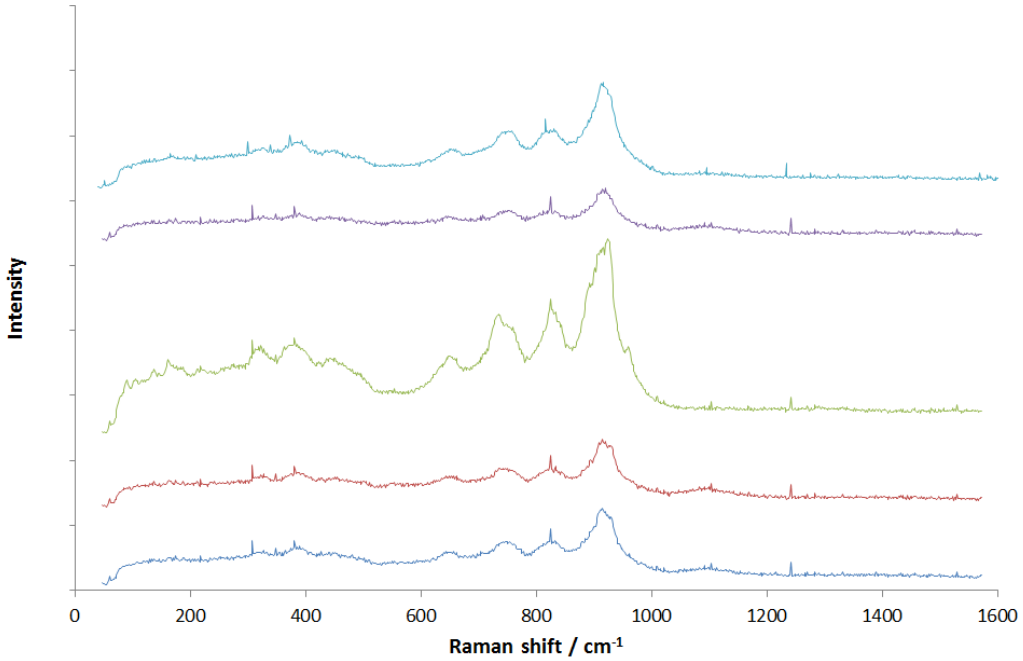

Fig. 4.1 – Raman spectra recorded from five points on the surface of a 6-layer electrode annealed at 550 °C. Following each deposition, the electrode was annealed for 10 minutes.

As can be seen from figure 4.1, there are a number of peaks observed. The peak at 395 cm^{-1} corresponds to V-O-V deformation in $FeVO_4$.[9] The peak at 660 cm^{-1} may be due to the previously observed band at 650 cm^{-1} assigned to a mixture of bridging V-O---Fe and V---O---Fe stretching[9] and Fe-O-Fe stretching vibrations in FeO_5 distorted trigonal bipyrimidal structures and FeO_6 octahedra in $FeVO_4$.[10] The peaks observed at *ca.* 745 and 829 cm^{-1} are assigned to $FeVO_4$,[9, 11] bridged V-O---Fe stretches. The peak at 910 cm^{-1} is due to the presence of terminal V-O stretching in VO_4 tetrahedra.[9, 10] These spectra were very similar to those that were observed seen in the previous chapter for the iron vanadate powder annealed at 550 °C. The band position and relative intensities are consistent at each of the five points on the surface analysed, indicating a homogeneous chemical composition at the points analysed. The absolute intensity differences could be a result of the film varying in thickness although small variations in intensity are also expected due to variation in laser focusing.

The electrode films were also annealed for 30 minutes per layer, in order to observe how increased annealing alters the structural properties of the film and whether it improves crystallinity and resultantly improves photo-electrochemical performance.

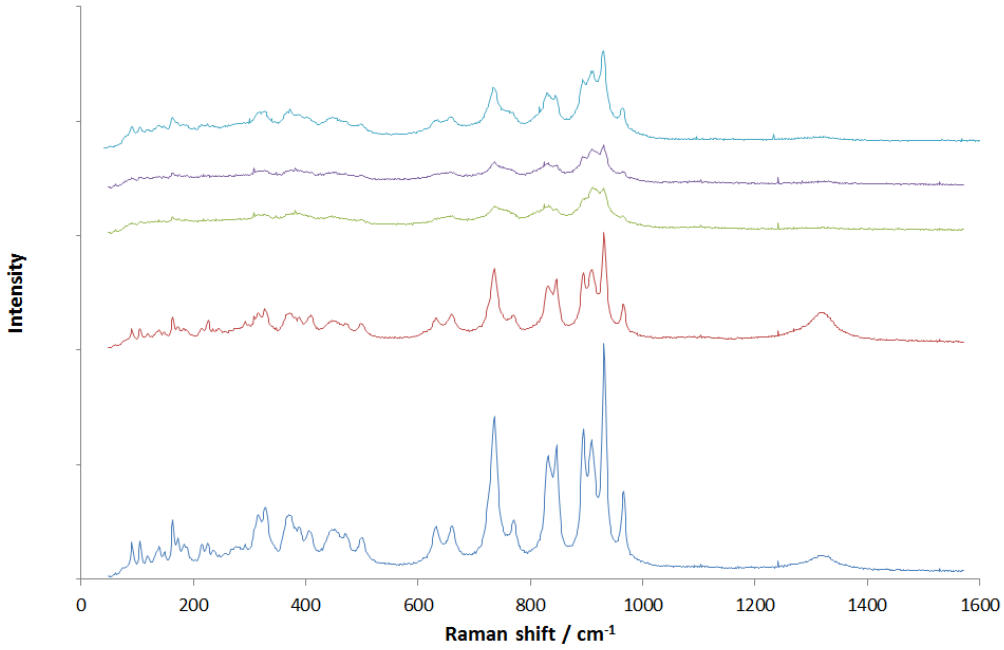

Fig. 4.2 – Raman spectra recorded from five points on the surface of a 6-layer electrode annealed at 550 °C. Following each deposition, the electrode was annealed for 30 minutes.

The Raman spectra of electrodes annealed for 30 minutes, seen in figure 4.2, displayed a stronger signal and had more clearly defined bands than the corresponding spectra for electrodes annealed for 10 minutes. Bands observed at *ca.* 374, 409 and 503 cm^{-1} are assigned to V-O-V deformations in VO_4 tetrahedra in $FeVO_4$.[9, 11] Peaks produced in the region of 800-600 cm^{-1} arise from Fe^{3+}-O modes in FeO_6 and FeO_5.[10] Peaks at 635, 663, 732 and 773 cm^{-1} correlate to mixed bridging V-O---Fe and V---O---Fe stretching vibrations in $FeVO_4$,[9, 10] and bands at 831 and 848 cm^{-1} also correspond to bridging V-O---Fe stretching.[9] Peaks at 898, 904, 936 and 961 cm^{-1}, correlate to terminal V-O stretching vibrations.[9] The broad band at 1325 cm^{-1} is a noticeable peak of hematite, α-Fe_2O_3.[12-14] There is a high possibility that there are more bands corresponding to hematite, which may be hidden by other bands (227, 246, 293, 412, 498 and 610 cm^{-1}).[13] Although the additional iron vanadate bands are seen, they are not seen for all points analysed. This could indicate that the film was between two crystallinity phases. Overall, there seems to be a large increase in crystallinity with annealing time as indicated by the fact that spectra with sharper bands are more clearly resolved for more crystalline samples, for example, iron vanadate powder annealed at temperatures above 550 °C (fig. 3.8).

4.2 – Film characterisation

The effect of the quantity of annealing cycles and annealing atmosphere, on the resultant surface morphology of the film was investigated. Changing the annealing atmosphere could alter the crystallinity, as was observed in the previous chapter when annealing the powder. The subsequent longer total annealing time implied by the increase in the number of layers deposited could alter particle size and crystallinity of the film. Three different electrodes were made at 650 °C (due to the fact this annealing temperature produced a crystalline film with a relatively high photocurrent shown in figure 4.6) and analysed using XRD, SEM, EDX and UV/Vis spectroscopy. The electrodes were a 6-layer electrode annealed in oxygen, a 6-layer electrode annealed in nitrogen and a 3-layer electrode annealed in oxygen, therefore comparing oxygen and nitrogen annealing atmospheres, and 3 and 6 layers.

XRD analysis was done in order to observe the crystallite phases present within the films, and to see whether they differ depending on the film production. Thin film XRD is difficult due to the miniscule quantity of sample being analysed, smaller than the penetration depth of the incident X-ray. As a consequence, data will also be collected from the substrate upon which, the film is fixed. The electrode films analysed were a) annealed in oxygen and contained 6 layers, b) annealed in oxygen and contained 3 layers, and c) annealed in nitrogen and contained 6 layers. All layers were annealed at 650 °C for 10 minutes each. The resultant XRD diffractograms are shown in fig. 4.3.

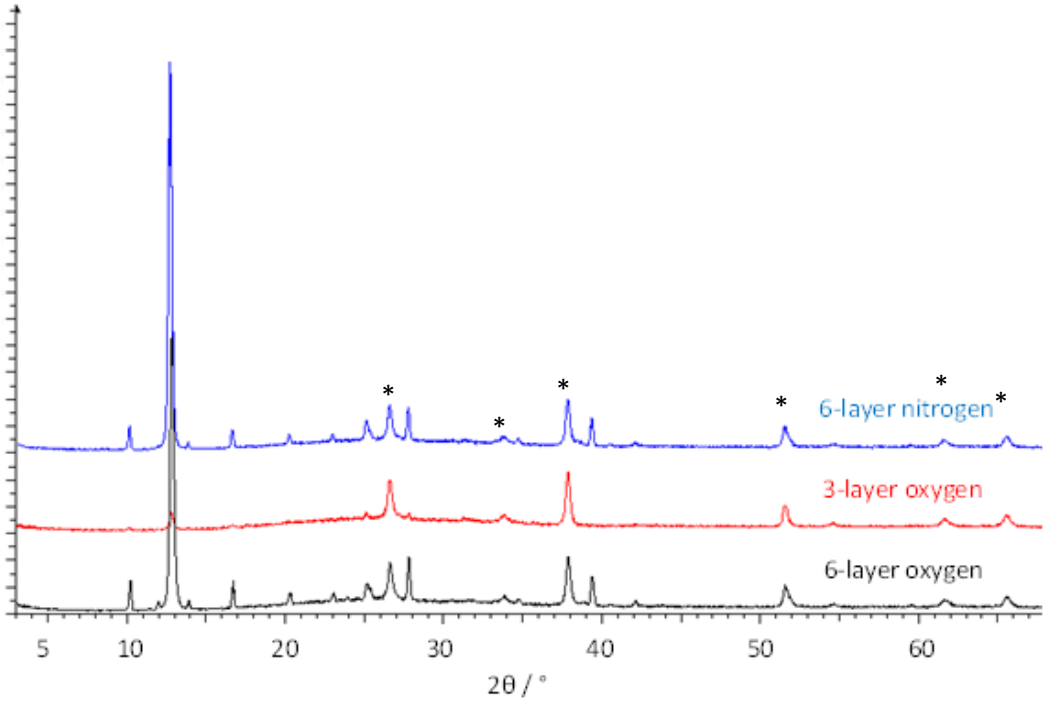

Fig. 4.3 – XRD patterns of the three electrodes, as labelled to the right of each pattern. Peaks corresponding to the tin oxide conductive layer are indicated by *.

The XRD patterns in figure 4.3 show evidence of hematite (Fe_2O_3) at very weak peaks of 36.5°, 39.5° and 41° 2θ, and tin oxide (found in the conductive FTO layer of the electrode) at 26.5°, 34°, 38°, 51.5°, 61.5° and 65.5° 2θ. The remaining peaks, apart from the peak at 13° 2θ, correspond to triclinic iron vanadate. It is possible that the peak at 13° 2θ may correspond to monoclinic iron vanadium oxide, $Fe_2V_4O_{13}$, due to an excess of vanadium in the layer, although as only one signal is detected for $Fe_2V_4O_{13}$, this is far from conclusive.

It can be seen that the patterns do not appear to be affected by the annealing atmosphere, but are affected by the number of layers. It was observed that the intensity of the peaks corresponding to the materials in the film were increased with the increasing number of layers, and film thickness, as could be expected given that the film thickness is critical to the amount of material probed by the incident x-rays.

SEM microscopy was undertaken upon the films in order to observe how the particle size and shape was altered in relation to the annealing conditions. The electrode films analysed were a) annealed in oxygen and contained 6 layers, b) annealed in oxygen and contained 3 layers, and c) annealed in nitrogen and contained 6 layers. All layers were annealed at 650 °C for 10 minutes each. The resultant micrographs are shown in fig. 4.4.

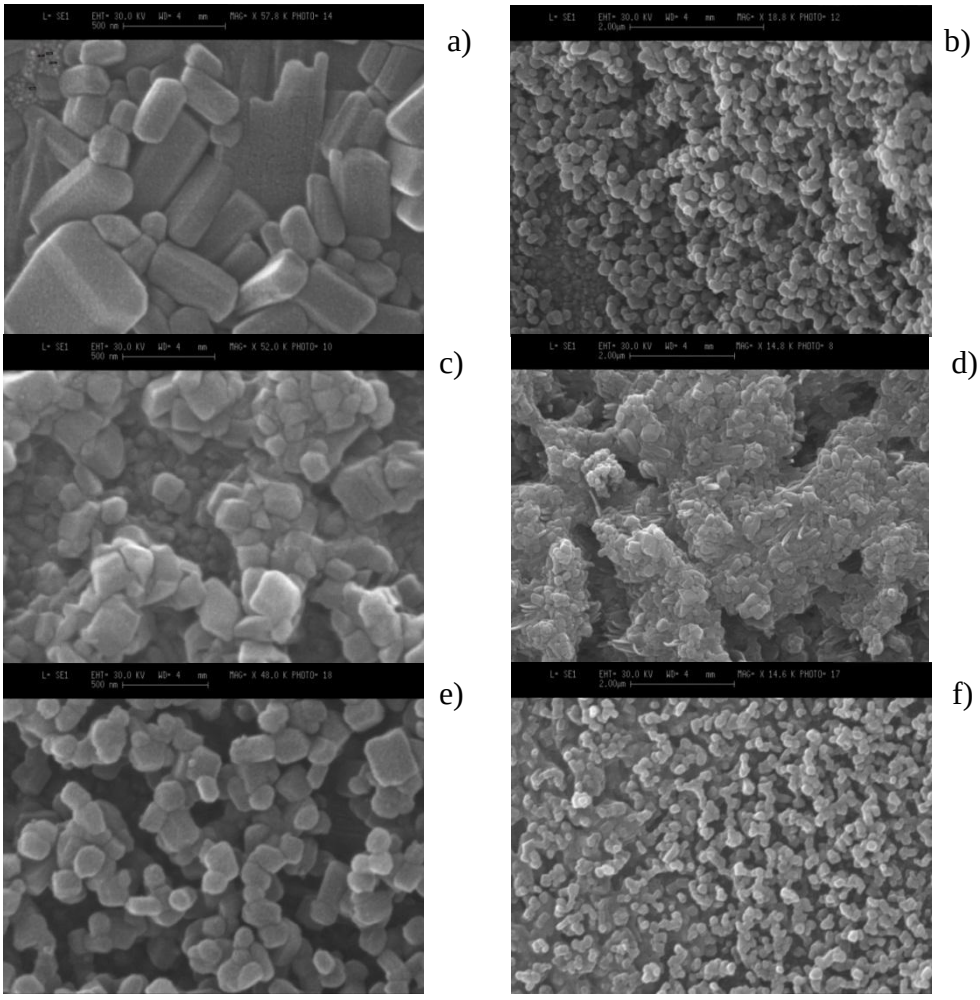

Fig. 4.4 – SEM micrographs of iron vanadate films, annealed in nitrogen and contained 6 layers (a-b), annealed in oxygen and contained 6 layers (c-d), and annealed in oxygen and contained 3 layers (e-f). All layers were annealed at 650 °C for 10 minutes each. For micrographs a, c and e, magnification of 48,000-58,000 x was used. For micrographs b, d and f, magnifications of 14,000-19,000 x were used.

It is observed from figure 4.4 that generally, particles seem to be just over 100 nm in diameter, but there is also a small number which are larger than this. It can be seen that the films appear porous in areas. The film annealed in nitrogen (fig. 4.4a-b) appeared to show cuboidic particles, whereas the other two films contained more rounded particles. Figure 4.4e-f shows that in the film containing 3 layers, the particle distribution seems more uniform.

UV/Vis data was taken of the three films in order to determine whether the band gap changes depending on annealing atmosphere or number of layers. Once again, the films analysed were a) annealed in oxygen, containing 6 layers, b) annealed in oxygen, containing 3 layers, and c) annealed in nitrogen, containing 6 layers. All layers were annealed at 650 °C for 10 minutes each. The resultant spectra are shown in fig. 4.5.

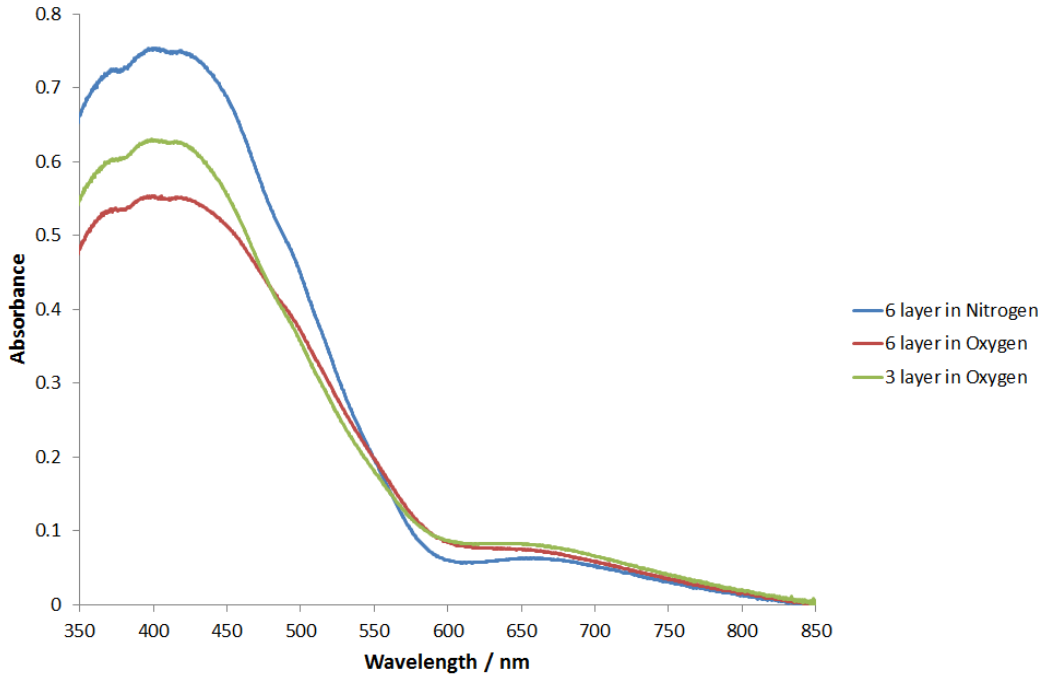

Fig. 4.5 – Diffuse reflectance UV/Vis spectra of all three electrodes as stated on the right of the figure.

Figure 4.5 shows that there is only a marginal change in the UV/Vis spectra of the three electrodes films, however, the spectrum for the electrode annealed in nitrogen is slightly different and the relative intensities of the two peaks are different. The maximum absorbances for all three seem to be at the same wavelengths, however, the slopes are slightly different. The two electrodes annealed in oxygen appear to be similar. Tauc analysis of the above data for an indirect and a direct band gap are shown in figures 4.6 and 4.7.

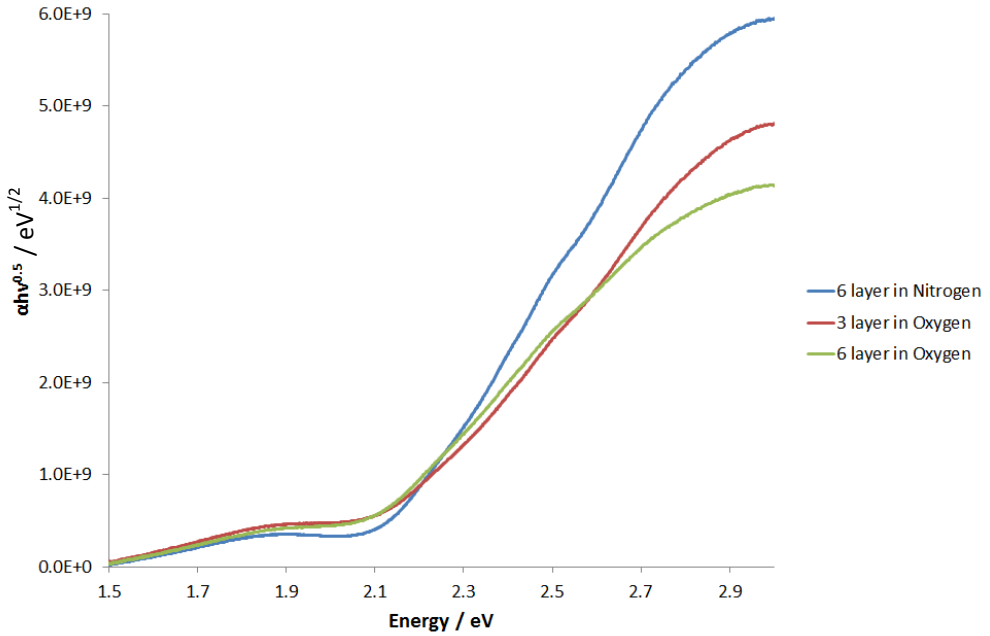

Fig. 4.6 – Tauc plots of all three electrodes, where the Tauc equation has been applied with n = 0.5, indicating an indirect band gap.

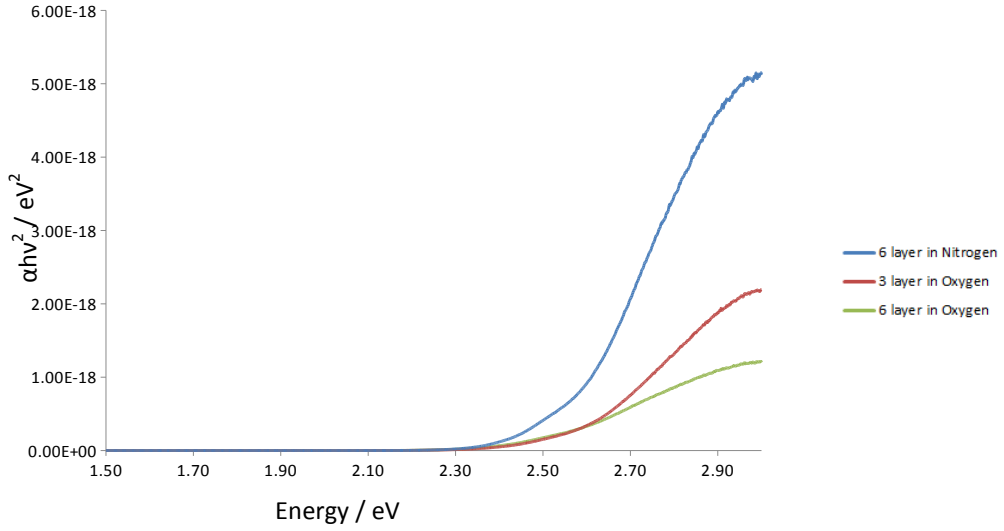

Fig. 4.7 – Tauc plots of all three electrodes, where the Tauc equation has been applied with n = 2, indicating a direct band gap.

It was observed that the Tauc plots corresponding to an indirect band gap (shown in figure 4.6) were most suitable for the data obtained, compared with data for a direct band gap (figure 4.7).[15] Extrapolation of the linear section of the graph indicates band gaps of between 2.0 and 2.1 eV, the electrodes annealed in oxygen produce the slightly shorter band gap. This could possibly be due to oxygen vacancy defects with the film annealed

in nitrogen.[16] These results seem to correspond to what was observed with the powder: between 2.0-2.1 eV at the same temperature.

The films were analysed by energy dispersive x-ray spectroscopy in order to observe the elemental make-up and of the material. This was done to determine whether the ratio of iron and vanadium deviated from the theoretical 1:1, and also to see whether there were any impurities, that may radically affect the photocurrent densities observed.

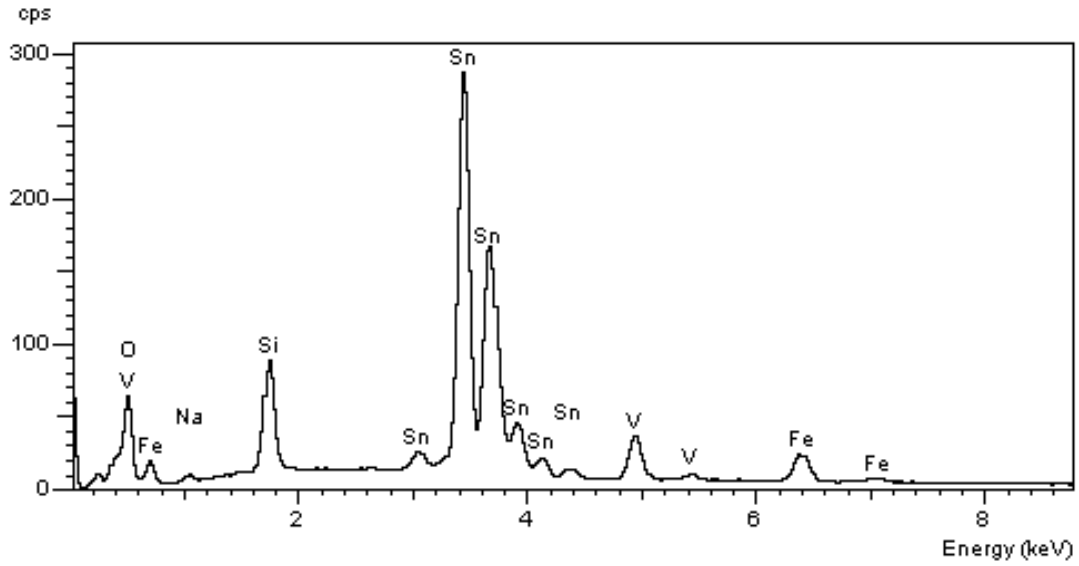

Fig. 4.8 – EDX spectra observed for electrode containing 6-layers, annealed in oxygen for 10 minutes per layer at 650 °C.

The above spectrum shows the EDX analysis of a film containing 6 layers, annealed in oxygen for 10 minutes per layer at 650 °C. This spectrum is typical of the electrodes that were made from deposition of powders that were analysed. X-rays are emitted that are characteristic of iron and vanadium in the film, signals due to silicon and tin in the substrate are also observed. This analytical technique is a useful method of determining the presence $FeVO_4$, due to the fact that other stoichiometries of iron vanadium oxide are known. However, the iron-vanadium ratios were very close to 1:1, although, the electrode containing 6 layers, annealed in oxygen was observed to have an iron:vanadium ratio of *ca.* 4:5 in the area analysed, indicating a possible abundance of vanadium at this point.

4.3 – Photo-electrochemistry

To investigate the effect of the number of layers deposited and the effect of annealing time, electrodes were made with 1, 3 or 6 layers. In addition, electrodes were made with 10 minutes or 30 minutes annealing times to investigate the effect of prolonged annealing. They were then immersed in an electrolyte of 0.5 M NaOH and photo-electrochemical measurements were conducted under simulated solar light (AM1.5) as described in section 2.6.8. The effect of the number of deposited layers on the photocurrent-voltage response is shown in fig. 4.9.

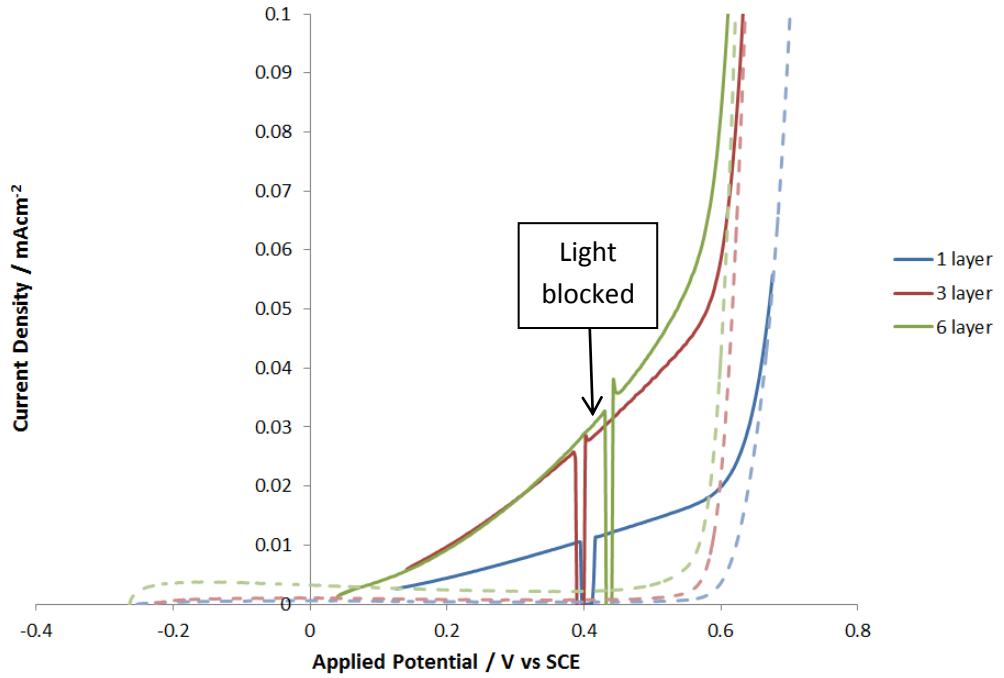

Fig. 4.9 – Photocurrent-voltage plots of electrodes annealed for 10 minutes per layer, immersed in 0.5 M NaOH. Solid lines indicate photocurrent observed under illumination from AM1.5 light. Dashed lines indicate current recorded in absence of illumination.

It can be seen in fig. 4.9, that there is a clear increase in photocurrent density with the exposure to light, highlighted by the fact that the current drops when the light is blocked. It is observed that there is a sharp increase in current at *ca.* 0.6 V, even when not exposed to light, indicative of thermodynamic water oxidation to occur at the film/electrolyte interface. When exposed to solar light however, it can be seen that there is a higher current produced at lower applied potentials (0.1-0.5 V), clearly indicating that the photo-oxidation of water in this region is light-driven. In order to compare the relative

photocurrent generation by each electrode, the highest applied potential that is confidently known not to have a contribution from an underlying dark current is 0.5 V. Here, the 1-layer electrode produces a photocurrent of *ca.* 0.0145 mAcm^{-2}, the 3-layer electrode produces 0.0382 mAcm^{-2} and the 6-layer electrode gave a photocurrent of 0.0430 mAcm^{-2}. This clearly showed an increase in produced photocurrent with increasing applied layers. Film thickness has been previously reported to affect light absorption and charge transport.[17] Finally, it appears that the onset potential is fairly consistent for all three electrodes, at *ca.* 0.1 V, indicating that the band edges are unaffected by the additional layer deposition.

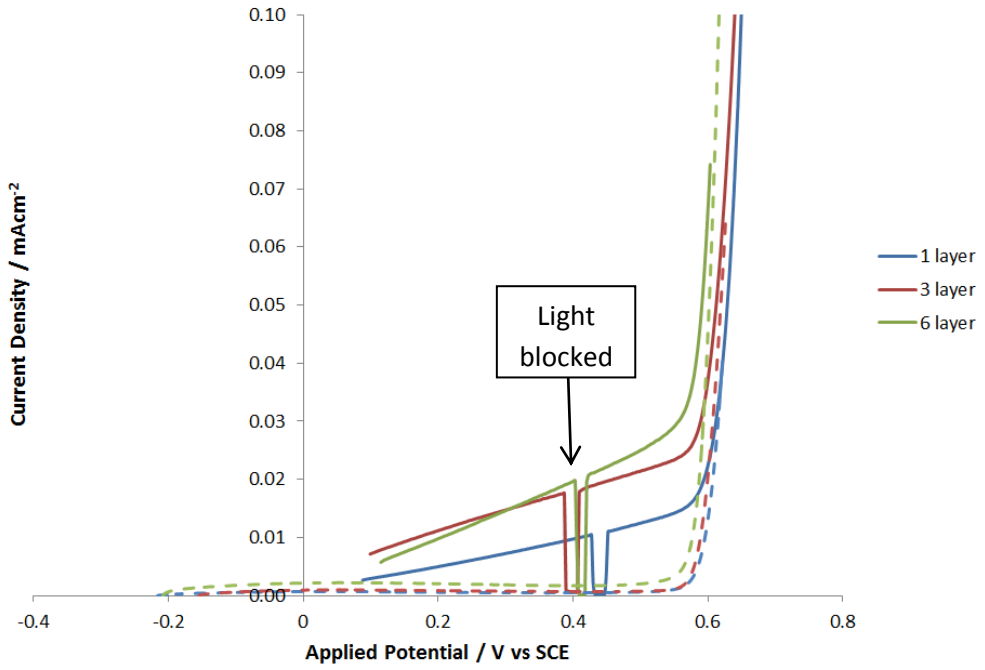

Fig. 4.10 – Photocurrent-voltage plots of electrodes annealed for 30 minutes per layer, immersed in 0.5 M NaOH. Solid lines indicate photocurrent observed under illumination from AM1.5 light. Dashed lines indicate current recorded in absence of illumination.

Figure 4.10 shows similar results as in figure 4.9. Once again, there is a clear increase in photocurrent density under illumination. The photocurrent densities were again analysed at 0.5 V. Here, the 1-layer electrode produces a photocurrent of *ca.* 0.0124 mAcm^{-2}, the 3-layer electrode produces 0.0216 mAcm^{-2} and the 6-layer electrode gave a photocurrent of 0.0249 mAcm^{-2}. This again showed an increase in produced photocurrent with increasing applied layers. It also appears that the onset potential was again consistent for

all three electrodes, at *ca.* 0.1 V, meaning, once again, an external bias of this quantity was required.

In both photocurrent-voltage plots, there is an increase in photocurrent with increasing applied layers for electrodes annealed at 10 minutes or 30 minutes. It is also apparent, that the annealing time has a great effect on the photocurrents produced. Indeed, the 3 and 6-layer electrodes annealed for 30 minutes produced *ca.* 50% of the photocurrents produced when annealed for 10 minutes. Consequently, it was concluded that the largest photocurrent density was observed for the electrode containing 6-layers, annealed for 10 minutes each. Therefore, seven electrodes were made using this method, but the effect of annealing temperature was investigated. Annealing temperatures of 250, 350, 450, 550, 600, 650 and 700 °C were used.

4.4 – Temperature dependence

Electrodes were analysed by Raman microscopy at five randomly chosen points on the surface. Little variation in Raman spectra were seen within the same electrode. The spectra shown in fig 4.11 are typical spectra for each electrode.

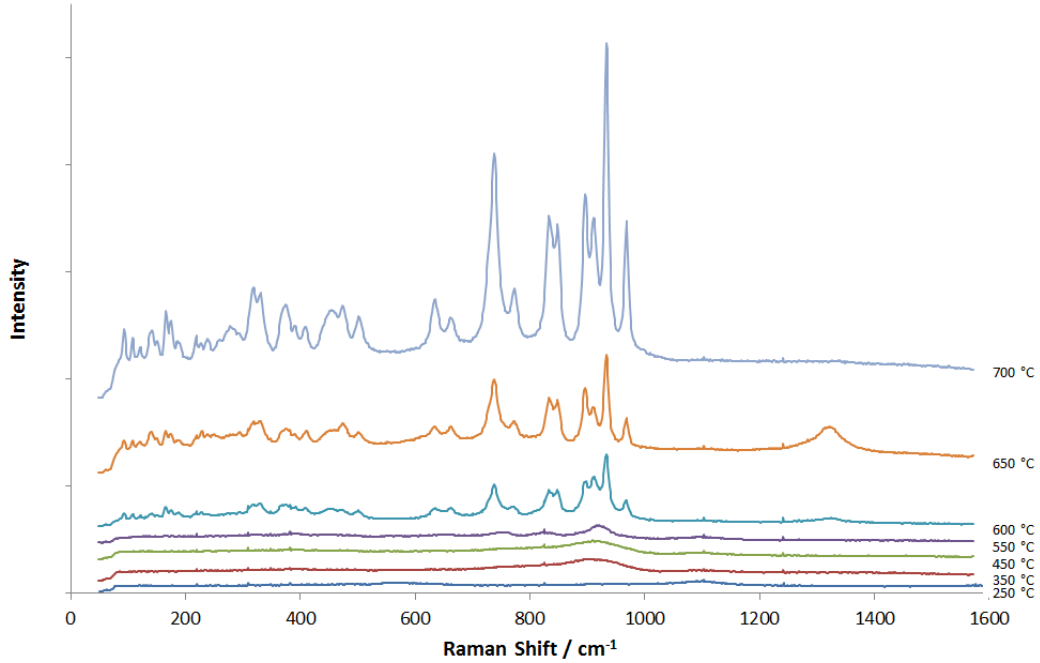

Fig. 4.11 – Raman spectra of 6-layer electrodes. The electrode was annealed for 10 minutes after each layer was deposited and annealed at the temperature given on the right of the figure.

Figure 4.11 showed clear differences in the Raman spectra of the electrodes annealed at different temperatures. Spectra obtained from films annealed at 250 and 350 °C look similar. The broad peak at 913 cm^{-1} is most likely due to terminal V-O stretching in VO_4 tetrahedra,[9] and the very weak, poorly defined bands suggest amorphous material on the electrode. The electrodes annealed at 450 and 550 °C show similar bands although there is increased resolution with increasing annealing temperature. The peak at 396 cm^{-1} is assigned to V-O-V deformation in $FeVO_4$.[9] The peak at 660 cm^{-1} is assigned to mixed bridging V-O---Fe and V---O---Fe stretching,[9] and Fe-O-Fe stretching in FeO_5 distorted trigonal bipyrimidal structures and FeO_6 octahedra in $FeVO_4$.[10] The peaks at 763 and 840 cm^{-1} correlate to bridged V-O---Fe stretches in $FeVO_4$.[9, 11] Finally, there is a peak at 930 cm^{-1}, most likely showing the presence of terminal V-O stretching in VO_4 tetrahedra.[9, 10] The Raman spectra from the iron vanadate thin films annealed at 600, 650 and 700 °C, contain identical peaks as each other, with respect to band position. Peaks at *ca.* 379, 408 and 505 cm^{-1} are assigned to V-O-V deformations in $FeVO_4$ tetrahedra.[9, 11] The peaks in the range of 600-800 cm^{-1} correspond to Fe^{3+}-O modes in FeO_6 and FeO_5.[10] Peaks at around 637, 670, 739 and 776 cm^{-1} all seem to correspond to mixed bridging V-O---Fe and V---O---Fe stretching vibrations in $FeVO_4$,[9, 10] and peaks at 844 and 849 cm^{-1} corresponds to bridged V-O---Fe stretching.[9] Peaks at around 907, 913, 935 and 969 cm^{-1} correspond to terminal V-O stretching.[9] Finally, the broad peak at 1330 cm^{-1} is a characteristic of Raman spectrum of hematite, α-Fe_2O_3.[12-14]

Figure 4.11 shows an increase in crystallinity with annealing temperature, observed by an increase in relative peak intensity and resolution, coinciding with what was observed with the iron vanadate powder in the previous chapter (fig. 3.8). Indeed the bands observed were also similar to that which was seen for the powder, and therefore the peak assignments in table 3.1 still apply. Although the peak positions are the same, the intensities on the electrode films are noticeably higher than that for the powders. This could be due to the increased amount of material analysed on the films, or the fact that a greater number of annealing cycles for the films means that the electrode was effectively annealed for longer than the powder samples, thereby increasing crystallinity.

To investigate the effect of annealing temperature, the electrodes made with 6 layers, annealed in oxygen for 10 minutes each, at specific temperatures underwent photo-electrochemical analysis. They were immersed in an electrolyte of 0.5 M NaOH and photo-electrochemical measurements were conducted under simulated solar light (AM1.5) as described in section 2.6.8. The effect of the annealing temperature on the photocurrent-voltage response is shown in fig. 4.12.

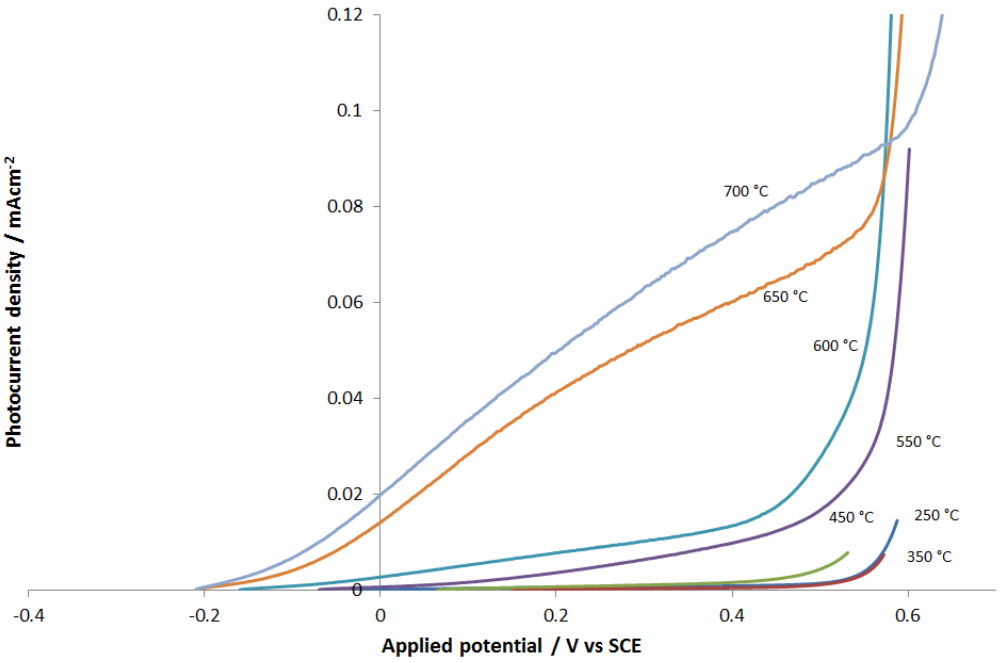

Fig. 4.12 – Photocurrent-voltage plots of electrodes annealed for 10 minutes per layer at the stated temperatures, immersed in 0.5 M NaOH. Solid lines indicate photocurrent observed under illumination from AM1.5 light.

Figure 4.12 shows the photocurrent-voltage plots of 6-layer electrode films annealed at temperatures in the range 250-700 °C, the Raman spectra of which are shown in figure 4.11. Dark currents (data not shown) were negligible until 0.6 V. Using photocurrents generated at 0.5 V as a comparison: films annealed at 250 and 350 °C produced photocurrents of 0.001 $mAcm^{-2}$, the film annealed at 450 °C produced 0.004 $mAcm^{-2}$, 550 °C produced 0.018 $mAcm^{-2}$, 600 °C produced 0.028 $mAcm^{-2}$, 650 °C produced 0.069 $mAcm^{-2}$, and finally, the film annealed at 700 °C produced a photocurrent of 0.086 $mAcm^{-2}$. It was observed that there is an increase in produced photocurrent with increasing annealing temperature, corresponding to increased crystallinity shown with Raman spectroscopy. This rise could be due to the increased crystallinity[18, 19] in the film,

with annealing temperature,[20] producing a more ordered structure and improving charge transport,[21] and consequently increasing the current observed.

4.5 – Film stability

In order to determine how stable the iron vanadate films are on the electrode, Raman spectra were taken before and after photo-electrochemical measurements. Raman spectroscopy was used as it allows quick comparison and allows one to observe whether the film is undergoing delamination or degradation. For example if the Raman spectra significantly decreases in intensity, the most likely cause is degradation. However, if peaks disappear completely, the most likely cause is delamination. The electrode film annealed at 600 °C was used as an example.

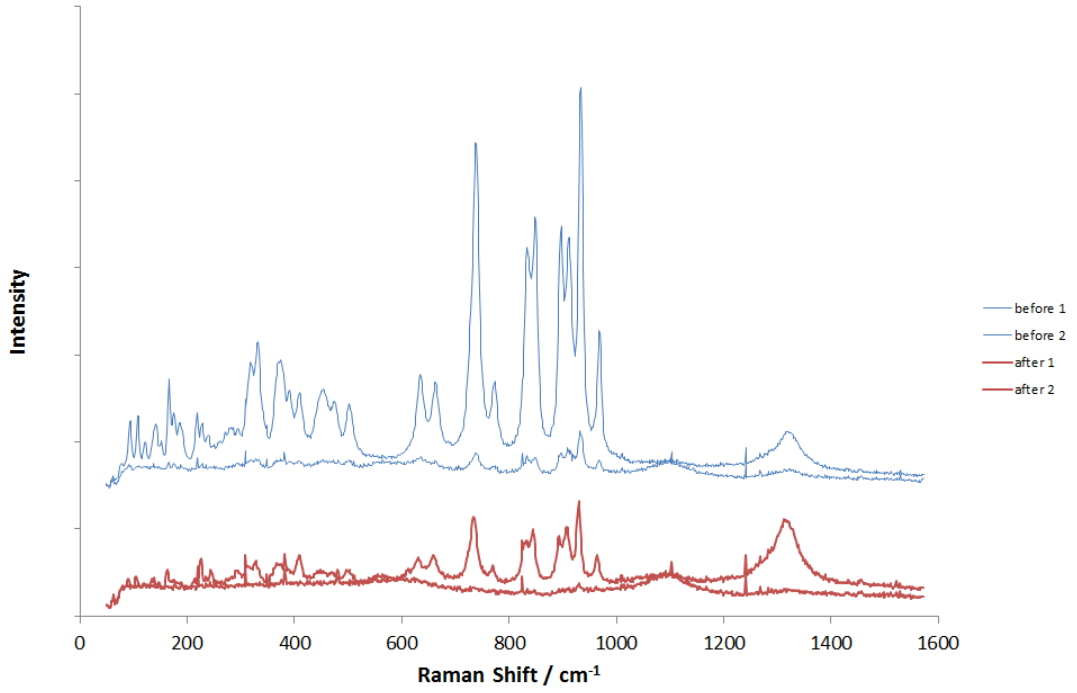

Fig. 4.13 – Most and least intense Raman spectra taken of a 6-layer electrode before (*blue*) and after (*red*) photo-electrochemical measurements. The electrode was annealed for 10 minutes after each layer was deposited and annealed at the temperature 600 °C.

It can be seen from figure 4.13, that the bands observed in the Raman spectra recorded before photo-electrochemical measurements were taken, followed band assignments as described in section 4.4 for this film annealed at 600 °C. The spectral intensities

significantly decrease after photo-electrochemical measurements. For example the most intense peak in the spectra before the measurements, at 935 cm^{-1}, is at *ca.* 4650 counts. However, the same band in the Raman spectra recorded after the measurements, although still the most intense band in the spectrum, is only 1325 counts by comparison. It appears that the intensities of the peaks corresponding to iron vanadate decrease uniformly which suggests a similar chemical composition before and after photo-electrochemical measurements although the Raman band for hematite at 1325 cm^{-1} appears to increase its intensity relative to $FeVO_4$ for one region of the surface. One inconsistency to this however, is the least intense spectrum of the film after the measurement, which contains only one of the peaks assigned to iron vanadate, at 935 cm^{-1}.

These decreases after photo-electrochemistry may be for a number of reasons, such as changes in instrumental focus, less material on the substrate and poorer crystallinity[22, 23] (*i.e.* degradation). Care was taken to ensure that the focussing was performed in the same way for each measurement, it is most likely due to the degradation of the iron vanadate, due to the fact the iron oxide (shown by the peak at 1330 cm^{-1}) did not appear to change. This therefore means that the instability could be due to delamination of the film or degradation of the iron vanadate. The decrease in peak intensity occurred regardless of annealing temperature, but was more noticeable as annealing temperature increased due to the increased intensity of the films before the measurements.

4.6 – Conclusions

Iron vanadate powder was applied to substrates prior to an annealing step. After annealing at specific temperatures, and an investigation of the effect of numbers of layers, the iron vanadate films where shown to be photo-active producing photocurrents of up to 0.09 $mAcm^{-2}$ at 0.5 V vs. SCE. It was also demonstrated that this photo-activity increased with annealing temperature and resultant crystallinity. It was also determined that the most crystalline films appeared porous and produced an indirect band gap of 2.0-2.1 eV. Finally, it was determined that the films were not stable during the photo-electrochemical measurements, as indicated by the comparison of Raman spectra before and after photo-electrochemical measurements.

4.7 - References

1. P. Poizot, E. Baudrin, S. Laruelle, L. Dupont, M. Touboul and J. M. Tarascon, *Solid State Ionics*, 2000, **138**, 31-40.

2. F. Orsini, E. Baudrin, S. Denis, L. Dupont, M. Touboul, D. Guyomard, Y. Piffard and J. M. Tarascon, *Solid State Ionics*, 1998, **107**, 123-133.

3. C. D. Morton, I. J. Slipper, M. J. K. Thomas and B. D. Alexander, *Journal of Photochemistry and Photobiology A: Chemistry*, 2010, **216**, 209-214.

4. R. Solarska, I. Rutkowska, R. Morand and J. Augustynski, *Electrochimica Acta*, 2006, **51**, 2230-2236.

5. M. T. Li, L. A. Zhao and L. J. Guo, *International Journal of Hydrogen Energy*, 2010, **35**, 7127-7133.

6. C. S. Enache, D. Lloyd, M. R. Damen, J. Schoonman and R. V. de Krol, *Journal of Physical Chemistry C*, 2009, **113**, 19351-19360.

7. B. D. Alexander, P. J. Kulesza, L. Rutkowska, R. Solarska and J. Augustynski, *Journal of Materials Chemistry*, 2008, **18**, 2298-2303.

8. X. Chen and S. S. Mao, *Chemical Reviews*, 2007, **107**, 2891-2959.

9. A. S. Vuk, B. Orel, G. Drazic, F. Decker and P. Colomban, *Journal of Sol-Gel Science and Technology*, 2002, **23**, 165-181.

10. S. Bencic, B. Orel, A. Surca and U. L. Stangar, *Solar Energy*, 2000, **68**, 499-515.

11. G. S. Li, D. Q. Zhang and J. C. Yu, *Chemistry of Materials*, 2008, **20**, 3983-3992.

12. D. L. A. de Faria, S. V. Silva and M. T. de Oliveira, *Journal of Raman Spectroscopy*, 1997, **28**, 873-878.

13. D. L. A. de Faria and F. N. Lopes, *Vibrational Spectroscopy*, 2007, **45**, 117-121.

14. V. C. Farmer, *The Infrared Spectra of Minerals*, Mineralogical Society, Middlesex, UK, 1974.

15. W. Yao, H. Iwai and J. Ye, *Dalton Transactions*, 2008, 1426-1430.

16. M. Kurzawa and E. Tomaszewicz, *Spectrochimica Acta Part a-Molecular and Biomolecular Spectroscopy*, 1999, **55**, 2889-2892.

17. K. Sivula, R. Zboril, F. Le Formal, R. Robert, A. Weidenkaff, J. Tucek, J. Frydrych and M. Gratzel, *Journal of the American Chemical Society*, 2010, **132**, 7436-7444.

18. K. Sivula, F. Le Formal and M. Graetzel, *Chemsuschem*, 2011, **4**, 432-449.
19. *On Solar Hydrogen & Nanotechnology*, John Wiley & Sons, Chichester, UK, 2009.

20. A. Mills and S. LeHunte, *Journal of Photochemistry and Photobiology a-Chemistry*, 1997, **108**, 1-35.

21. H. S. Nalwa, *Handbook of Advanced Electronic and Photonic Materials and Devices: Conducting polymers*, Elsevier, Cambridge, UK, 2001.

22. R. J. Lehnert, P. J. Hendra and N. Everall, *Polymer*, 1995, **36**, 2473-2476.

23. M. V. PellowJarman, P. J. Hendra and R. J. Lehnert, *Vibrational Spectroscopy*, 1996, **12**, 257-261.

5 – ELECTRODES PREPARED FROM SOL-GEL SYNTHESIS

5.1 – Optimisation of electrode synthesis

Electrodes were made by drop coating a sol made using iron nitrate and vanadyl acetylacetonate solutions onto the electrode, as discussed in section 2.5. After each application, the electrode was spun at 1000 rpm before being placed into an oven in oxygen at 650 °C for 10 minutes. This process was repeated for each layer applied. The number of layers deposited on each electrode was investigated, from one to six, as was the effect of gelling time, from 0 to 10 minutes.

5.1.1 – Raman analysis

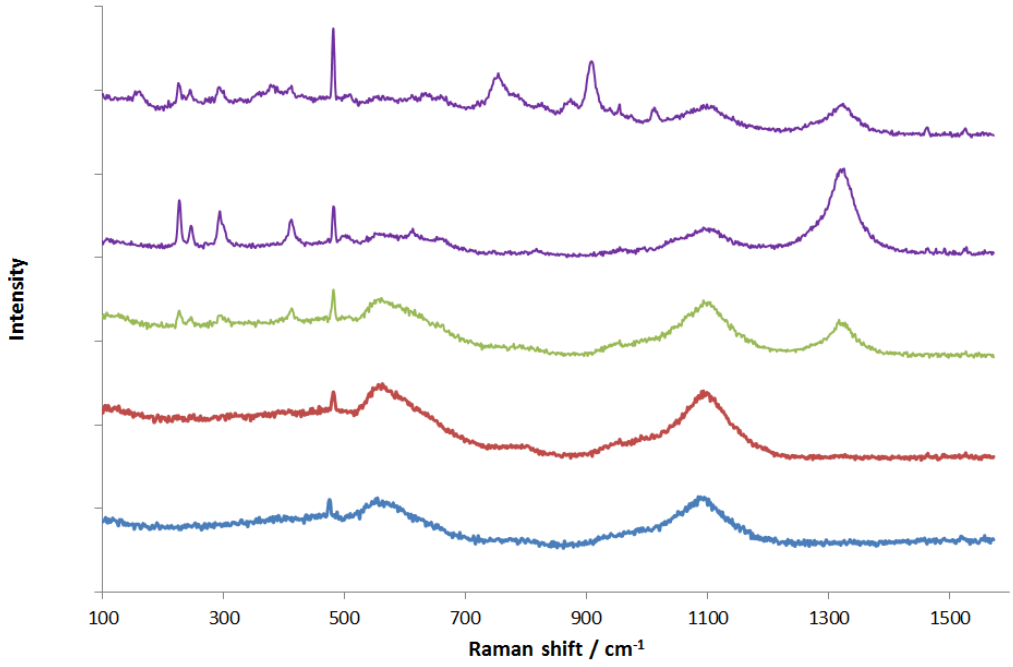

Fig. 5.1 – Representative Raman spectra of iron vanadate films containing one (red), three (green) and six layers (purple). The films were annealed for 10 minutes at 650 °C in oxygen per layer after spin coating. Also shown is the Raman spectrum of a blank F-doped SnO_2 substrate for comparison (blue).

The Raman spectra for the films containing 1 and 3 layered films in figure 5.1 are visually similar to the spectrum of the blank glass substrate. Numerous areas of each electrode film were analysed, and all but the film containing 6 layers showed uniformity, shown by closely similar Raman spectra recorded at different points on the film surface.

The Raman spectra presented in this chapter are representative of all of the points analysed on the film surface. In rare cases that the film is not uniform, more than one representative spectra will be shown in order to demonstrate the differences observed. For the 6-layer electrode, two representative spectra are shown, to illustrate the characteristic spectra that were observed in the film.

The Raman spectra of the electrode containing three layers, prepared by direct addition of the sol followed by immediate spin coating, appear to show the fluorine-doped tin oxide (FTO) glass peaks, but also begin to show peaks of other material. Namely, these are at 1325 cm^{-1}, corresponding to hematite,[1] and a band at around 950 cm^{-1} corresponding to terminal V-O stretching and VO_4^{3-} tetrahedra.[2-4] In the spectra of the film containing six layers, more bands begin to emerge, most likely due to the presence of more material on the electrode surface. The film containing three layers displayed bands at similar Raman shifts to those observed in the spectra of the 6-layer film. The peak observed at 388 cm^{-1} corresponds to Fe-O stretching in $FeVO_4$.[3] The peak at 640 cm^{-1} corresponds to mixed bridging V-O---Fe and V---O---Fe stretching,[3] and Fe-O-Fe stretching vibrations in FeO_5 distorted trigonal bipyrimidal structures and FeO_6 octahedra in $FeVO_4$.[2] A peaks at 758 and 830 cm^{-1} indicate $FeVO_4$,[3, 5] again in bridged V-O---Fe stretches. Lastly, there is a peak at 910 cm^{-1} which shows the presence of terminal V-O stretching in VO_4.[2, 3]

5.1.2 – Diffuse Reflectance UV/Visible Analysis

Diffuse reflectance UV/Vis spectroscopy was used to determine the light absorbance properties of the films annealed at 650 °C for 10 minutes in oxygen and is shown in figure 5.2.

It can be seen in figure 5.2 that the absorbance increases with increasing number of layers, due to more material being present. When these were converted to Tauc plots, it was seen that a Tauc plot for an indirect band gap best fit the data (fig. 5.3)

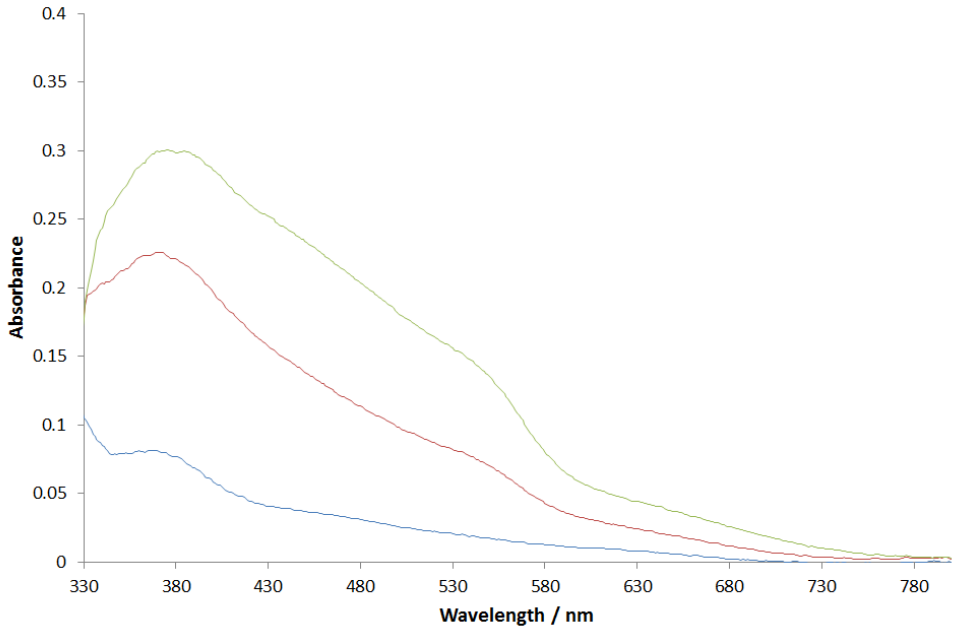

Fig. 5.2 – Diffuse reflectance UV/Vis spectra of three iron vanadate electrodes made by direct application of the sol followed by immediate spin coating. (one layer – blue, three layer – red, six layer – green).

.

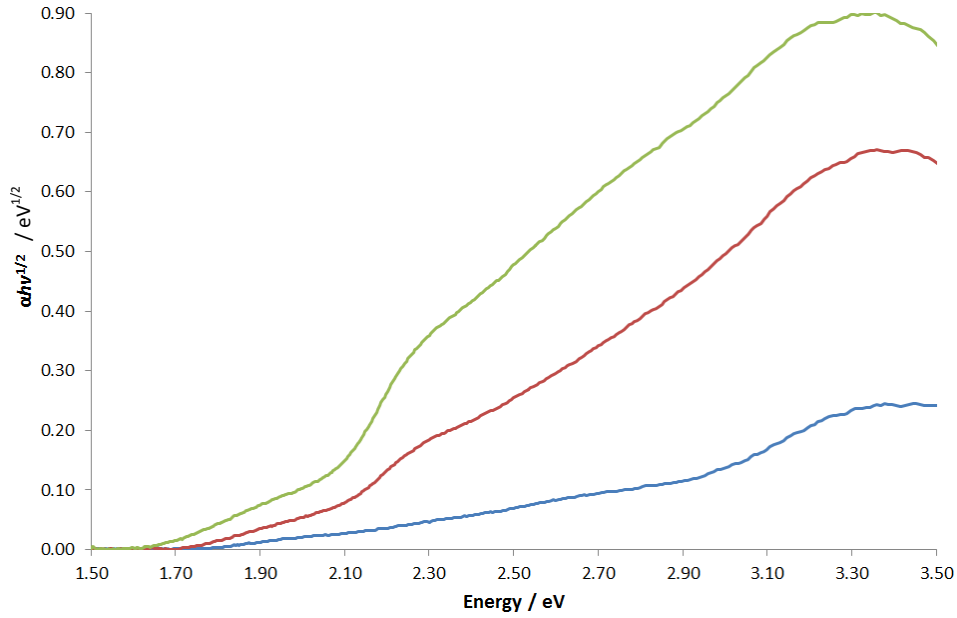

Fig. 5.3 – Tauc plots for the electrode films spin-coated directly after deposition, (six layers – green, three layers – red, one layer – blue). Films were annealed at 650 °C in oxygen, for 10 minutes per layer.

Band gaps of 2.00 eV were observed for the films containing six and three layers, and just below that for the one layered film, at *ca.* 1.95 eV. The latter, however, was difficult to measure as the UV/Vis spectra were very weak.

5.1.3 – Photo-electrochemical measurements

These three electrodes were analysed by photo-electrochemistry to see if they were photo-active and to investigate their stability in comparison to the films detailed in the previous chapter. The conditions were the same as with the previous electrodes, AM1.5 light was used to irradiate the samples in an electrolyte of 0.5 M NaOH, in the presence of an SCE reference electrode. Shown in figure 5.4, are the *j/v* plots for the electrodes synthesised with direct spin coating after deposition.

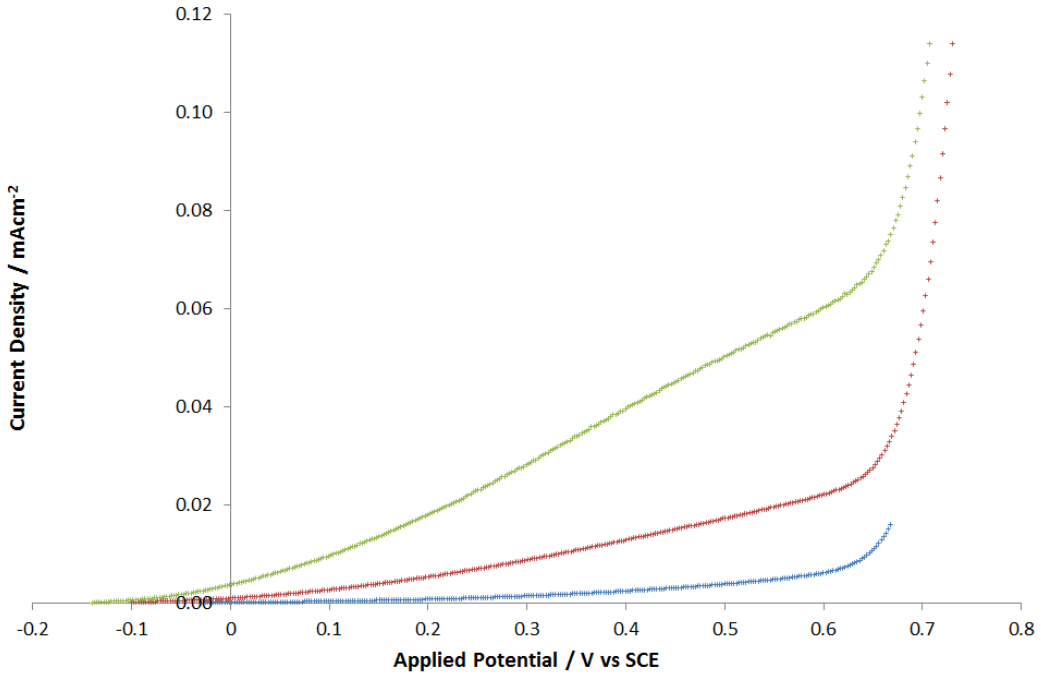

Fig. 5.4 – j/v plots of the electrode films spin-coated directly after deposition, exposed to AM1.5 light, in 0.5 M NaOH electrolyte, with a 0.01 Vs^{-1} scan rate. (six layers – green, three layers – red, one layer – blue.)

It was observed there was a clear increase in photo-activity with an increasing number of layers, the highest being with the film containing six layers, producing a current density of *ca.* 0.06 $mAcm^{-2}$ at 0.55 V. This increase could be for two reasons. Firstly, there is more material present, and therefore more electron-hole pairs may be generated under illumination due to greater absorbance, as shown in fig. 5.2. This may lead to a greater charge transfer between the electrode and the electrolyte, and consequently a higher observed current. Secondly, the material in the initially deposited layers has been heated in the oven for longer, due to the need to anneal each of the subsequent layers, and could therefore mean that parts of the films are more crystalline (possibly indicated by

increasing intensity of Raman spectra in fig. 5.1) at the FTO-film interface, improving charge transport, and limiting recombination.

5.1.4 – Gelling

Due to the fact that there did not appear to be sufficient material to be detected by Raman spectroscopy, the sol was gelled on the electrodes first, for 5 and 10 minutes before spinning them. Gelling involved applying the film to the electrode and allowing it to sit for 5 or 10 minutes. The purpose of this was to allow some of the solvent to evaporate, and make the film more viscous, which would result in less material being expelled from the electrode upon spinning, and may also allow some sol to adhere to the substrate during the gelling process.

5.1.5 – Raman analysis of films prepared following gelling of sol

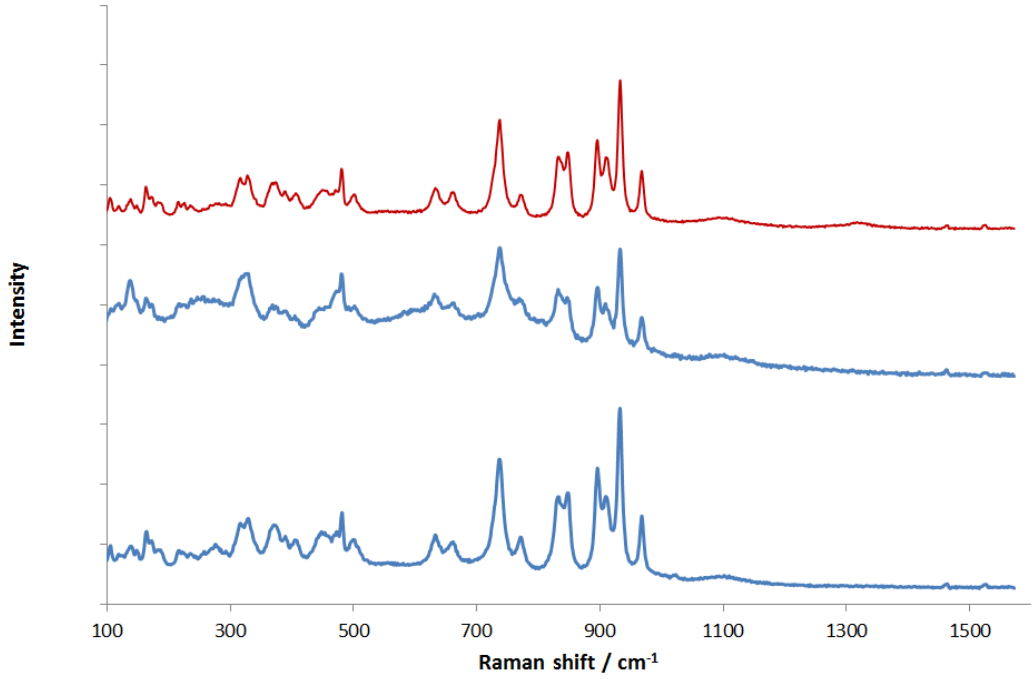

Fig. 5.5 – Representative Raman spectra of 3-layer iron vanadate films annealed at for 10 minutes per layer at 650 °C in oxygen, each layer was gelled for 10 minutes (red) and 5 minutes (blue).

The film made from a sol that was gelled for 10 minutes per layer gave Raman spectra that did not vary with location on the film surface and was thus more uniform, hence only one representative Raman spectrum is presented in fig. 5.5. In contrast, the electrode film gelled for only 5 minutes per layer appeared slightly less uniform. This is shown by a

slight change in the in the band intensities between the two points shown. This could be due to more material being expelled from the electrode upon spinning, as a result of the less viscous nature of the sol. However these differences are very slight, indicating a very small range of variation. Looking at both films, it is clearly apparent that the spectra are well defined and that the bands are sharp and intense, which indicates well crystalline films as observed in previous chapters, as well as a peak at 1100 cm^{-1} corresponding to the FTO glass. Peaks observed at 230 and 290 cm^{-1} are characteristic of hematite (α-Fe_2O_3).[1, 6] However, peaks at around 375, 405 and 503 cm^{-1} are representative of V-O-V deformations in VO_4 tetrahedra in $FeVO_4$.[3, 5] Bands within the range of 800-600 cm^{-1} correspond to Fe^{3+}-O stretching modes in FeO_6 and FeO_5.[2] Bands at 637, 664, 737 and 776 cm^{-1} all correspond to mixed bridging V-O---Fe and V---O---Fe stretching vibrations in $FeVO_4$,[2, 3] while the peaks at 838 and 848 cm^{-1} also correspond to bridging V-O---Fe stretching.[3] The bands present at *ca.* 897, 913, 932 and 967 cm^{-1}, correspond to terminal V-O stretching vibrations.[3] Finally, the broad peak at 1327 cm^{-1} indicates a two-magnon scattering band characteristic in hematite, α-Fe_2O_3.[1, 6-8]

5.1.6 – Diffuse reflectance UV/Vis analysis of films prepared following gelling of sol

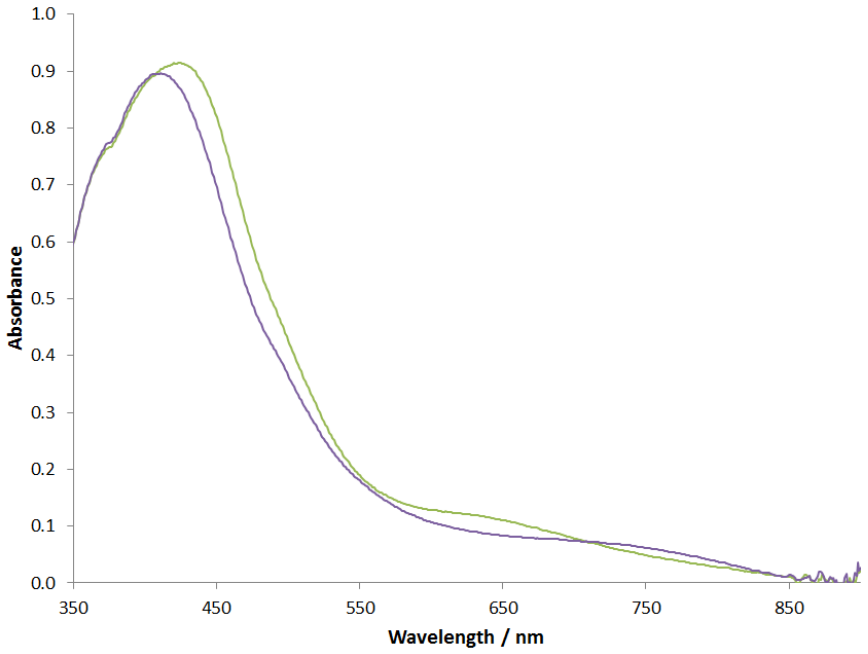

Fig. 5.6 – Diffuse reflectance UV/Vis spectra of electrodes containing 3 layers, each gelled for 10 (purple)and 5 minutes (green), and annealed in oxygen at 650 °C for 10 minutes per layer.

Figure 5.6 shows the diffuse reflectance UV/Vis spectra for the films which have been gelled before spin coating. It can be seen that there is not much difference between them apart from an increase in absorbance at *ca.* 630 nm, for the film that has been gelled for 5 minutes, which could possibly indicate oxygen deficiencies and V^{4+} ions as lattice defects.[9] The intensity of these spectra are higher than seen for the films spin-coated immediately after deposition, as seen in figure 5.2, indicating a thicker layer had been deposited following the gelling process, due to increased viscosity of the sol.

5.1.7 – Photo-electrochemical measurements of films prepared following gelling of sol

The electrodes gelled for different times were analysed using the photo-electrochemical setup used previously. The resulting photocurrent measurements are presented in figure 5.7.

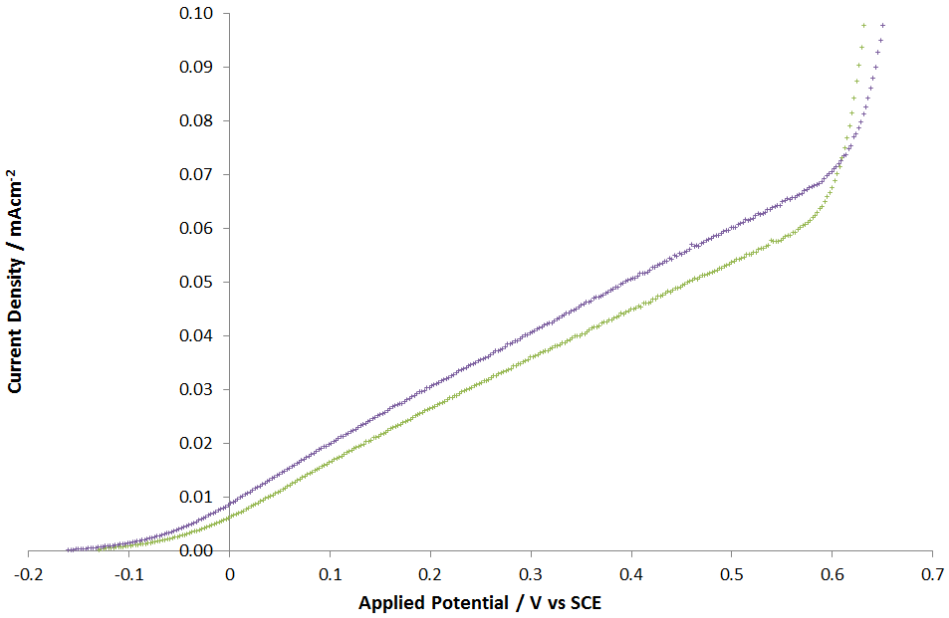

Fig. 5.7 – j/v plots of iron vanadate films containing 3 layers, each layer gelled for 10 (purple) and 5 minutes (green) before spin-coating. Electrodes were annealed for 10 minutes per layer at 650 °C in oxygen. Measurements taken when exposed to AM1.5 light in 0.5 M NaOH electrolyte, using a scan rate of 0.01 Vs^{-1}.

The *j/v* plots in figure 5.7 show that there is a slight increase in photocurrent density with gelling time. This result is most likely due to more material being retained by the electrode when spun, as a result of the sol being more viscous. This increase in film thickness therefore increases the absorbance of the film (see fig. 5.6), and may be

responsible for the increased photocurrent. However it should also be noted that an optimum thickness will be determined. It can be seen that the film containing three layers, gelled for 10 minutes per layer before annealing actually produced a slightly larger photo-current density than was observed in the electrode containing six layers without any gelling, seen in figure 5.4.

5.1.8 – Post-photo-electrochemical analysis of films prepared following gelling of sol

Raman spectroscopy was used to re-analyse the surfaces of the films after the photo-electrochemistry measurements to observe how the film composition changes during experiment. Consequently, it is able to indicate how stable the films are.

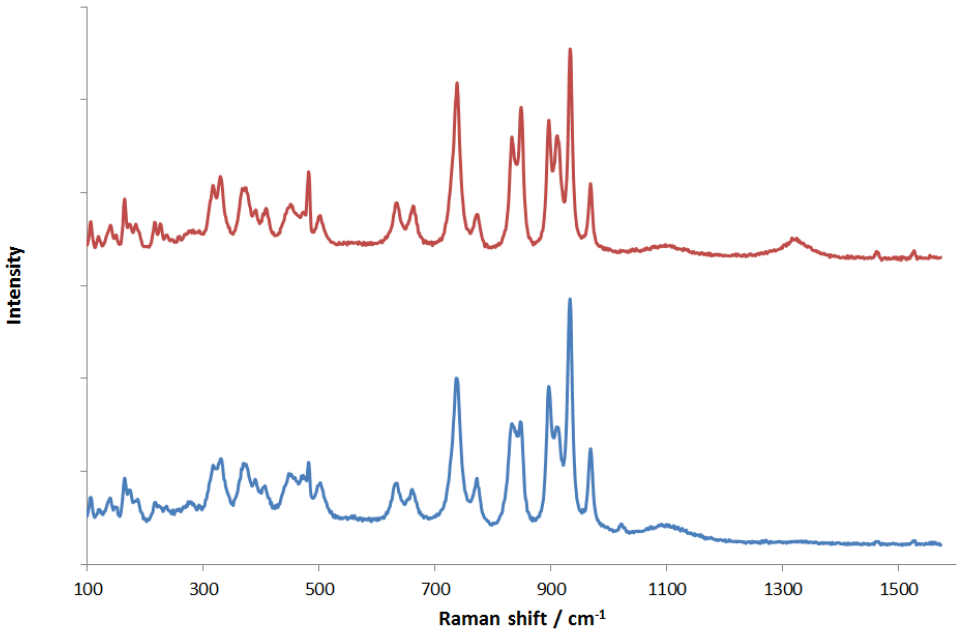

Fig. 5.8 – Representative Raman spectra of iron vanadate films gelled for 5 minutes (blue) and 10 minutes (red) and annealed at 650 °C for 10 minutes per layer in oxygen, after photo-electrochemical measurements were taken.

It can be seen when comparing the Raman spectra of electrodes before and after PEC measurements (figures 5.5 and 5.8 respectively), that there is little difference in the spectral intensity when comparing the spectra recorded before and after photo-electrochemistry measurements. This indicates a much higher stability than was observed for the electrodes in the previous chapter, where the peak intensity dropped dramatically

during photo-electrochemistry. This is possibly due to the iron vanadate being synthesised directly onto the substrate, improving adhesion.

It was therefore decided that an electrode film containing three layers allowed to stand for 10 minutes before spin-coating, was the optimum preparation method to allow comparison of properties from electrode to electrode, due to the fact that it was chemically and mechanically stable and afforded a comparatively high photo-current density.

5.2 – Reproducibility

During the course of making the electrodes reported herein, and the last chapter there is some variation in the photocurrents measured. Therefore, the source of this irreproducibility was investigated. The reproducibility of the film formation and the photo-electrochemical measurements were analysed. All electrodes within this section contained 3 layers, gelled for 10 minutes each, spin-coated, and then annealed for 10 minutes each at 600 °C in oxygen. In each reproducibility investigation herein, (5.2.1, 5.2.2 and 5.2.3) the colours of the Raman spectra and the resultant photo-electrochemistry measurements match to the same electrode.

5.2.1 – Reproducibility of electrodes

As it was thought possible that the sol used may be subject to an aging process, a series of electrodes were made from the same sol, within 8 hours of each other. The resulting electrodes were first characterised to identify any variation in composition prior to photo-electrochemical measurements. Raman spectra recorded from these electrodes is given in figure 5.9.

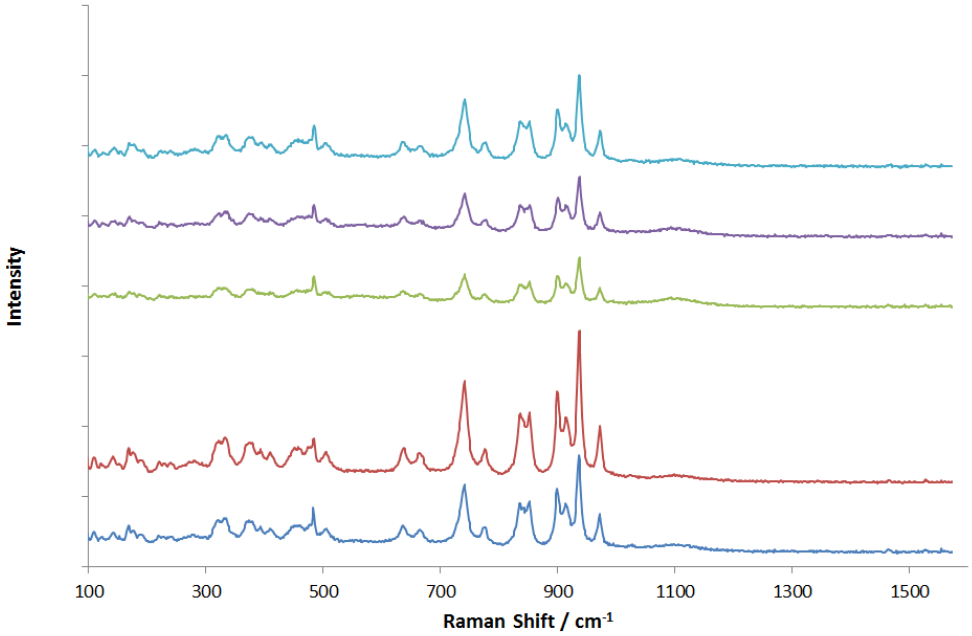

Fig. 5.9 – Raman analysis of five iron vanadate films made from the same sol. Each had three layers, gelled for 10 minutes each, and annealed for 10 minutes at 600 °C in oxygen.

It can be observed from figure 5.9 that the spectra are broadly similar throughout these electrodes, indicating little variation in composition. No hematite peaks were observed, only that of the iron vanadate and the substrate. The spectra observed are most representative of the selected points analysed on the film. There is a slight difference in intensity in the different electrodes. The observed intensities can be affected by a number of factors, such as: focusing, density of material and crystallinity of material. The effect of changing density and crystallinity was minimised by agitating the sol before deposition, depositing the same number of drops of sol for each layer, keeping the spin-coating procedure the same and keeping annealing conditions the same. Care was taken to ensure focusing was performed in the same way each time in order to minimise the effect of this factor on the results.

Any variation in photocurrent density measured from these electrodes may be linked to the variation in deposition of the films. The results of the photo-electrochemical analysis are given in figure 5.10.

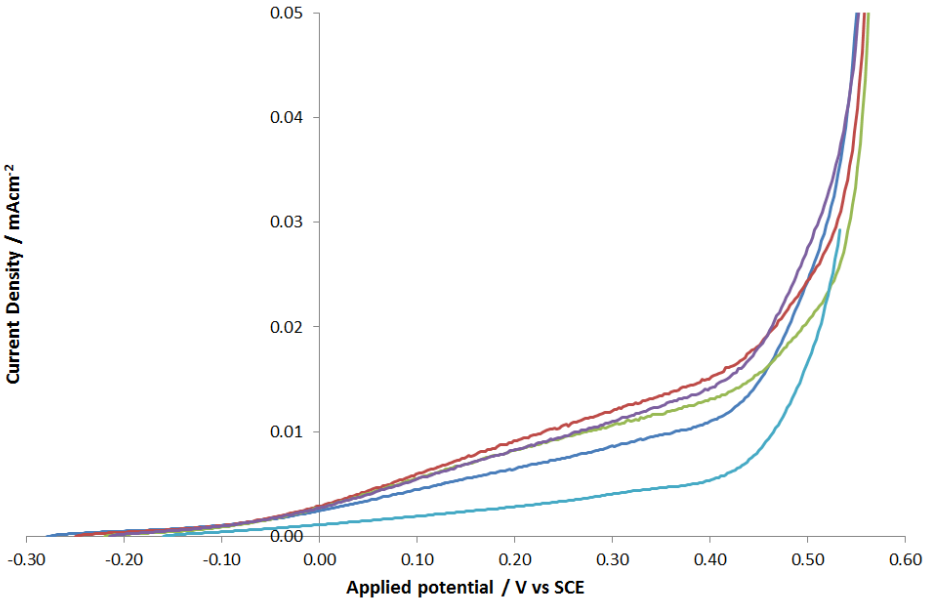

Fig. 5.10 – Photo-electrochemical measurements of five iron vanadate electrodes made using the same sol containing three layers, annealed for 10 minutes each, gelled for 10 minutes each, annealed at 600 °C. Measurements were performed in 0.5 M NaOH electrolyte, exposed to AM1.5 light, using a 0.01 Vs^{-1} scan rate. All of the electrodes were analysed in one batch. The colours match the electrodes to their Raman spectra in fig. 5.9.

It can be seen from the above figure that the iron vanadate made from the same sol give a reasonably consistent photocurrent, with the exception of one (light blue). In addition, another electrode gave a slightly lower photocurrent (dark blue) compared to the others.

5.2.2 – Reproducibility of photo-electrochemical analysis

A series of electrodes were produced from the same sol within a short period of time and analysed on different days in order to observe the reproducibility of the photo-electrochemistry measurements. Possible sources of irreproducibility investigated such as placement of electrode in relation to light source.

Three electrodes were made and first characterised to ensure compositional uniformity. The results of Raman microscopy are shown in figure 5.11.

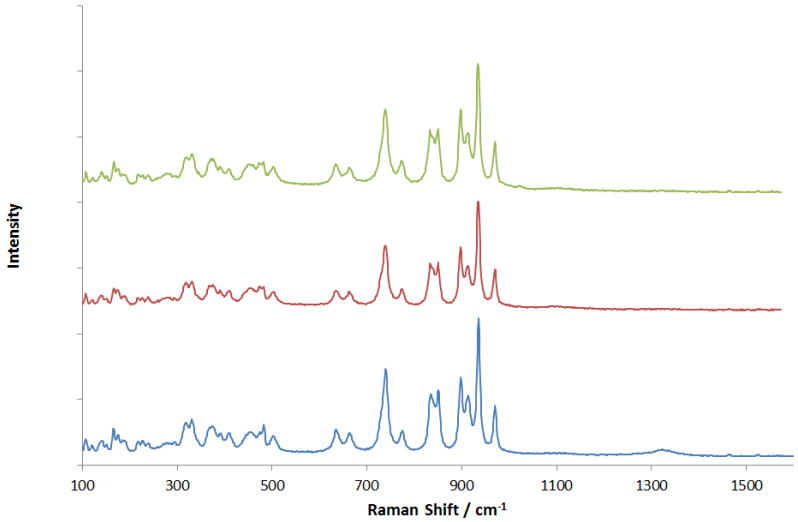

Fig. 5.11 – Raman analysis of three iron vanadate films made using the same sol. Each had three layers, gelled for 10 minutes each, and annealed for 10 minutes at 600 °C in oxygen.

The above spectra are the most representative spectra of the electrode films and little variation across electrode surface and between electrodes is found, thus giving confidence that there is reproducibility in the electrode preparation. These electrodes were then analysed using photo-electrochemical measurements, shown in figure 5.12. It can be seen that the electrode analysed first (blue), appeared to contain a trace of hematite also.

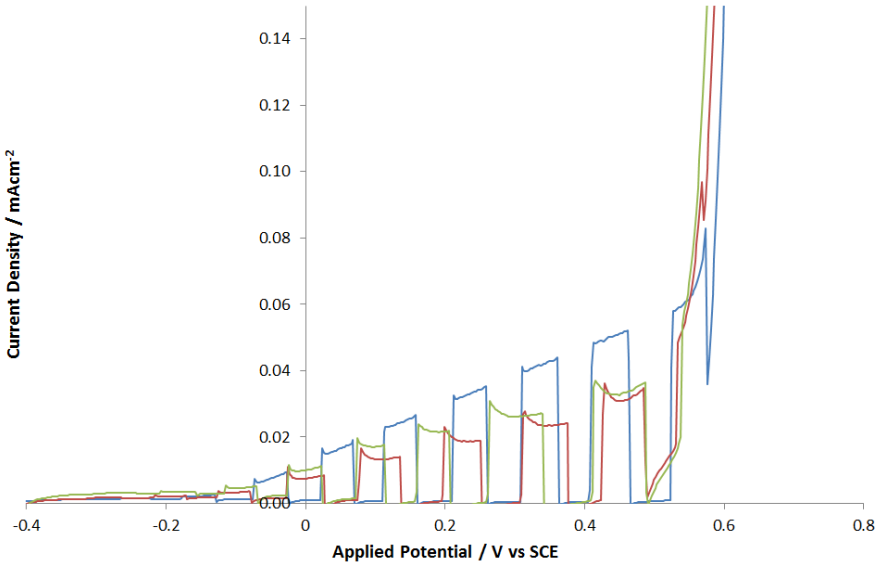

Fig. 5.12 – Photo-electrochemical measurements of three iron vanadate electrode films made using the same sol, containing three layers, gelled for 10 minutes each, and annealed for 10 minutes at 600 °C in oxygen. Photo-electrochemical measurements were recorded over the space of three days. 0.5 M NaOH was used as an electrolyte, AM1.5 light was used as a light-source, and a scan rate of 0.01 Vs^{-1} was used. The colours match the electrodes to their Raman spectra in fig. 5.11.

To clearly observe the difference between the light and dark currents during these experiments, the light source was blocked (shown by the sharp decrease in current) and un-blocked every five seconds. It was observed during these photo-electrochemical measurements, that there was a difference in the photocurrent measurements from these electrodes when analysed on the different days, notably the increase on test day 1 (blue) compared to the other two. At 0.45 V vs. SCE of applied voltage, the film analysed on day 1 (blue) produced a photocurrent of 0.052 $mAcm^{-2}$, noticeably higher than the other two, both producing 0.033 $mAcm^{-2}$. It was also seen that the Raman spectrum of this electrode clearly showed the presence of hematite within the film. An investigation into the contribution of hematite to the observed photocurrent suggests that this will be a minor contributory factor.

5.2.3 – Reproducibility of precursor sols

As sol-gel processes can suffer from variation in sol preparation,[10] films were prepared from different sols to determine the effect this has on the measured photocurrent. Possible sources of irreproducibility may be linked to particle size and aggregation of the sol and precipitation and speciation of the solution phase ions. Films were first characterised using Raman microscopy and the results are given below in figure 5.13.

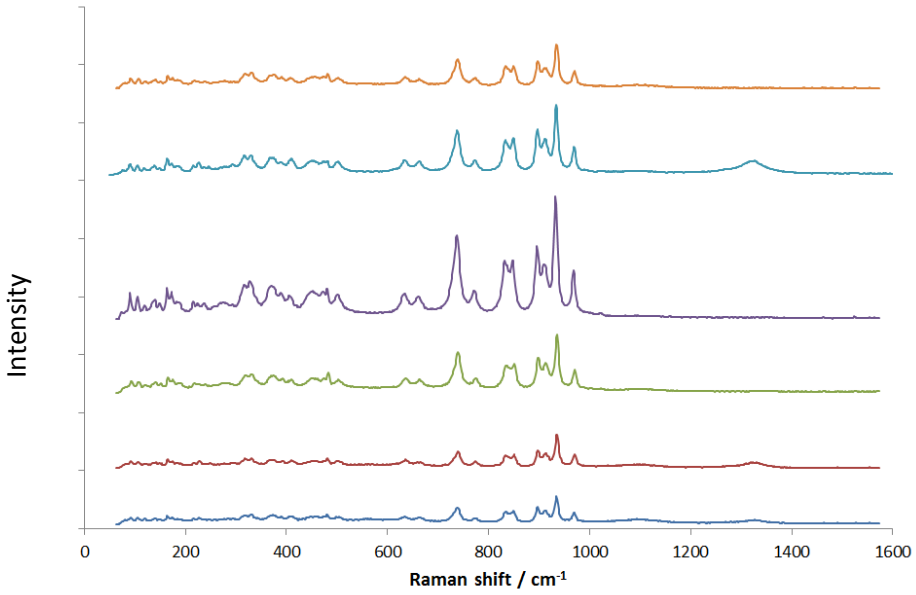

Fig. 5.13 – Raman analysis of three iron vanadate films made using the different sols. The top two spectra (orange and turquoise) are from two films made using the same sol on the same day. Each electrode consisted of three layers, gelled for 10 minutes each, and annealed for 10 minutes at 600 °C in oxygen.

Figure 5.13 shows the Raman analysis of six electrodes made using different sols with the exception of the top two spectra, orange and turquoise, which were from two films made using the same sol. These spectra are the most representative of all of the spots which were analysed on the film. It can be seen that the intensities differ from film to film. It is also apparent that hematite peaks were present in some electrodes, however, this should not significantly influence the resultant photocurrent. Having established this slight variation in the films, they were analysed by photo-electrochemistry. The results are given in figure 5.14.

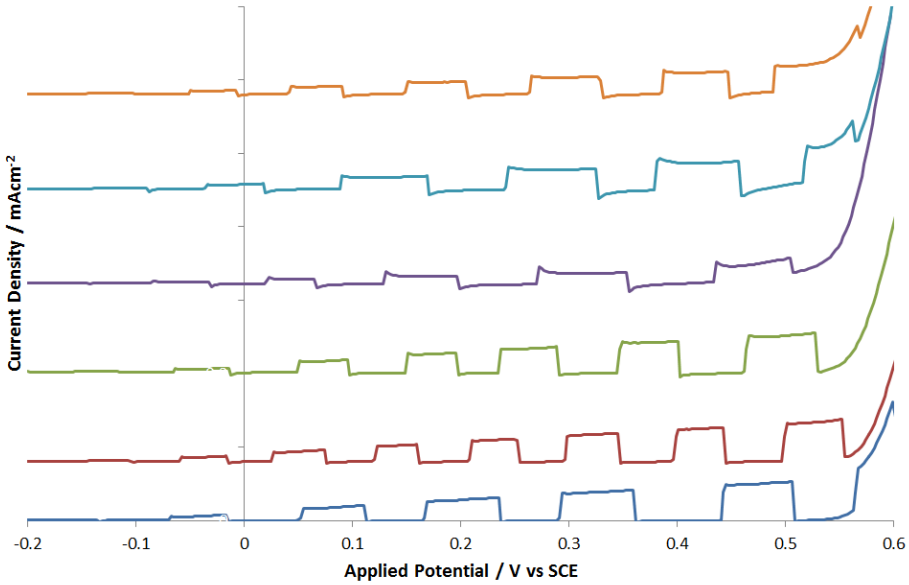

Fig. 5.14 – Photo-electrochemical measurements of iron vanadate electrode films made using different sols. Each electrode consisted of three layers, gelled for 10 minutes each, and annealed for 10 minutes at 600 °C in oxygen. Measurements were recorded in 0.5 M NaOH electrolyte, using AM1.5 light as a light-source, and a scan rate of 0.01 Vs^{-1}. *j/v* plots were stacked for clearer comparison. The colours match the electrodes to their Raman spectra in fig. 5.13.

The figure above shows the *j*/v plots from the electrode films made from different sols. For all of these films, a new sol was made on each day of electrode preparation (for the orange and turquoise plots, one sol was made to produce these two films). To clearly see the difference between the light and dark currents, the light source was blocked (shown by the sharp decrease in current) and un-blocked every five seconds. It was observed from these plots, that there is a slight difference in the photocurrents observed in these electrodes. For the electrodes made on the first three days, there appears to be little or no difference between the plots observed (dark blue, red and green). For the next three (purple, light blue, orange), made over the following two days, the photocurrents seem to be lower, by around 0.01-0.02 $mAcm^{-2}$. The differences highlight the need to consider

the age and aggregation of the precursor sol. This may influence the material deposited and also the spin coating process.

From these experiments, it seems that the main sources of error appear to originate from small fluctuations in photo-electrochemical measurements and the effect of the age of the precursor. It was therefore deemed that the best way to minimise these inefficiencies and continue to be able to make comparisons within experiments, was to make a standard 3-layer iron vanadate electrode with each investigation, to use as a comparison.

5.3 – Presence of hematite

It has been clearly observed in the Raman spectra, that hematite (α-Fe_2O_3) is present in the most crystalline films. This has previously been extensively reported as a known photocatalyst for water-splitting.[11, 12] It was therefore decided that the photocatalytic properties of this hematite should be investigated, and its contribution to the photocurrent densities observed quantified for the films produced. A three layer film was created using the same method as for making the sol, however, excluding the source of vanadium. Thus, iron nitrate was dissolved in acetic acid, which was then mixed with acetyl acetone in a manner analogous to that which is described in Section 2.5. The films were deposited, gelled for 10 minutes, spin-coated, and then annealed for 10 minutes per layer in oxygen at 650 °C.

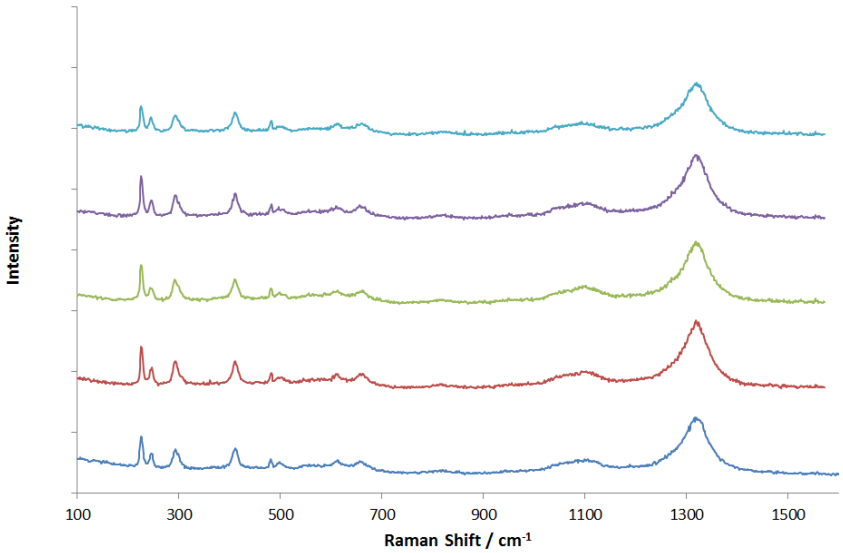

Fig. 5.15 – Raman spectra of the 3-layer iron oxide electrode annealed at 650 °C for 10 minutes per layer. Spectra were recorded at different points on the same film.

It was observed in the Raman spectra in figure 5.15 that peaks corresponding to iron oxide, at 227, 246, 293, 412, 498, 610 and 1325 cm^{-1},[6] and the tin oxide conductive layer were produced. This suggests that hematite is formed, however, the peak at 650 cm^{-1} indicates the presence of magnetite (Fe_3O_4).[6]

XRD analysis was performed on the iron oxide film in order to confirm the presence of the iron oxide and to determine as to what form it is present. The XRD diffractogram for the iron oxide film made from analogous conditions as the iron vanadate electrodes produced in fig. 5.1 and 5.8 is shown in figure 5.16.

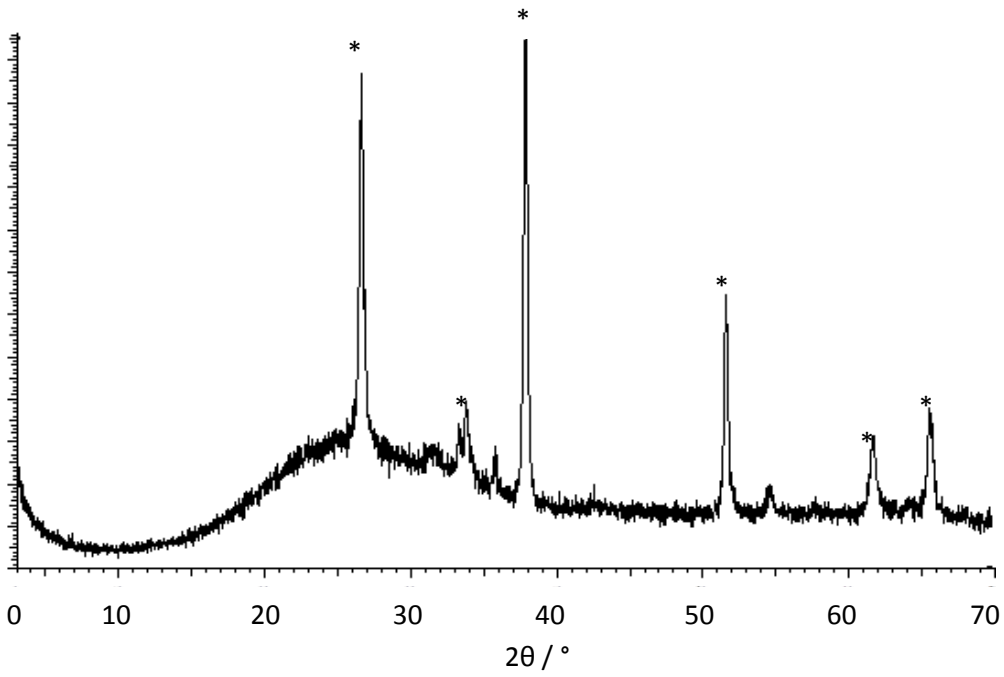

Fig. 5.16 – XRD pattern of the 3-layer iron oxide electrode annealed at 650 °C for 10 minutes per layer in oxygen. Peaks indicating FTO layer marked with *.

The XRD pattern in figure 5.16 shows evidence of peaks corresponding to the FTO conductive layer on the glass at 26.5°, 34°, 37.5°, 51.5°, 61.5° and 65.5° *2θ.* Peaks corresponding to hematite were observed at 33°, 36°, 49.5°, 54°, 57.5° and 64° *2θ.*

SEM microscopy was used in order to analyse the particle size and morphology within the iron oxide film made. This allows comparison with not only the iron vanadate films made under the same conditions, but also with other iron oxide electrodes made for photocatalysis. The SEM micrograph obtained from the surface of the iron oxide film is shown in figure 5.17.

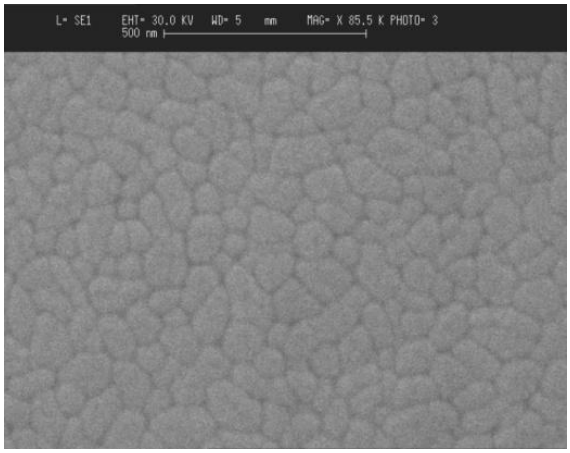

Fig. 5.17 – SEM micrograph of 3-layer iron oxide electrode annealed at 650 °C for 10 minutes per layer in oxygen.

Figure 5.17 shows an SEM micrograph of the iron oxide film made under the same conditions as the iron vanadate electrodes, detailed in fig. 5.5. It was observed that the particle size ranged between 50 and 80 nm in diameter. These particle sizes have been reported previously for iron oxide in literature at these annealing temperatures,[13] however the particles are more densely packed in this case than for deposition methods such as using colloids[13] or CVD,[12] meaning a lower porosity and surface area in films produced by the deposition from the acetylacetonate sol.

The iron oxide film, made using analogous conditions to the iron vanadate films reported in this chapter, was analysed using diffuse reflectance UV/Vis spectroscopy. Using UV/Vis spectroscopy allowed the derivation of the band gap properties using Tauc plots, to be compared to the iron vanadate films also reported in this chapter, and other iron oxide materials reported in literature. The UV/Vis spectrum recorded from the iron oxide film is presented in figure 5.18.

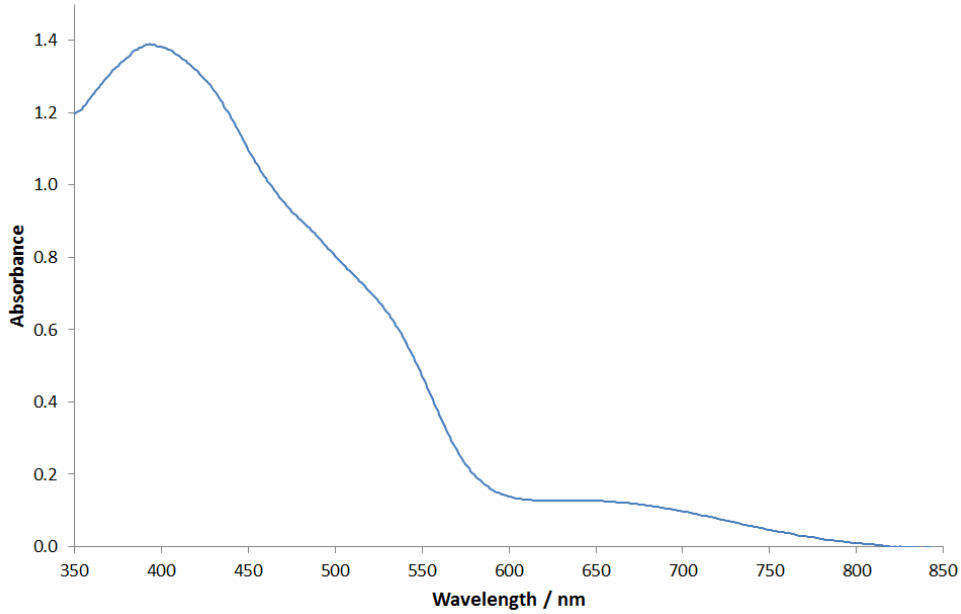

Fig. 5.18 – UV/Vis spectrum of 3-layer iron oxide electrode annealed at 650 °C for 10 minutes per layer in oxygen.

The diffuse reflectance data above was then converted into a Tauc plot to estimate the band gap. The Tauc plot for the iron oxide film again shows evidence of having an indirect band gap of around 2.1 eV, which coincides with what is reported in literature.[12, 14, 15]

Photo-electrochemical measurements were taken using the 3-layer iron oxide film, in order to quantify its contribution to the photocurrents produced by the 3-layer iron vanadate film made under analogous conditions, shown to contain traces of the iron oxide. The iron oxide *j/v* plots, both under illumination and in the absence of light, are presented in figure 5.19, and are also compared to a *j*/v plot of a 3-layer iron vanadate film made under like conditions.

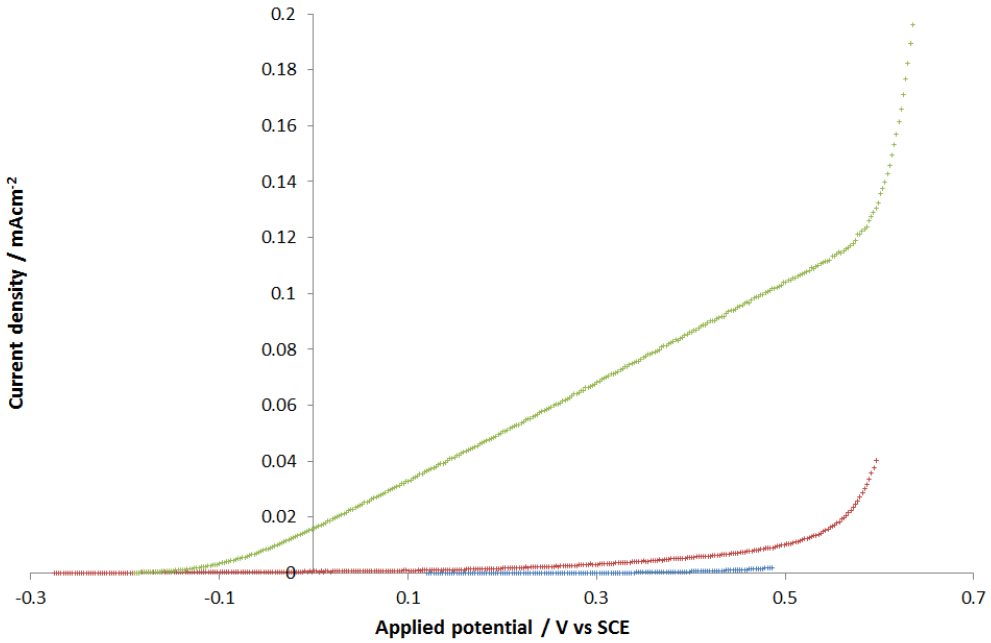

Fig. 5.19 – Photo-electrochemical measurement of 3-layer iron oxide electrode annealed at 650 °C for 10 minutes per layer in oxygen. Current shown in the absence of illumination (blue) and when exposed to AM1.5 light (red). Also shown is the PEC measurement taken from a 3-layer iron vanadate electrode, annealed at 650 °C for 10 minutes per layer in oxygen under illumination (green). All measurements were made in 0.5 M NaOH electrolyte, using a scan rate of 0.01 Vs^{-1}.

Figure 5.19 shows that while the iron oxide electrode prepared from a method analogous to the iron vanadate electrodes is photo-responsive, the photocurrent density is negligible when compared to that produced by the iron vanadate electrode annealed at the same temperature. For example, if 0.5 V vs. SCE is taken as a reference, 0.1 $mAcm^{-2}$ was produced by the iron vanadate electrode, 10 times that of the iron oxide electrode, at 0.01 $mAcm^{-2}$. It should be noted, however, that the photocurrent produced for this iron oxide film, is much smaller than many reported for iron oxide films.[12-14, 16]

5.4 – Temperature dependence

Electrode films were made by deposition of a sol and gelled for 10 minutes before each layer was spin coated, then annealed for 10 minutes each, in an oxygen atmosphere at a specific temperature. The results of the analysis by Raman microscopy are given in fig. 5.20.

5.4.1 – Raman spectroscopy

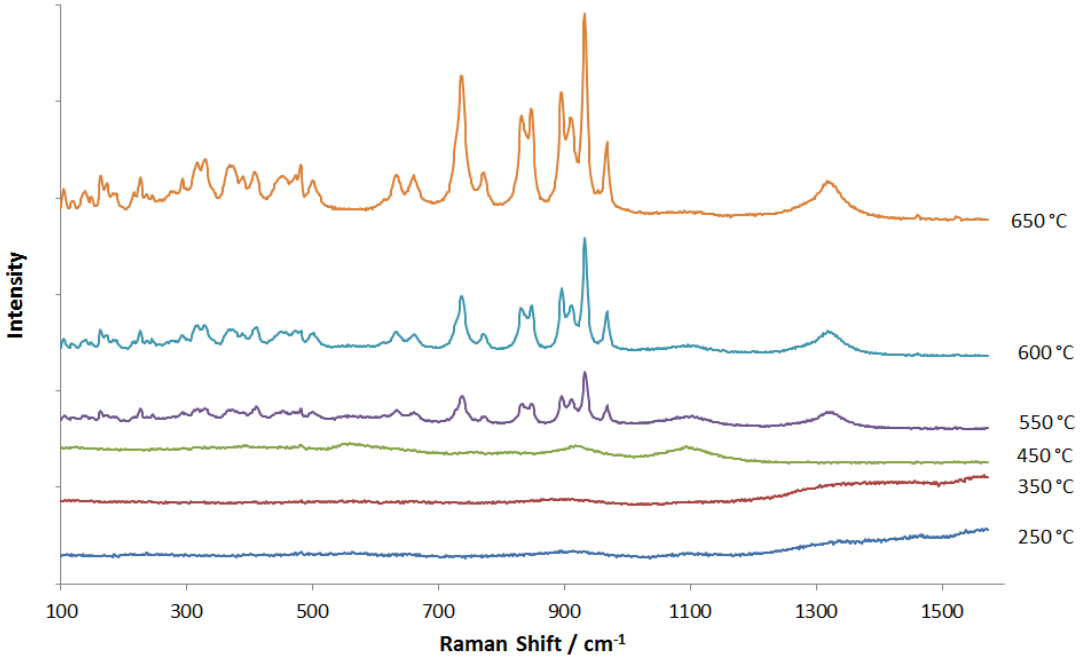

Fig. 5.20 – Raman spectra of 3 layer iron vanadate electrodes annealed at the stated temperatures for 10 minutes per layer in oxygen.

It was observed from the Raman spectra obtained (figure 5.20), that there is a clear increase in crystallinity with annealing temperature. When annealed at temperatures below 350 °C, the spectra suggested the presence of an amorphous film containing a broad peak at 916 cm^{-1} correlating to terminal V-O stretching vibrations in VO_4 tetrahedra.[3] The peak at 1100 cm^{-1} was the same as that observed for the FTO. Finally, the broad peaks observed at 1200-1600 cm^{-1} is a clear indication of the presence of carbon,[17] most likely from the acidic acetyl acetone precursor complex. The electrode annealed at 450 °C has more apparent peaks. The band at 395 cm^{-1} corresponds to Fe-O stretching in $FeVO_4$.[3] The band at 645 cm^{-1} corresponds to mixed bridging V-O---Fe and V---O---Fe stretching[3] and Fe-O-Fe stretching vibrations in FeO_5 distorted trigonal bipyrimidal structures and FeO_6 octahedra in $FeVO_4$.[2] Peaks at around 770 and 830 cm^{-1} indicate $FeVO_4$,[3, 5] once again in bridged V-O---Fe stretches. There is a peak at 920 cm^{-1} showing the presence of terminal V-O stretching in VO_4 tetrahedra.[2, 3] The peak at 1100 cm^{-1} again arises from the FTO. Lastly, a peak at 1322 cm^{-1} was observed on some areas of the electrode, indicating the presence of iron oxide (α-Fe_2O_3).[1, 6] The last three Raman spectra, annealed at 550, 600 and 650 °C, display similar profiles. There are many clearly defined, sharp peaks visible in these spectra. From the samples annealed at

550, 600 and 650 °C, some of the bands below 330 cm^{-1}, at 230 and 290 cm^{-1} are characteristic of hematite (α-Fe_2O_3).[1, 6] Peaks at around 375, 405 and 503 cm^{-1} correspond to V-O-V deformations in $FeVO_4$ tetrahedra.[3, 5] The bands in the region of 600-800 cm^{-1} correspond to Fe^{3+}-O stretching modes in FeO_6 and FeO_5.[2] Bands at around 637, 664, 737 and 776 cm^{-1} all correspond to mixed bridging V-O---Fe and V---O---Fe stretching vibrations in $FeVO_4$,[2, 3] while the peaks at 838 and 848 cm^{-1} also correspond to bridging V-O---Fe stretching.[3] Peaks at around 897, 913, 932 and 967 cm^{-1} correspond to terminal V-O stretching vibrations.[3] Finally, the broad peak at 1327 cm^{-1} is a noticeable characteristic of two-magnon scattering in hematite, α-Fe_2O_3.[1, 6-8]

5.4.2 – SEM

The SEM micrographs of the 3-layer iron vanadate electrodes annealed at temperatures of between 250-650 °C are shown in figure 5.21.

As can be seen in figure 5.21, when the annealing temperature was increased, so too was the particle size. At lower temperatures *e.g.* 250 °C, the particle size was around 50-80 nm in diameter, whereas at higher temperatures, *e.g.* 650 °C, the particle size was increased up to 100-120 nm in diameter, evidence of sintering. Indeed, there was a clear change in particle shape that occurred at temperatures that also produced a sudden increase in crystallinity. The uniformity of particle size and shape was fairly consistent throughout. The porosity seems to increase slightly with increased annealing temperature.

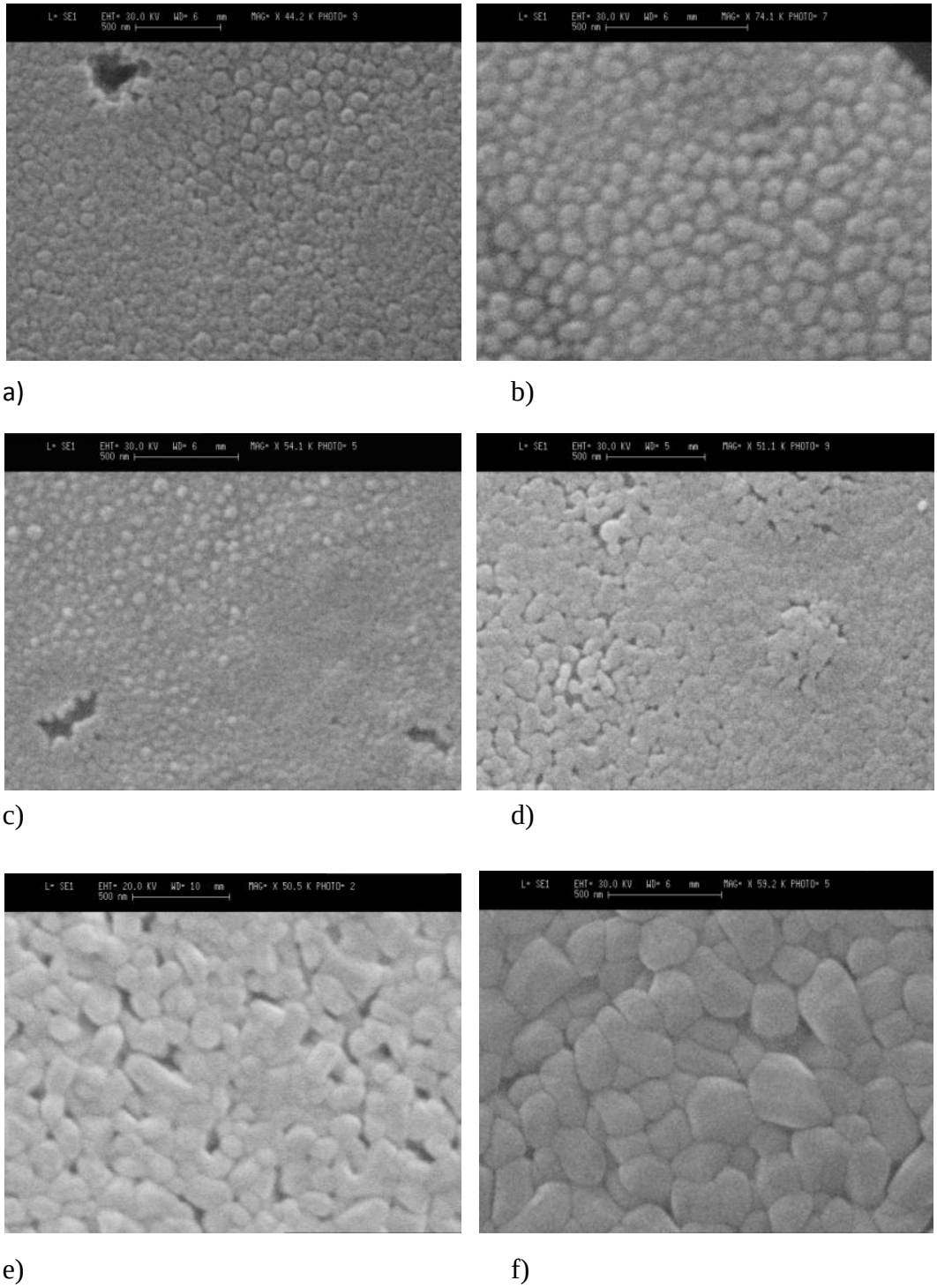

Fig. 5.21 – SEM micrographs of 3-layer iron vanadate films annealed at the temperatures: a) 250 °C, b) 350 °C, c) 450 °C, d) 550 °C, e) 600 °C and f) 650 °C, for 10 minutes per layer in oxygen.

Samples that were not subject to an annealing step afforded estimated particle sizes of 15-20 nm, shown in figure 5.22.

Fig. 5.22 – SEM micrograph of an unannealed 1-layer film of the iron-vanadium film prepared following deposition then drying in air.

5.4.3 – XRD

The XRD patterns observed for the 3-layer iron vanadate films annealed at different temperatures in oxygen are shown in figure 5.23.

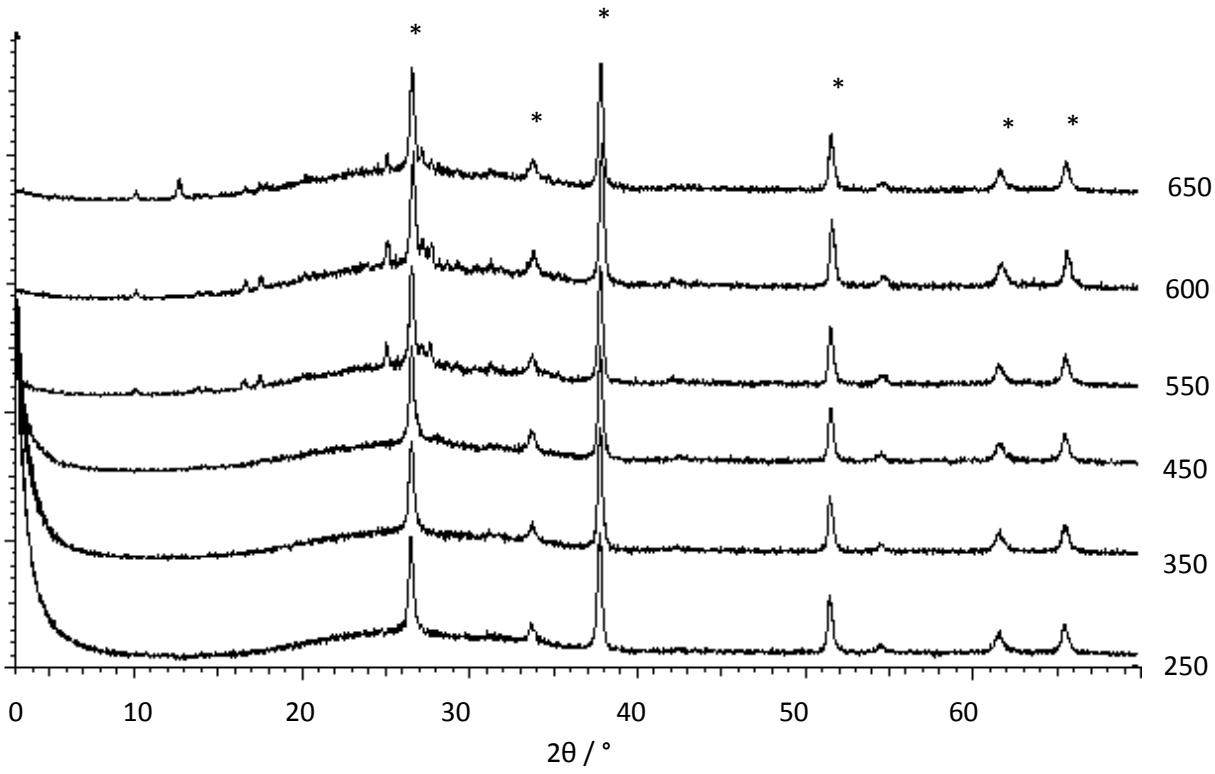

Fig. 5.23 – XRD patterns of 3 layer electrodes annealed at the stated temperatures (°C), for 10 minutes per layer in oxygen. Asterisks indicate peaks corresponding to conductive FTO layer.

The XRD patterns showed prominent peaks as tin oxide, from the FTO layer, observed for all electrodes, at 26.5°, 34°, 37.5°, 51.5°, 61.5° and 65.5° *2θ*. Due to the amorphous nature of the iron vanadate at lower temperatures, peaks corresponding to it were not observed at these temperatures. At more elevated temperatures *i.e.* ≥ 500 °C, more peaks due to material other than the F-SnO_2 layer became evident. Although they are not as prominent as the FTO peaks (due to thinness of the film), they are still clearly observed and can help to characterise the film composition. Peaks were observed corresponding to triclinic $FeVO_4$ at 10°, 13.7°, 14.2°, 16.5°, 17.5°, 20.7°, 24°, 25°, 27°, 28.2°, 28.6°, 29.3°, 31.2°, 34.5°, 35.3° and 42° *2θ* (ICDD pattern no. 038-1372). The XRD patterns may also indicate the presence of a small about of hematite and 24° and 54° *2θ*. However other signals may be obscured by the iron vanadate peaks.

5.4.4 – DR UV-Vis spectroscopy

The 3-layer iron vanadate electrodes annealed for 10 minutes per layer in oxygen at specific temperatures in the range of 250-650 °C were analysed using diffuse reflectance UV/Vis spectroscopy, in order to derive details of the band gaps of the electrodes made.

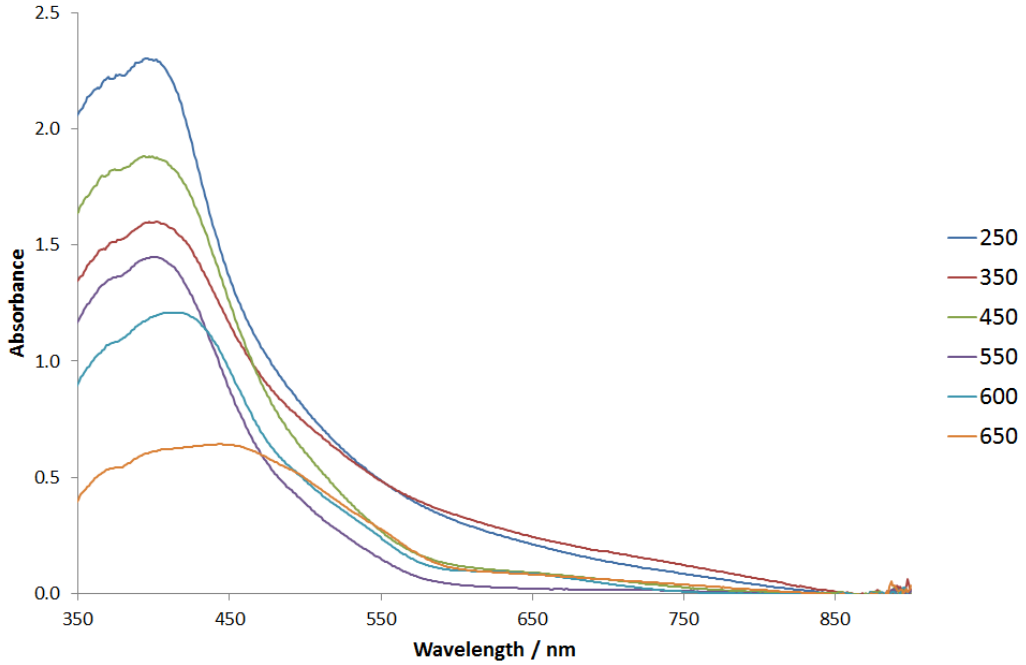

Fig. 5.24 – DR UV/Vis spectra of 3 layer electrodes annealed at the stated temperatures (°C) for 10 minutes per layer in oxygen.

From the spectra obtained (fig. 5.24), it can be seen that the band gap will change with increased annealing temperature. This is inferred by the shift in absorbance wavelength range with annealing temperature. Tauc plots were derived to estimate the band gaps (table 5.1).

Annealing temperature / °C	Estimated indirect band gap / eV
250	2.30
350	2.30
450	2.15
550	2.15
600	2.05
650	2.00

Tab. 5.1 – Band gaps derived from Tauc plots of 3 layer sol-gel electrodes annealed at the stated temperatures (°C) for 10 minutes per layer in oxygen.

There is a decrease in band gap with increasing annealing temperature, from 2.3 eV at 250 °C to 2.00-2.05 eV at 600 and 650 °C. This decrease with increasing annealing temperature is a common observation in semiconductors,[18-21] and is possibly due to crystal orientation within the film improving as crystallinity increases, which plays an important role in determining the band structure.[21]

5.4.5 – Photo-electrochemistry measurements

In order to observe the affect that increased annealing temperature and crystallinity has on the photocurrents they produce, the 3-layer electrode films gelled for 10 minutes per layer in oxygen at specific temperatures ranging from 250-650 °C were analysed using the photo-electrochemical setup used previously (figure 5.7). The resulting photocurrent measurements are presented in figure 5.25.

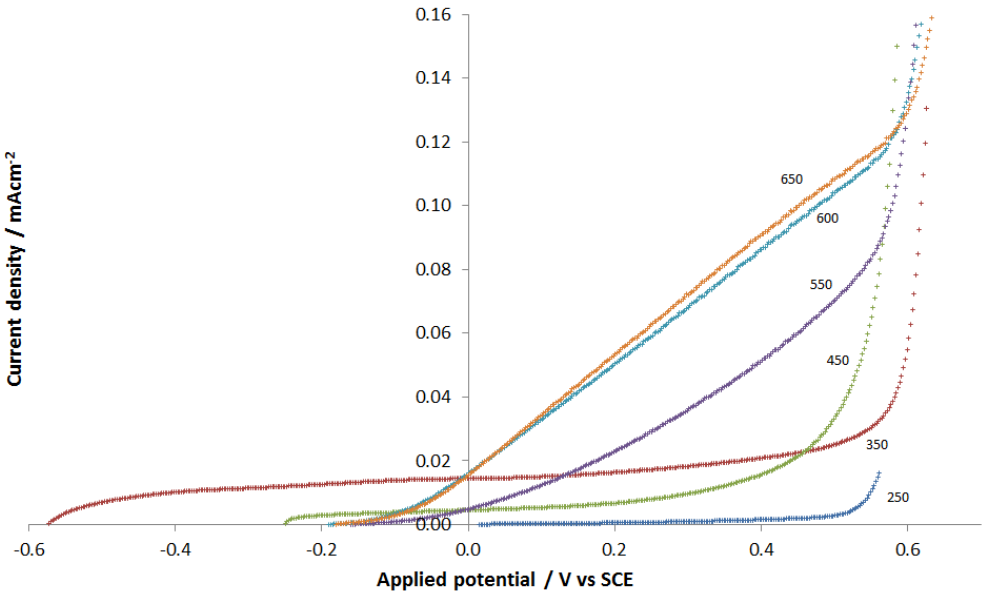

Fig. 5.25 – j/v plots of 3-layer electrodes annealed at the stated temperatures (°C), for 10 minutes per layer in oxygen. Photocurrents were recorded upon irradiation with AM1.5 light, in 0.5 M NaOH electrolyte and a 0.01 Vs^{-1} scan rate.

The *j/v* plots obtained for electrodes annealed at different temperatures, shown in figure 5.25, illustrate that there is a clear increase in the current densities of these films with increasing annealing temperature. Indeed, it should be noted that the highest photocurrent densities recorded, when annealed at 600 and 650 °C, of 0.12 $mAcm^{-2}$ were higher than was recorded for the 6-layer electrode made from the suspension of pre-formed powder, when annealed at 700 °C, as detailed in the previous chapter. The films annealed at 550, 600 and 650 °C have an onset potential of *ca.* -0.1 V vs. SCE, similar to the films reported in Chapter 4. For the films made at temperatures below 450 °C, the onset potential was difficult to determine.

5.4.6 – Post-photo-electrochemical Raman analysis

The electrodes were re-analysed using Raman spectroscopy in order to observe the stability of them. For the electrodes annealed between 250-450 °C, there was visible delamination of the films in the electrolyte, indicating a lack of mechanical stability.

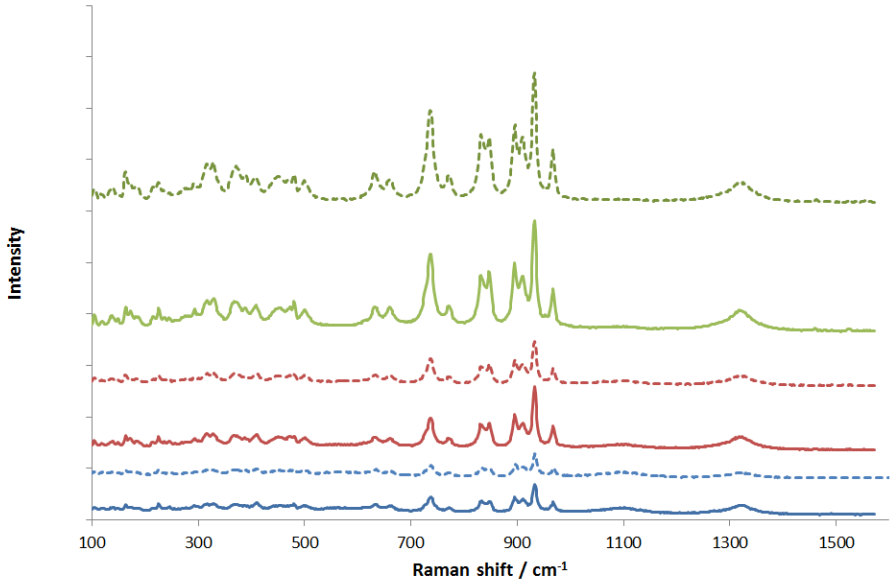

Fig. 5.26 – Raman spectra of 3-layer electrodes annealed for 10 minutes per layer in oxygen at 550 °C (blue), 600 °C (red) and 650 °C, shown before (solid line) and after (dotted line) photo-electrochemical measurements.

It can be seen from figure 5.26 that the Raman spectra before and after the photo-electrochemistry measurements, are very similar, not only in peak position, but in peak intensity. The spectra shown in the above figure are representative of the five for each film before and after photo-electrochemistry, at various points on the film. There appears to be very little difference in the spectra before and after the photo-electrochemistry measurements, indicating relatively high film stability, especially compared to all of the electrodes prepared from the iron vanadate suspension, containing the same numbers of layers, annealed for the same time and at the same temperature, as described in the previous chapter.

5.5 – Number of layers on film thickness and photocurrent density

Five $FeVO_4$ electrodes were produced from an iron-vanadium precursor solution that was allowed to gel for 10 min prior to spin coating. Each electrode was annealed at 600 °C for 10 minutes per layer and differed only in the number of layers applied. Electrodes consisting of 1, 3, 6, 12 and 24 layers were used to investigate the effect of the number of layers applied on film thickness and photocurrent density produced under AM1.5 light illumination. Characterisation was first done to observe how chemical composition, elemental distribution, and film thickness change with increasing applied layers.

5.5.1 – Film thickness: Raman microscopy

Representative Raman spectra of iron vanadate films containing 1, 3, 6, 12 or 24 layers, annealed for 10 minutes per layer at 600 °C in oxygen, are presented in figure 5.27.

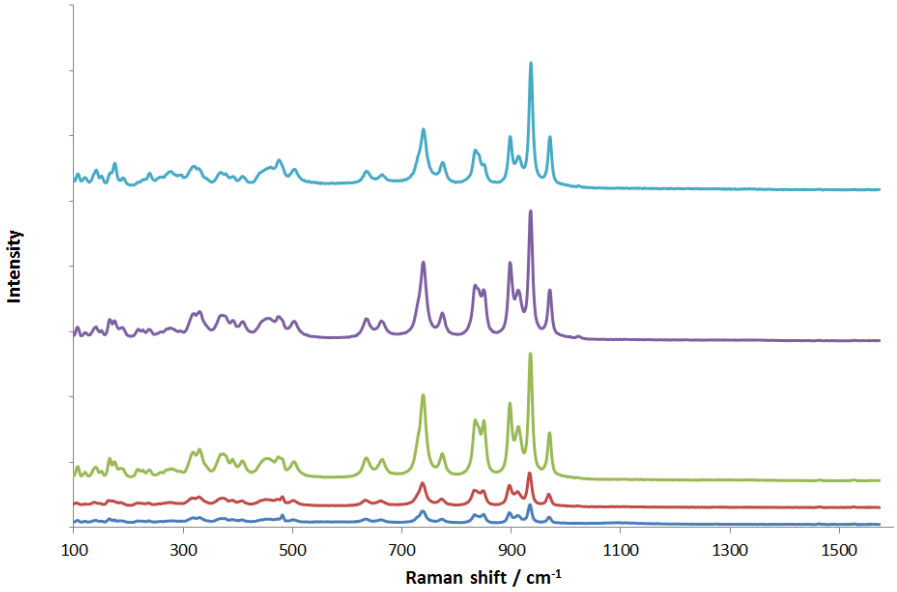

Fig. 5.27 – Raman spectra taken from iron vanadate films annealed at 600 °C for 10 minutes per layer in oxygen. The number of layers in each film were 1 (dark blue), 3 (red), 6 (green), 12 (purple) and 24 (turquoise).

The Raman spectra in figure 5.27 show uniformity in peak position, indicating a similar morphology throughout. The peaks are also typical of what has been observed previously in this chapter.[1-3, 5-7] It was observed from the Raman spectrum of 3-layer film that the intensity of the peaks increased, compared to the 1-layer film, most likely due to more material being present. The Raman spectrum of the film containing 6 layers, shows that the intensity increases compared to the 1 and 3 layer electrodes. The Raman spectra of the 12 layer and 24 layer films are of similar peak intensity as the 6 layer film, although it would be reasonable to predict that there would be another increase due to more material being present. This is due to the fact that film thicknesses have exceeded the penetration depth of the laser used to analyse the sample, and therefore, the same depth is being sampled in each measurement.

5.5.2 – Thickness measurements

It is a challenge to accurately measure thickness of films in samples such as these. This is demonstrated by the increasingly large number of methods tried by various research groups, from using different spectroscopic techniques, such as ellipsometry,[22] which analyses change of polarisation of light reflected from the film at different angles,[23] and XPS for ultra-thin films,[24] to analysing the film roughness using specific apparatus.[25, 26] Because these set-ups were unavailable, another method for measuring the thicknesses of the iron vanadate films had to be developed.

The electrodes with different numbers of layers described above were cut across the electrode perpendicular to the film, mounted in resin and polished. This method has also been used for thickness measurements by other research groups.[26-28] The electrodes were then analysed by scanning electron microscopy on the polished edge. This would afford an image that showed the $FeVO_4$ layer, the SnO_2 layer and the glass. However, in order to ensure that thickness measurements were for the active layer, rather than the SnO_2, it was necessary to analyse the elemental composition by using energy dispersive x-ray spectroscopy (EDX). Not only would this allow determination as to where the iron vanadate layer started and ended, but it would also allow observations of possible elemental migration throughout the layer during prolonged heating.

The cross-section SEM micrographs for films containing between 1-24 applied layers, annealed for 10 minutes per layer at 600 °C in oxygen, are presented in figure 5.28.

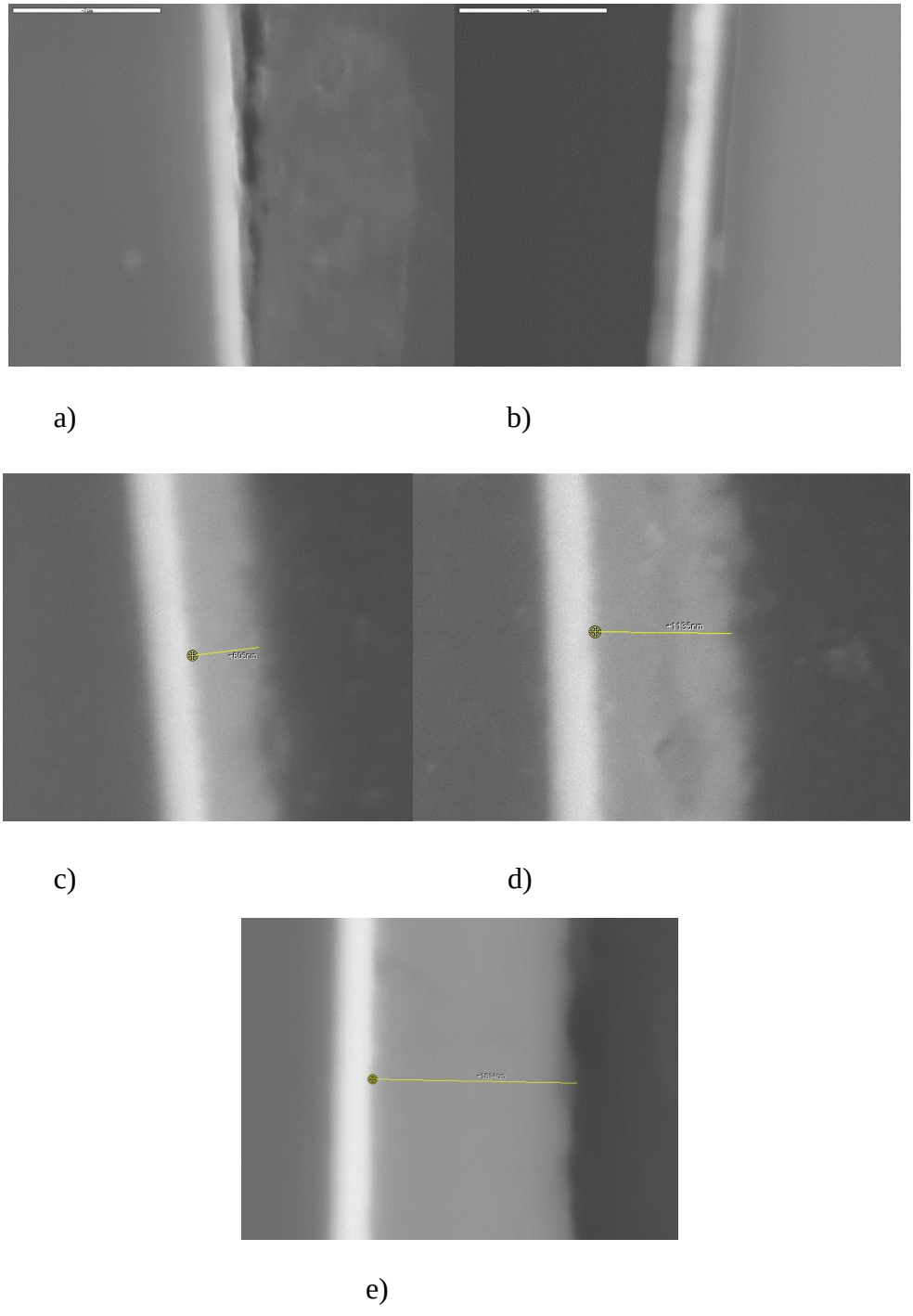

a) b)

c) d)

e)

Fig. 5.28 – SEM micrographs of iron vanadate electrodes annealed at 600 °C for 10 minutes per layer in oxygen, containing a) 1, b) 3, c) 6, d) 12 and e) 24 layers.

The thickness of the $FeVO_4$ films could be measured from the SEM images in fig. 5.28 but only after mapping of the elemental composition. This can be seen in figure 5.29, where EDX analysis is overlaid on the corresponding SEM image, and clearly shows the

presence of the silicon in the glass (red), the tin in the conductive layer (green) and the vanadium in the applied iron vanadate layer (blue). Mapping can only be visualised for three elements at a time, however the distribution of iron shown by EDX indicated that the iron was located in a region that overlapped that of the vanadium, showing an even distribution of the iron and the vanadium in the layer.

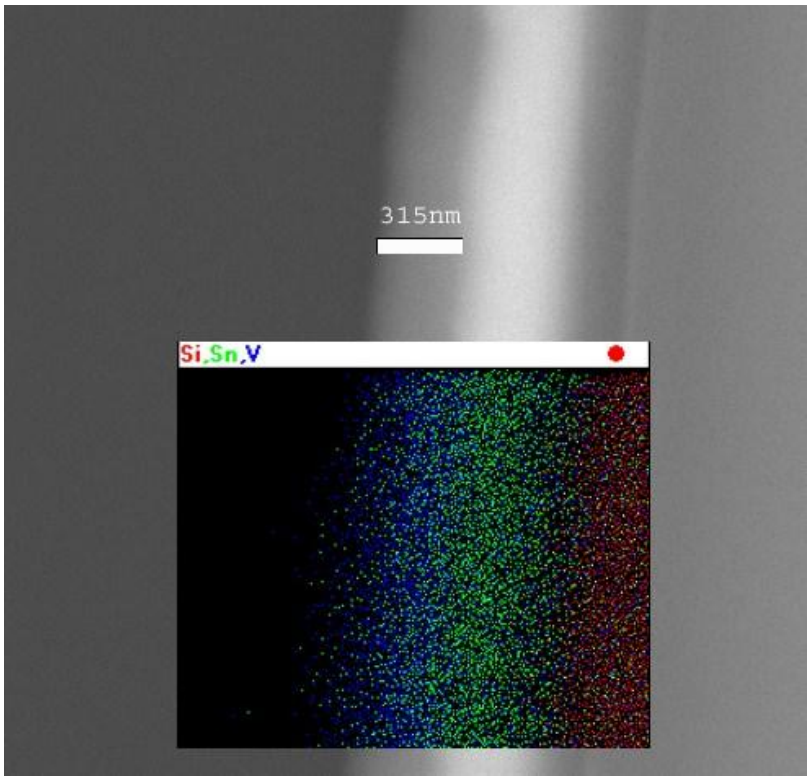

Fig. 5.29 – SEM micrograph of 3-layer electrode annealed at 600 °C for 10 minutes per layer in oxygen, superimposed EDX analysis to show different elemental layers. Shown are silicon (*red*), tin (*green*) and vanadium (*blue*).

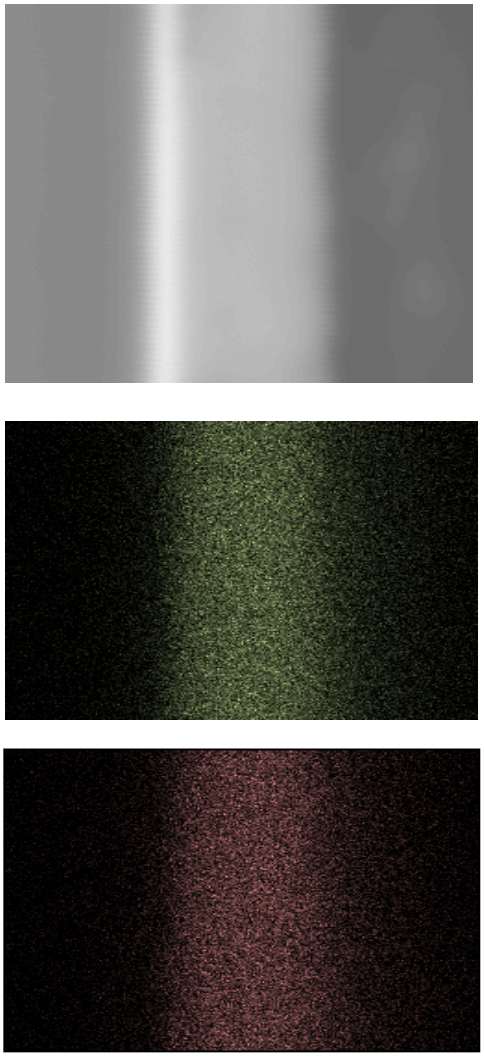

Fig. 5.30 – EDX analysis of the 24-layer electrode annealed at 600 °C for 10 minutes per layer in oxygen. Top – Micrograph of electrode cross-section. Middle – EDX analysis of the same area, showing where the vanadium is present in the image (green). Bottom – EDX analysis of the same area, showing where the iron is present (red).

Figure 5.30 shows the distribution of the main elements within the 24 layer electrode. As can be seen, there seems to be even distribution of the iron and vanadium within the film, and that the film thickness seems to be of around 1900 nm. Thickness measurements from Fig 5.28 in conjunction with EDX measurements allowed determination of how the thickness was dependent on the number of applied layers. This is summarised in fig. 5.31

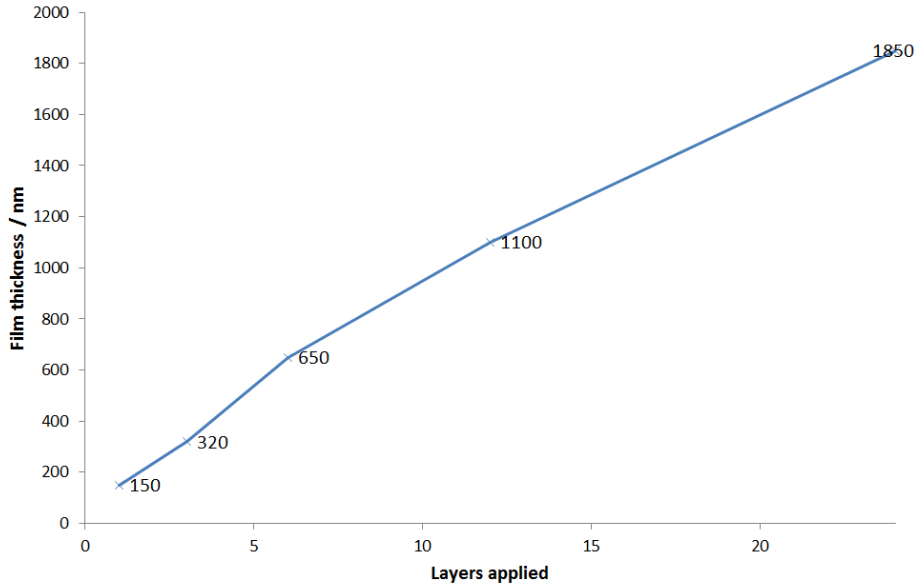

Fig. 5.31 – Variation in how the average film thickness changes with increasing applied layers.

Figure 5.31 shows that there is an almost linear relationship between the number of applied layers and the film thickness although the increase in thickness is slightly smaller for the thicker samples.

5.5.3 – Film thickness: XRD

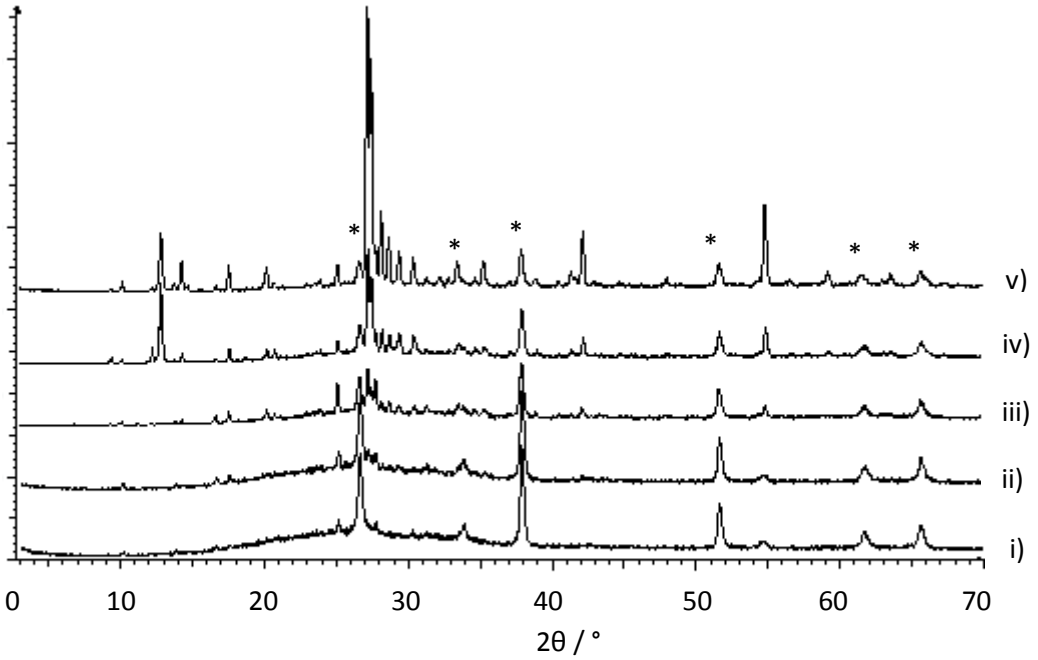

Fig. 5.32 – XRD patterns of electrode films containing: i) 1, ii) 3, iii) 6, iv) 12 and v) 24 layers. Asterisks indicate peaks corresponding to FTO.

The XRD patterns in figure 5.32 clearly show that differences occur with increasing layers. Peaks corresponding to the FTO layer, are observed at 26.5°, 34°, 38°, 51.5°, 61.5° and 65.5° *2θ*. The peaks for the film material increased in intensity with increasing layers due to increased material or increased total annealing time (therefore increased crystallinity). Peaks were observed corresponding to triclinic $FeVO_4$ at 10°, 13.7°, 14.2°, 16.5°, 17.5°, 20°, 20.7°, 24°, 25°, 27°, 27.7°, 28.9°, 29.3°, 30.3°, 31.2°, 32.2°, 32.8°, 34.6°, 35.3°, 37°, 38.9°, 40.4°, 41.3°, 42°, 42.9°, 44.6° and 45.2° *2θ* (ICDD pattern no. 038-1372). Weak hematite peaks seemed to be mostly obscured by other peaks at lower diffraction angles, but seem to be slightly more visible at larger angles at 41°, 54°, 57° and 64° *2θ*.

5.5.4 – Film thickness: UV/Vis spectroscopy

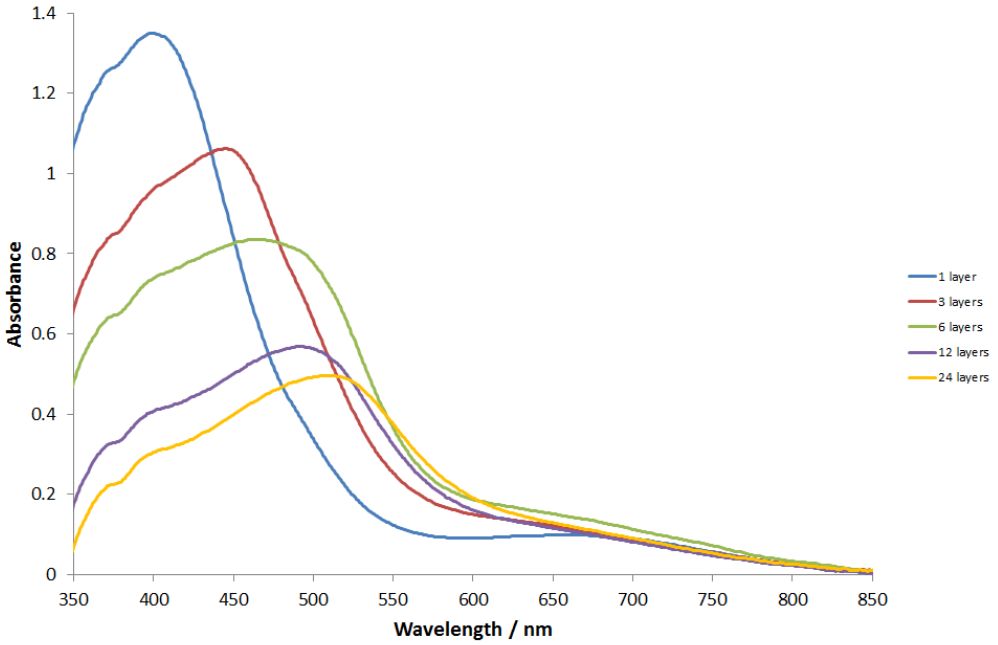

Fig. 5.33 – Diffuse reflectance UV/Vis spectra of iron vanadate electrodes annealed at 600 °C for 10 minutes per layer in oxygen, containing 1, 3, 6, 12 and 24 layers.

It was observed in figure 5.33 that the absorbance drops significantly, as well as broadens, when more layers are applied. This is possibly the result of scattering changes with different particle sizes present as the number of layers, and therefore annealing steps, is increased. It is possible that as more layers are added, material deposited in the initial layers could include larger particles, which could alter the light scattered by the film. Smaller particles tend to scatter shorter wavelengths more effectively.[29]

5.5.5 – Effect of film thickness on photocurrent density.

Photo-electrochemistry measurements were taken using the iron vanadate films annealed at 600 °C for 10 minutes per layer in oxygen, containing increasing numbers of layers, (1-24). These measurements were done in order to determine whether increasing the number of layers increases the photocurrents produced, to what extent, and whether there is a limit. The resultant *j/v* plots a shown in figure 5.34.

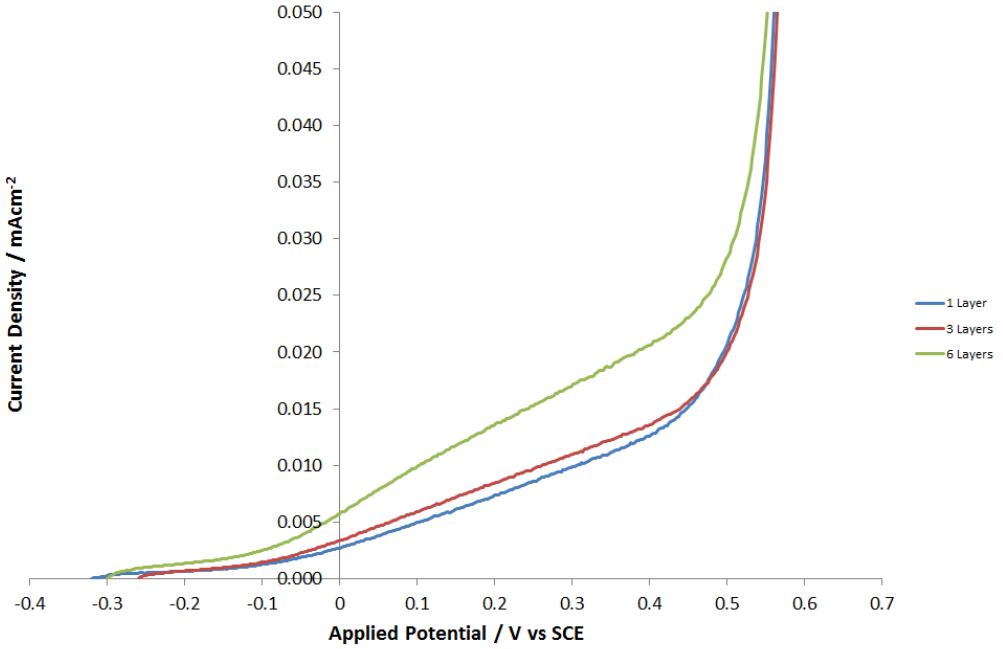

Fig. 5.34 – Photo-electrochemical performance of electrode films containing 1, 3 and 6 layers.

Figure 5.34 shows the photocurrents recorded for the electrodes containing 1, 3 and 6 layers. The electrodes containing 12 and 24 layers delaminated upon entry into the electrolyte. The physical delamination is possibly due to the continual expansion and contraction of the glass substrate during the annealing steps and relaxing the film to a different extent to the substrate due to different thermal expansion coefficients, thereby stretching the film and weakening it. From figure 5.34, it appears that there is an increase in photocurrent with increasing layers.

5.6 – Incident-Photon-to-Current-conversion-Efficiency (IPCE)

IPCE measurements for 3-layer and 6-layer electrodes were undertaken to determine the efficiency in converting photons into current and to determine the range of wavelengths that the iron vanadate is active towards. Upon exposure to a particular wavelength of monochromatic light, the difference between the photocurrent generated and the dark current can be used to calculate the conversion of incident photons to current if the photon flux is firstly known, using equation 5.1.

$$\%\, IPCE = \frac{(1240)(i_{photocurrent}\ \mu A cm^{-2})}{(\lambda\ nm)(j_{photons}\ \mu W cm^{-2})} \times 100\% \qquad \text{equation 5.1}^{15}$$

The incident photon-to-current conversion efficiencies as a function of incident wavelength gave the photo-action spectrum in fig. 5.35.

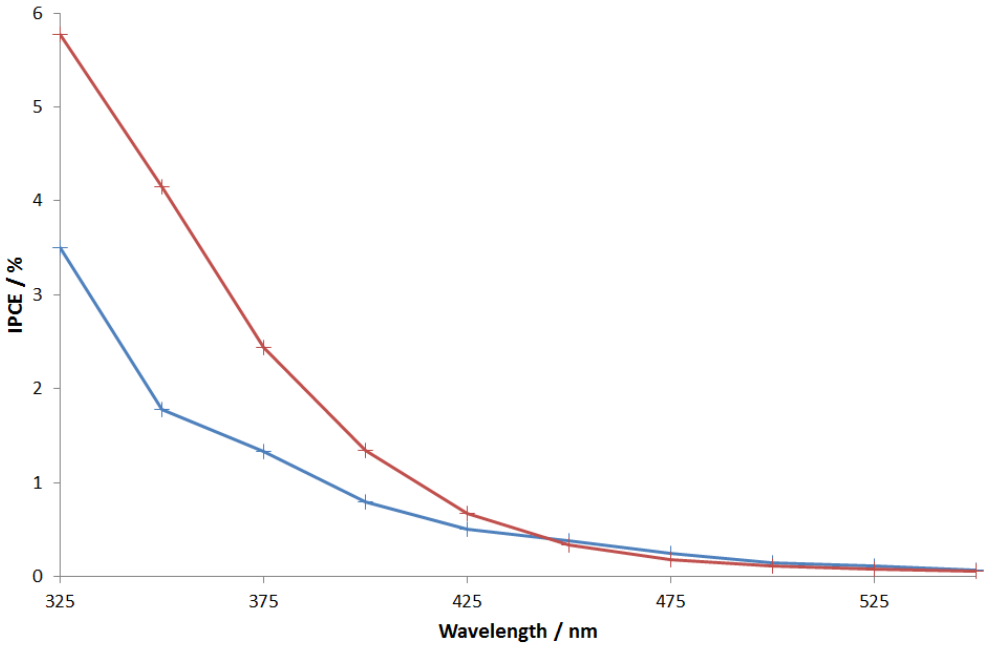

Fig. 5.35 – IPCEs for iron vanadate films containing six (blue) and three (red) layers. Each layer was gelled for 10 minutes and then annealed at 10 minutes at 600 °C in oxygen. All currents were recorded using a 0.5 M NaOH electrolyte at 0.45 V vs. Ag/AgCl.

It can be seen from figure 5.35 that the efficiency decreases with increasing wavelength. It can also be seen that, overall, the 3-layer electrode gave a higher efficiency than the 6-layer electrode, which could be due to increased distance required for the electrons to travel to the back contact in the 6-layer electrode, increasing the risk of charge trapping

and recombination. The films appear to be active up to the 550 nm wavelength analysed, although with efficiencies of 0.065 %. It is expected that these electrodes would be active to some extent up to wavelengths of 610-630 nm, corresponding to the band gap of 2.00-2.10 eV calculated. Absorbance is also observed in this region within the UV/Vis spectra of these films. Comparing these results with other vanadates, such as indium vanadate and bismuth vanadate, shows that the IPCEs given in figure 5.35 are higher than those reported for $InVO_4$: a maximum of 0.3% at 350 nm, but using 0.8 V vs. Ag/AgCl of applied potential.[30] The maximum IPCE reported for $BiVO_4$ strongly depends on the synthetic route. IPCEs have been reported from 2.2% at 450 nm using 0.65 V vs. Ag/AgCl applied potential,[31, 32] to 60 % at 360 nm using 1.00 V vs. Ag/AgCl.[31]

5.7 – Medium-term photocurrent stability

Chronoamperometry measurements were undertaken in order to observe the photo-stability of the electrode. Here, electrodes were continuously irradiated with AM1.5 light, at an applied potential of 0.4 V vs. SCE while monitoring the photocurrent produced. This analysis allows a visualisation of how the performance of the film deteriorates or improves during photolysis of water.

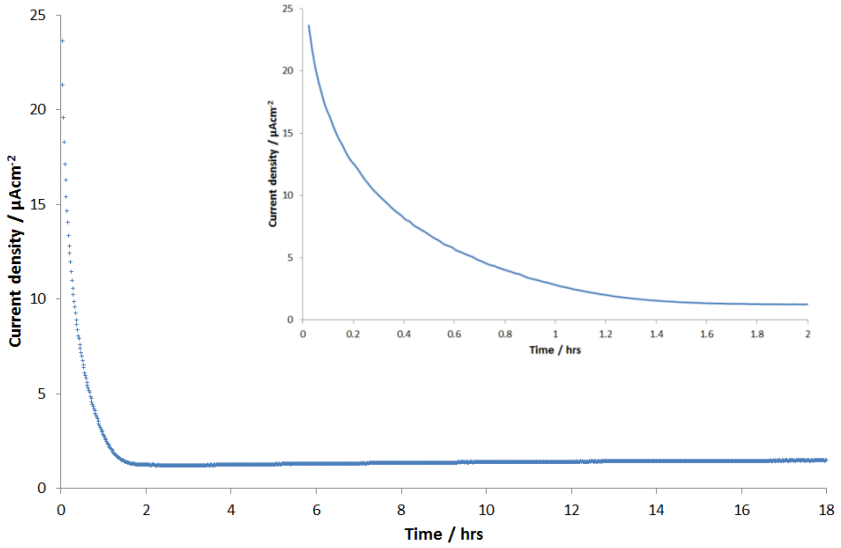

Fig. 5.36 – Chronoamperometry plot of a 6-layer iron vanadate film, made by gelling the deposited precursor for 10 minutes and annealing for 10 minutes at 600 °C per layer. Chronoamperometric measurements were performed under continuous AM1.5 illumination and an applied voltage of 0.4 V vs. SCE. *Inset*: Data from of the first two hours of the experiment, where the decrease in current density is most apparent.

The chronoamperometry data in figure 5.36 clearly shows that there is a decrease in produced photocurrent within the first 1.5 hours, where the produced photocurrent appears to stabilise at *ca.* 1.3 μAcm^{-2}, a value that is similar to the dark current. These findings indicate that the iron vanadate film appears to lose its photo-activity over the course of two hours of continuous photo-electrochemical measurements, possibly due to film degradation, as the sample colour changed slightly.

5.8 – Effect of pH of precursor sol

The dependence of the sol pH was investigated, due to the fact that pH can affect the stability of the sol.[33] The sol stability can be enhanced by the pH, if the conditions encourage the iron and vanadium to interact within the precursor and fall into the matrix structure.[33] As well as the pH of vanadium being able to affect its coordination tendencies and its oxidation state in nature, the acidity or basicity of the sol can essentially act as a catalyst for the gelling process, encouraging the cross-linking within the sol.[34] Thus, an alkaline sol (pH > 7) was made by dissolving a 1:1 ratio of iron nitrate and vanadyl acetyl acetonate in acetyl acetone, acetic acid, followed by adjustment of pH by addition of triethylamine.

5.8.1 – Effect of precursor pH on film composition: Raman spectroscopy

Electrodes were prepared with iron vanadate precursor sols of different pH, containing 3 layers, annealed at 600 °C in oxygen for 10 minutes per layer. The effect of precursor pH on film crystallinity and chemical composition was investigated by Raman spectroscopy, presented in figure 5.37.

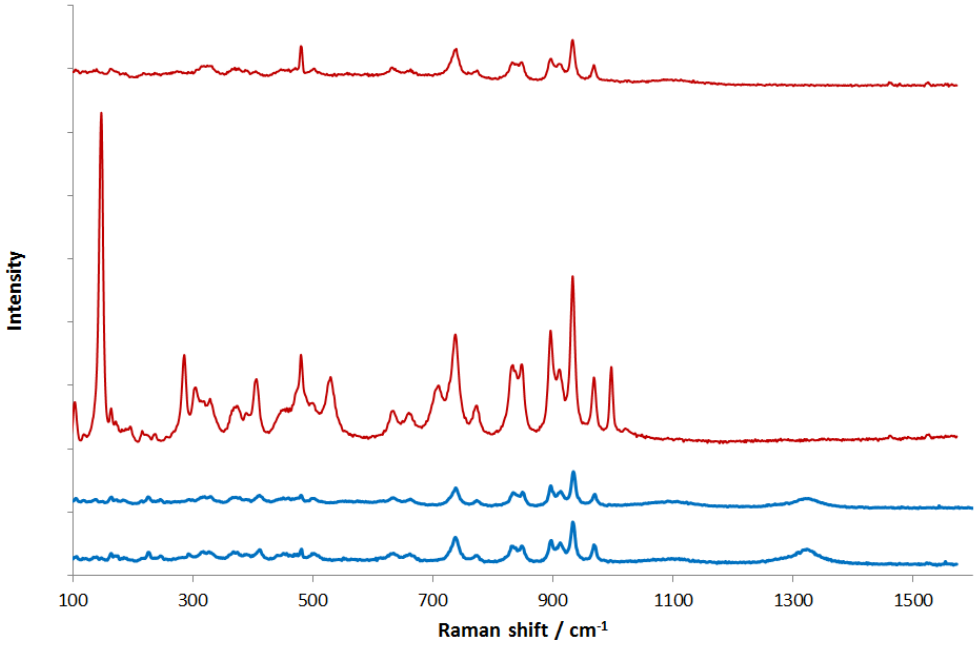

Fig. 5.37 – Representative Raman spectra of 3-layer iron vanadate films made using alkali sol (red) and acidic sol (blue). Each film was gelled for 10 minutes per layer and annealed at 600 °C for 10 minutes per layer.

Figure 5.37 shows that while the majority of the bands associated to iron vanadate are present in the spectra of both electrodes, the chemical composition of the electrode made using the acidic sol is more uniform, as demonstrated by the fact that the Raman spectra consistently show similar profiles independent of location on the electrode surface that was analysed. Only two are shown for comparison purposes. However the spectra taken from the alkaline electrode show that the Raman spectra contain much greater variation throughout the film surface. This indicates a lack of homogeneity in chemical composition. For example, there are extra peaks at 997 and 150 cm^{-1}, which are observed in vanadium oxide,[35] however this is unlikely to have any effect on the photo-response. Although these peaks were observed, the majority of the points analysed on the electrode surface show only peaks for iron vanadate.

5.8.2 – Alkali sol UV/Vis

A Tauc plot was derived from the UV/Vis spectrum of the 3-layer iron vanadate electrode made using the alkaline sol, in order to compare the derived band gap to that of the film made from the acidic sol.

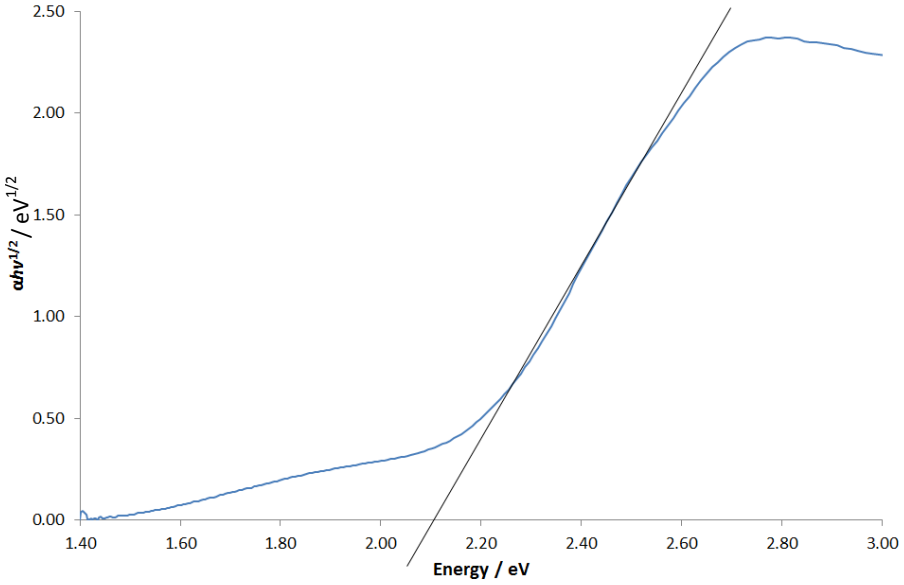

Fig. 5.38 – Tauc plot of 3-layer iron vanadate film made using an alkali sol, gelled for 10 minutes per layer and annealed at 600 °C for 10 minutes per layer.

The Tauc plot suggests that the observed band gap is slightly larger than has been seen previously, at *ca.* 2.10 eV, compared to 2.05 eV, shown in table 5.1.

5.8.3 – Effect of precursor pH on surface morphology

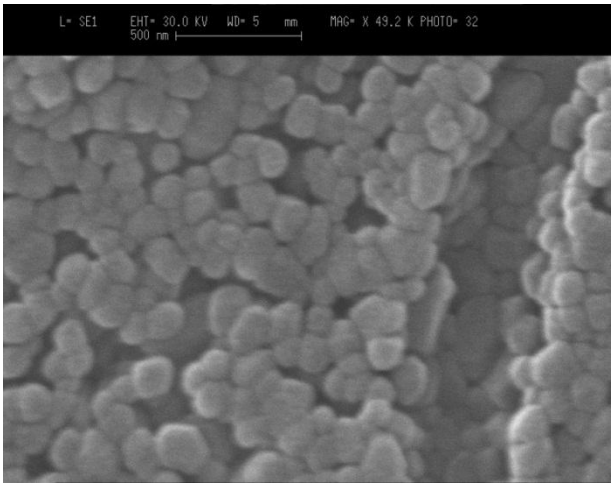

Fig. 5.39 – SEM micrograph of 3-layer iron vanadate film made using an alkali sol, gelled for 10 minutes per layer and annealed at 600 °C for 10 minutes per layer.

The SEM image of the alkaline sol film (fig. 5.39) shows more rounded particles than those observed in the corresponding acidic film (fig. 5.21e), which appeared, on average, to be more elongated. The particles in the micrograph also appear less packed and contain a more porous arrangement than observed for its acidic counterpart (fig. 5.21e). Finally, the acidic sol contained an average particulate size of *ca.* 100-120 nm in diameter (fig. 5.21e). In comparison, the particulate size observed is *ca.* 80-100 nm.

5.8.4 – Effect of sol pH on photo-electrochemical response

Photo-electrochemical measurements were performed on the 3-layer iron vanadate films made using acidic and alkali sols. The films were annealed at 600 °C in oxygen, for 10 minutes per layer. These measurements were performed in order to observe how the property differences determined within this section will affect the photocurrents produced. The measurements are presented in figure 5.40.

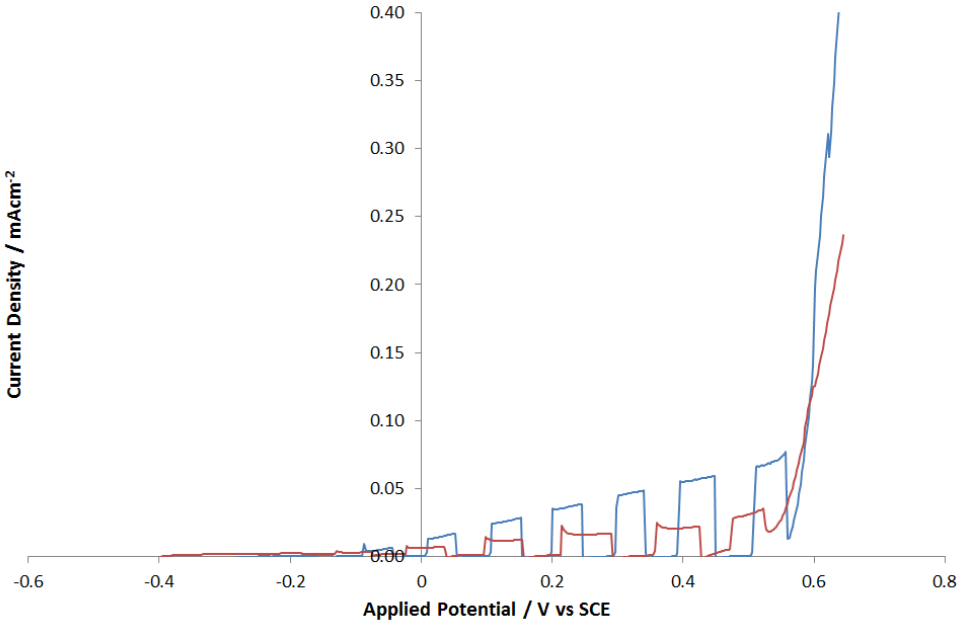

Fig. 5.40 – Photo-electrochemical measurements of 3-layer iron vanadate films made using an alkali sol (red) and acidic sol (blue), gelled for 10 minutes per layer and annealed at 600 °C for 10 minutes per layer.

Photocurrent measurements under AM1.5 illumination are given in figure 5.40. Light was blocked every 5 seconds and the corresponding dark current is shown after the sharp decrease in current. It can be seen from the above figure that the film created from an acidic sol produced a higher photocurrent (0.066 $mAcm^{-2}$ at 0.5 V vs. SCE) than that of

the corresponding alkaline film (0.030 $mAcm^{-2}$ at 0.5 V vs. SCE). This difference could be caused by variations in the film composition as evidenced by Raman spectroscopy (fig. 5.37). It was observed that the films prepared from an alkaline precursor were much more heterogeneous than those prepared from an acidic precursor, and therefore the overall performance of the electrode would be less, particularly as the additional presence of V_2O_5 was observed in the former case. This was thought not to be photoactive and to test this, a vanadium oxide electrode consisting of a 3-layer film annealed and gelled under the same conditions as the electrodes within this section, was prepared from a sol that was analogous to the one used throughout this chapter. No photocurrents were observed.

It appears from these results that in this particular sol, acidic conditions are more favourable for catalysing the gelling process and therefore consequently creating a more uniform sol and resulting film. This is most likely due to the acidic conditions driving the formation of oxidised vanadium ions, whereas the alkaline conditions favour the production of vanadium hydroxides and oxohydroxides,[36] making it more difficult to combine with the iron in the reaction.

5.9 – Effect of oxidation state of the iron precursor

The effect of the oxidation state of the reactant iron in the precursor was investigated. Here, an equimolar amount of iron (II) chloride or iron (III) chloride to vanadium acetyl acetonate, was dissolved in acidic acetyl acetonate to form the sol. The iron (II) chloride required sonication to fully dissolve.

5.9.1 - Effect of iron oxidation state on film composition: Raman spectroscopy

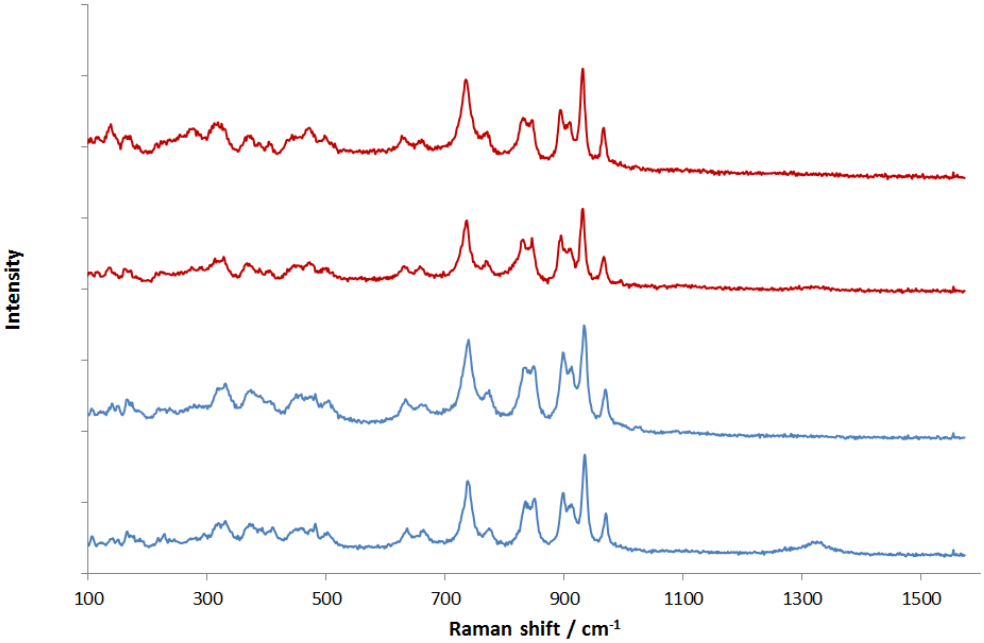

Fig. 5.41 – Representative Raman spectra of 3-layer electrodes gelled for 10 minutes and annealed for 10 minutes at 600 °C per layer, made using Fe^{2+} (*blue*) and Fe^{3+} (*red*).

The Raman spectra in figure 5.41 show that iron vanadate and hematite bands are present and there does not appear to be much difference in peak intensity between the Raman spectra obtained. The only difference is that on the film made using Fe^{3+}, there are areas which produced Raman spectra with a slightly higher baseline and absolute intensity was consequently lower. This could indicate that the film made using Fe^{3+} was slightly more amorphous than the film made using Fe^{2+}.

5.9.2 - Effect of iron oxidation state on film composition: XRD

To investigate whether or not there was a decrease in crystallinity when using Fe^{2+} within the precursor, the electrodes were analysed by XRD. The resultant diffractograms are shown in figure 5.42.

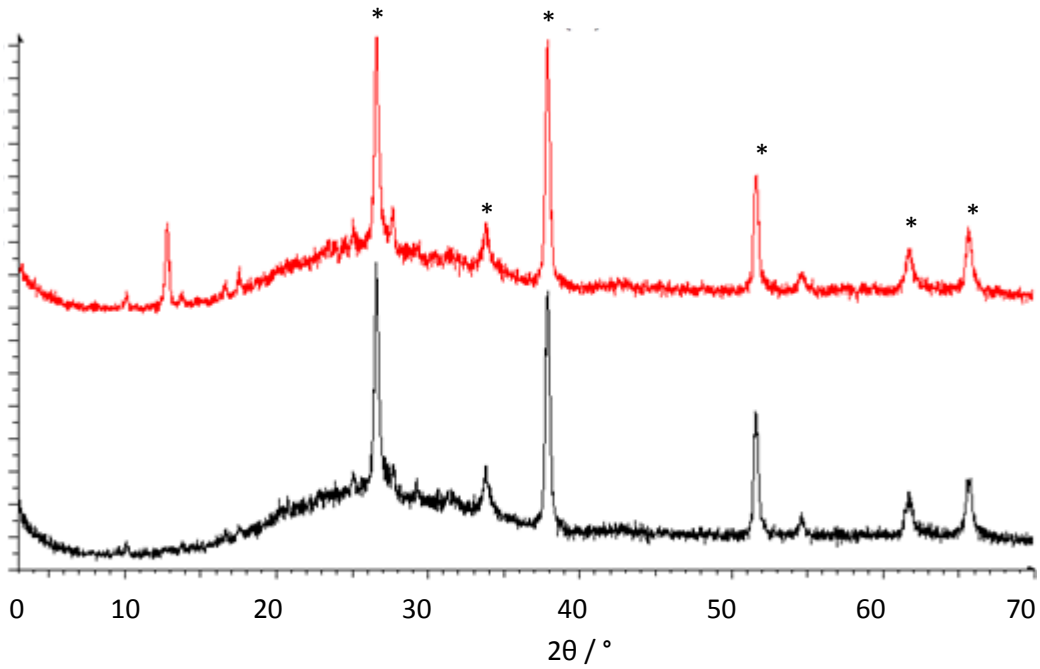

Fig. 5.42 – XRD patterns of 3 layer films gelled for 10 minutes, and annealed for 10 minutes at 600 °C per layer using Fe^{2+} (*black*) and Fe^{3+} (*red*). The asterisks indicate peaks indicating FTO on the electrode.

The above figure shows little difference between the two electrodes. The main peaks seem to correspond to tin oxide and triclinic iron vanadate. $FeVO_4$ peaks are observed at 10°, 13.7°, 16.5°, 17.5°, 20°, 20.7°, 24°, 25°, 27°, 27.7°, 28.9°, 29.3°, 30.3°, 31.2°, 32.2°, 32.8°, 34.6°, 35.3°, 37°, 38.9°, 41.3°, 42°, 42.9°, 44.6° and 45.2° 2θ (ICDD pattern no. 038-1372).

5.9.3 – Effect of iron oxidation state on film composition: UV/Vis Tauc plots

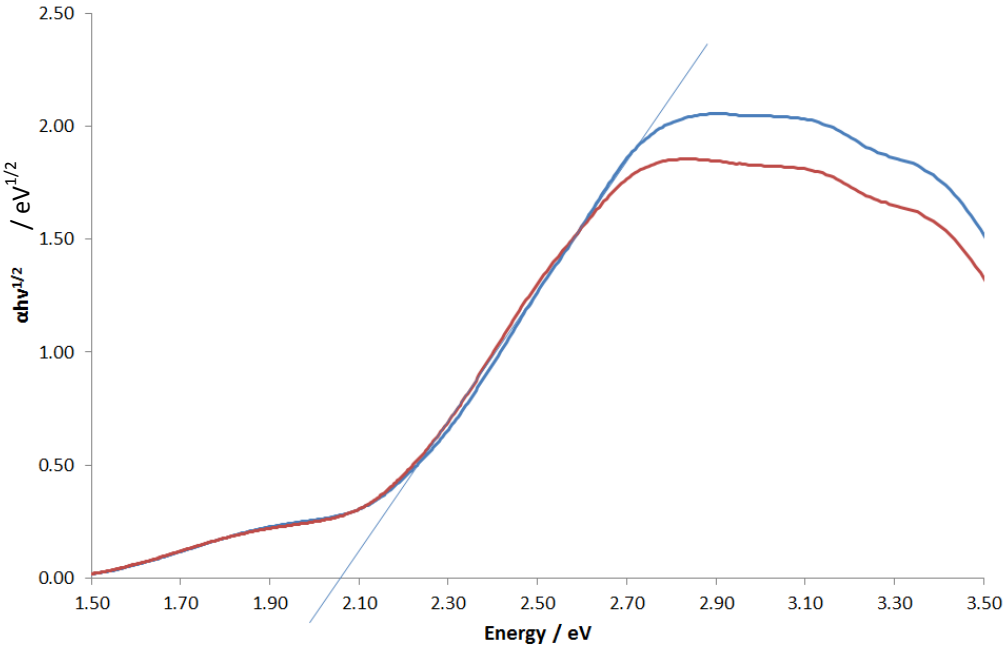

Fig. 5.43 – Tauc plots of 3 layer iron vanadate films made using iron (II) chloride (*blue*) and iron (III) chloride (*red*) as iron sources, annealed at 600 °C for 10 minutes per layer, and gelled for 10 minutes per layer.

The Tauc plots of the electrodes made from iron (II) and iron (III), had very similar shape, and give an indirect band gap of *ca.* 2.05 eV, indicating that there was little appreciable difference in the observed absorbances of the electrodes.

5.9.4 – Effect of iron oxidation state on film composition: photo-electrochemistry

Photo-electrochemical measurements were taken from the 3-layer iron vanadate films annealed in oxygen for 10 minutes per layer at 600 °C, made using iron (II) chloride and iron (III) chloride in order to observe whether the difference in reactant oxidation state decreases or increases photo-activity. The resultant *j/v* plots are shown in figure 5.44.

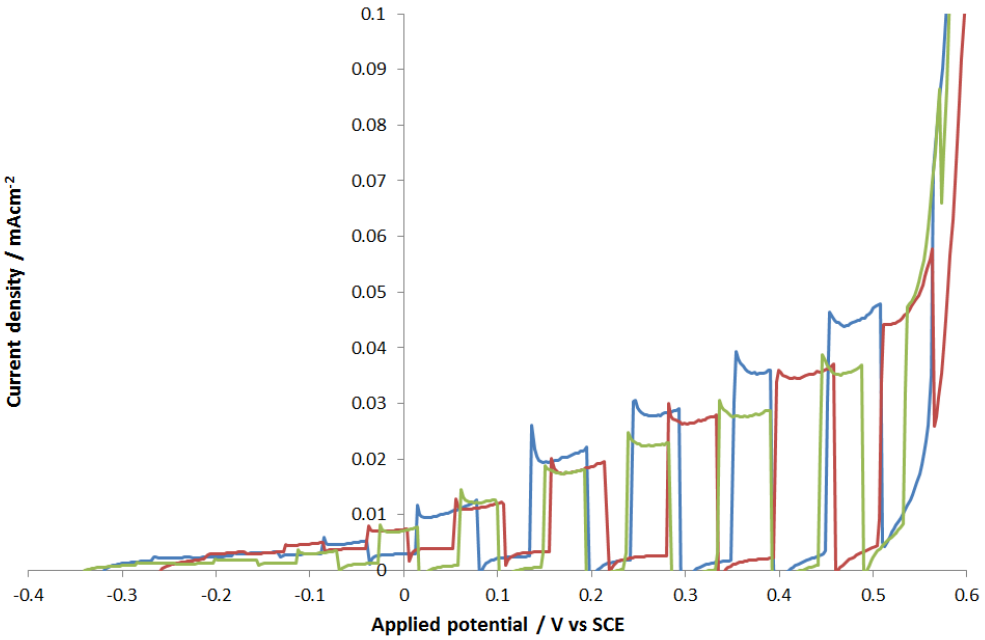

Fig. 5.44 – *j/v* plots of 3 layer iron vanadate films made using iron (II) chloride (*blue*) and iron (III) chloride (*red*), compared to the $FeVO_4$ electrode made using iron (III) nitrate (*green*). Films were annealed at 600 °C for 10 minutes per layer, and gelled for 10 minutes per layer.

The *j/v* plots from the electrodes above, show that there is very little difference between the current densities obtained from the electrodes made using iron (II) chloride, iron (III) chloride and iron (III) nitrate, showing that the oxidation state of the reactant iron was not a limiting factor within this synthesis. Studies into the effect of metal oxidation state and counter-ion on structural composition and performance changes depending on the iron source of a semiconductor, have previously been done for iron oxide, by Sartoretti *et al*,[37, 38] who observed the effect of changing precursor salt, *e.g.* iron (III) nitrate, iron (III) chloride and iron (III) acetylacetonate on iron oxide films. A clear difference in photo-electrochemical response was observed between iron nitrate and iron chloride derived films. Furthermore, absorption of iron chloride derived films was higher than those derived from iron acetylacetonate. In the case of the results herein, the difference of counter ions involved *i.e.* Cl^- and NO_3^-, was not an influencing factor in the product formed. This could be due to the fact that the same product is formed, as observed in the XRD patterns and Raman spectra.

5.10 – Effect of precursor composition

As explained in the previous section, the effect of counter ions within the iron precursor for producing the iron oxide photoanodes has been previously reported.[37, 38] Although the chloride and nitrate ions did not affect the photo-electrochemical performance of the iron vanadate electrodes reported herein, others may do so. The other precursor investigated by Sartoretti *et al.* is that of iron (III) acetlyacetonate.[37, 38] Using this as an iron source eliminates the possible use of Cl^- ions which may interfere with underlying photochemistry. It also decreases the number of counter ions, as acetylacetonate is already present in the vanadium source, as well as in the solvent (acetylacetonate).

5.10.1 – Iron acetylacetonate

A 3-layer iron vanadate electrode was made by dissolving an equimolar quantity of iron acetylacetonate and vanadyl acetyl acetonate in an acidic acetylacetone solution. This sol was then dropped on the electrode, gelled for 10 minutes per layer, spin coated, and then annealed for 10 minutes in oxygen at 600 °C per layer.

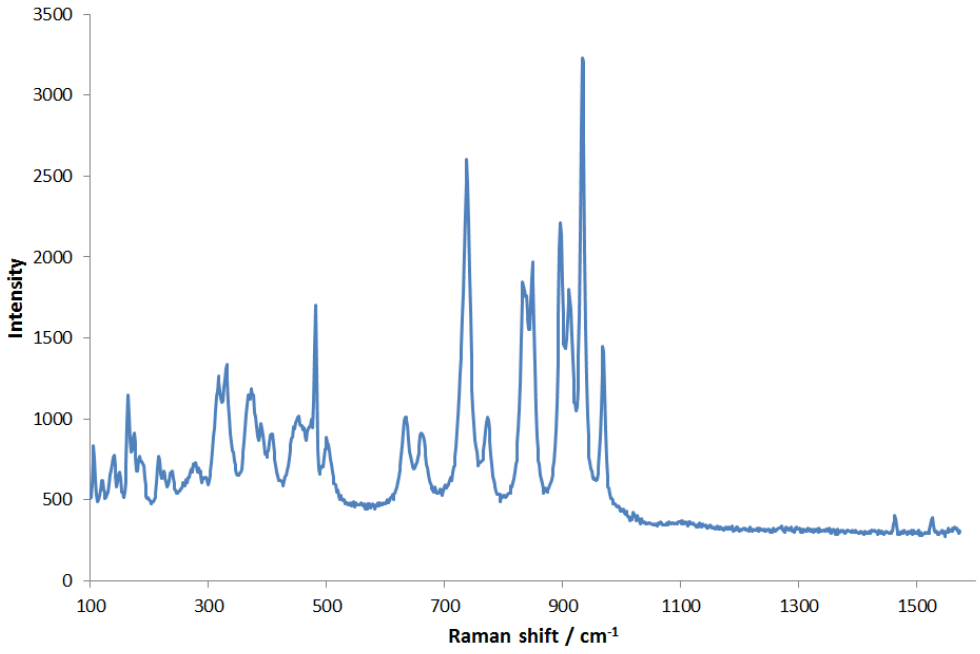

Fig. 5.45 – Representative Raman spectrum of the 3-layer iron vanadate film, made using iron acetylacetonate, gelled for 10 minutes per layer, annealed for 10 minutes at 600 °C per layer.

The Raman spectrum shown in fig. 5.45 is representative of five points analysed on the film surface. The Raman spectra produced were very similar, producing the same bands, and similar intensities, and is therefore an homogenous film. The absolute peak intensities observed were similar to those seen for iron nitrate derived 3-layer thin films. The bands observed correspond to that of triclinic iron vanadate,[1-3] and there were no instances of the observation of bands attributed to hematite at any point on the film.

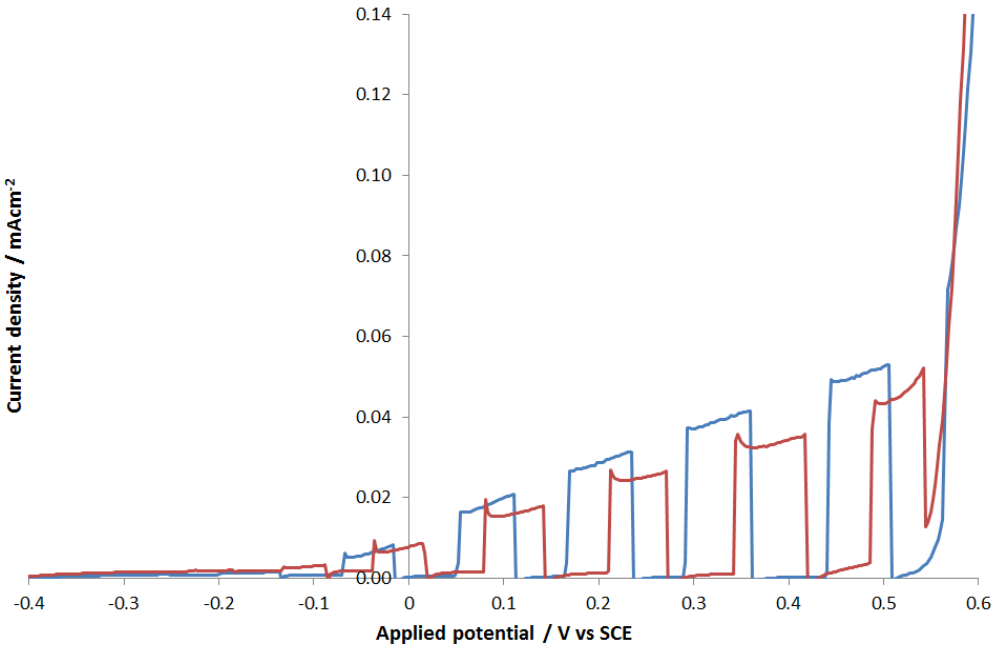

Fig. 5.46 – *j/v* plots of the 3-layer iron vanadate films, made using iron acetylacetonate (*red*) and iron nitrate (*blue*) precursors. Each layer was gelled for 10 minutes and annealed for 10 minutes in oxygen at 600 °C.

The above figure shows that there is little difference between the films made using iron acetylacetonate and using iron nitrate (producing 0.044 and 0.051 $mAcm^{-2}$ at 0.5 V vs. SCE, respectively), although the electrode made from using iron nitrate afforded a slightly higher photo-current density. Sartoretti *et al.* also showed similar photocurrents when using either of the precursors as an iron source, when investigating iron oxide.[37, 38]

5.10.2 – Alkoxide based precursors

Vanadium alkoxides have also been used to produce sols for the deposition of thin films, mainly vanadium oxoisopropoxide.[3, 39] Thus, equimolar amounts of the vanadium oxoisopropoxide, and iron nitrate were stirred in *n*-propanol, to produce an orange-brown solution. 3-layer electrode films were then made by covering a substrate in this solution, gelling for 10 minutes, spin coating and then annealing in oxygen for 10 minutes per layer. Electrodes were prepared at a variety of temperatures, but Raman analysis showed very low intensity iron vanadate bands from 550 °C to 650 °C, and the photocurrents observed were negligible. This is possibly a result of the reported instability of the sol,[3] confirmed by these films.

The question still remained, however, as to whether using an alkoxide could improve the film performance. Electrodes were made using iron ethoxide in acetic acid, combined with vanadyl acetyl acetonate in acetylacetone. In this case, a quantity of iron ethoxide was firstly dissolved in part of the acetylacetone, and then added to the acetic acid. This was then added to the vanadyl acetyl acetonate, dissolved in the remainder of the acetylacetone. The iron ethoxide was difficult to dissolve, and only appeared to do so when a concentration of 0.029 M was used instead of 0.2 M, as was used in the previous sols, with the sol continuously sonicated. Therefore the concentrations of iron and vanadium in the precursor solution were reduced accordingly and in order to deposit a comparable quantity of material as the previous iron nitrate-based three-layer electrodes, 21 layers of ethoxide-based precursor had to be deposited. Two of these ethoxide electrodes were prepared. For comparison, a 21-layer electrode was made from a precursor sol containing 0.029 M iron nitrate and vanadyl acetyl acetonate. Also for comparison, a 3-layer electrode was made using a precursor containing 0.2 M iron nitrate and vanadyl acetylacetonate, as per the previous synthesis. All electrodes were annealed at 600 °C for 10 minutes per layer.

5.10.2.1 – Iron ethoxide based precursor: Raman spectroscopy

The iron vanadate films made using iron ethoxide and iron nitrate were analysed using Raman spectroscopy in order to observe how crystallinity and chemical composition are altered, not only with the change of iron precursor, but also with increased layers of less concentrated sol. The obtained Raman spectra are shown in figure 5.47.

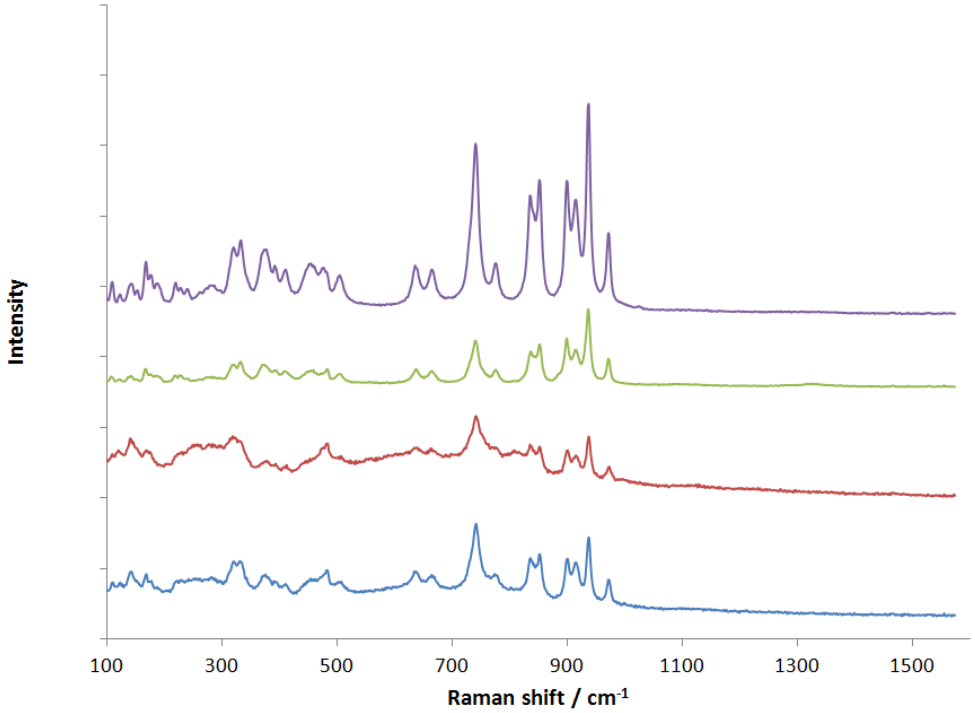

Fig. 5.47 – Representative Raman spectra of 21-layer electrodes made using iron ethoxide (blue and red), 21-layer electrode made using iron nitrate (green) and a 3-layer electrode made using iron nitrate (purple). 21-layer electrodes were made using 0.029 M of iron and vanadyl acetylacetonate, and the 3-layer electrode was made using 0.2 M of iron nitrate and vanadyl acetylacetonate. Each applied layer was gelled for 10 minutes, and annealed for 10 minutes at 600 °C.

From the Raman spectra of the four electrodes made for this investigation, there is a difference between the electrodes made using iron ethoxide (blue and red) and those made using iron nitrate (green and purple). The electrodes made using iron nitrate, show the bands expected for iron vanadate and occasionally hematite. The Raman spectra for the electrodes made using iron ethoxide are similar to the electrodes made using iron nitrate, but the baseline is significantly higher.

5.10.2.2 – Ethoxide based precursors: XRD of resultant films

XRD was performed on the iron vanadate electrodes made using iron nitrate and iron ethoxide, in order to observe possible changes in chemical composition and crystallinity between them. The resultant diffractograms are presented in figure 5.48.

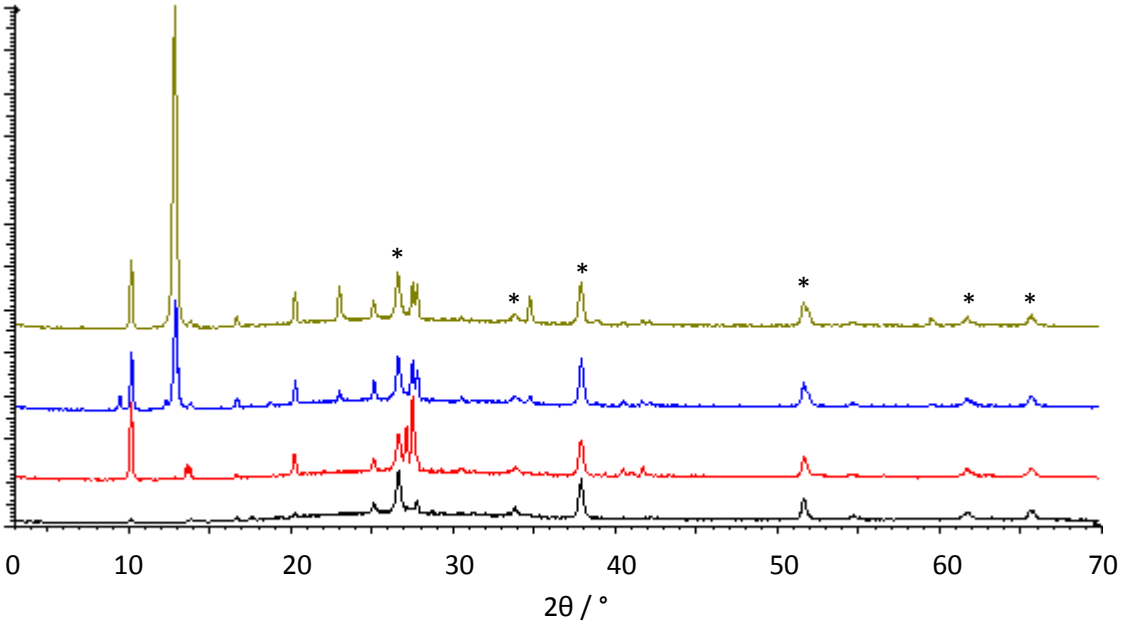

Fig. 5.48 – XRD patterns of 21-layer electrodes made using iron ethoxide (blue and green), 21-layer electrode made using iron nitrate (red) and a 3-layer electrode made using iron nitrate (black). 21-layer electrodes were made using 0.029 M of iron and vanadyl acetylacetonate, and the 3-layer electrode was made using 0.2 M of iron nitrate and vanadyl acetylacetonate. Each applied layer was gelled for 10 minutes, and annealed for 10 minutes at 600 °C. Peaks indicating FTO are shown with asterisks.

The above XRD patterns show that there seems to be slight differences in the crystalline composition of the films. The pattern for the conventional 3-layer film shows peaks corresponding to triclinic iron vanadate (10.2°, 13.9°, 16.6°, 17.6°, 20.3°, 25° and 27.8° 2θ) and the conductive tin oxide layer (26.5°, 33.8°, 38°, 51.7°, 61.8° and 65.8° 2θ). In the 21 layer iron nitrate electrode (*red*), the peaks are more intense, and there are additional peaks corresponding triclinic iron vanadate (10.2°, 13.9°, 16.6°, 17.6°, 20.3°, 22.8°, 25°. 27.2°, 27.8°, 29.3°, 30.5°, 35.7°, 40.5° and 41.8° 2θ). Peaks for the tin oxide conductive layer are observed. The most likely reason for the additional triclinic iron vanadate peaks being present is that more material is present or the material is more crystalline due to more annealing cycles. Both of these factors would mean that

peaks increase in intensity and would explain the emergence of bands that were previously too weak to be observed. The two 21-layer electrode films made using iron ethoxide gave mostly very similar peaks as the others, however, there are some differences. Triclinic iron vanadate peaks are again observed (10.2°, 13.9°, 14.1° (*green only*), 16.6°, 17.6°, 20.3°, 22.8°, 25°. 27.4°, 27.8°, 29.3°, 30.5°, 34.7°, 39°, 40.5°, 41.6° and 41.8° 2θ), as are the expected peaks for the tin oxide conductive layer. However, it can also be seen that there are additional peaks observed on the films at 9°, 12° and 13° 2θ (*blue*) and at 13° 2θ (*green*). There is a possibility that the main peak at 13° 2θ, may correspond to monoclinic ($Fe_2V_4O_{13}$).[40]

5.10.2.3 – Elemental analysis of film composition by EDX

EDX was used in order to observe atomic composition at the surface of the film. The extended annealing of the films could cause enrichment of some elements at the surface, contrary to the 1:1 ratio of the original sol.[31] On the films made using iron ethoxide, slightly more vanadium was observed, than iron, with a ratio of *ca.* 3:2, whereas for the electrodes made using iron nitrate had a much closer vanadium:iron ratio of *ca.* 1.1:1.

5.10.2.4 – Optical properties of ethoxide-based films

The iron vanadate electrodes made using iron nitrate and iron ethoxide were analysed using diffuse reflectance UV/Vis spectroscopy, in order to observe any absorbance differences between the films and also to derive Tauc plots to gain information as to the nature of the band gaps. The derived Tauc plots are shown in figure 5.49.

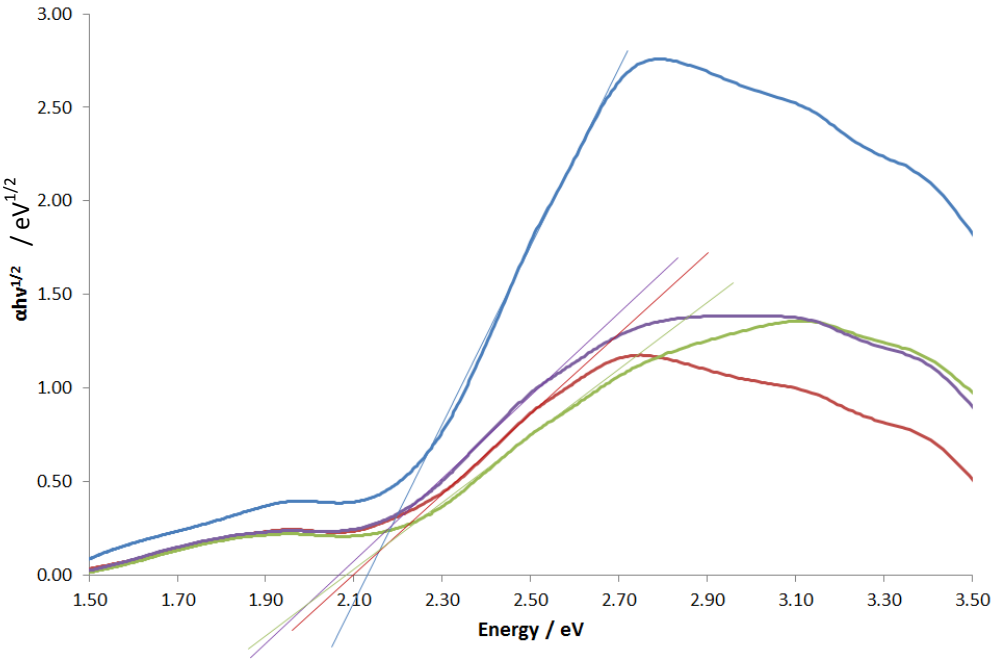

Fig. 5.49 –Tauc plots of 21-layer iron vanadate electrodes made using iron ethoxide (purple and green), 21-layer electrode made using iron nitrate (red) and a 3-layer electrode made using iron nitrate (blue). 21-layer electrodes were made using 0.029 M of iron and vanadyl acetylacetonate, and the 3-layer electrode was made using 0.2 M iron nitrate and vanadyl acetylacetonate. Each applied layer was gelled for 10 minutes, and annealed for 10 minutes at 600 °C.

The above Tauc plots all show that the iron vanadate has an indirect band gap of *ca.* 2.1 eV. There is a noticeable increase in absorbance for the film containing 3-layers (dark blue). This is possibly due to the scattering effect observed in fig. 5.33, for the films containing increasing layers. In the case of the 21-layer films, prolonged heating cycles from increasing layers could cause particle sizes in the initial layers to increase and alter the scattering.

5.10.2.5 – Ethoxide-prepared electrodes: photo-electrochemical characteristics

Photo-electrochemical measurements were taken from the iron vanadate electrodes made using iron ethoxide and iron nitrate, in order to observe whether using iron ethoxide increases or decreases the produced photocurrent, and also to observe the effect of using less concentrated sols, but a theoretically similar quantity of deposit, on produced photocurrents. The obtained *j/v* plots are shown in figure 5.50.

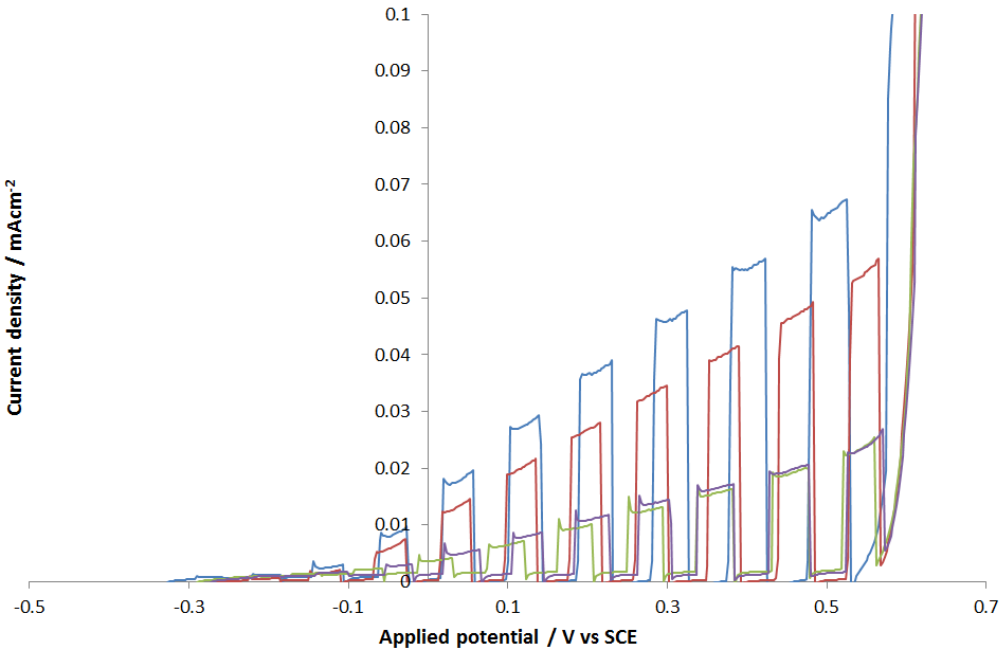

Fig. 5.50 – *j/v* plots of iron vanadate electrodes made using iron nitrate, containing 3 layers (0.2 M sol) (*blue*), 21 layers (containing 0.029 M concentration of iron nitrate) (*red*), and electrodes made using iron ethoxide (0.029 M sol) (*green* and *purple*). Electrodes were immersed in 0.5 M NaOH electrolyte and irradiated with AM1.5 light, using a scan rate 0.01 Vs^{-1}.

It can be seen from the photocurrent densities obtained that the two films made using an iron ethoxide based precursor gave similar photocurrent densities (*ca.* 0.02 $mAcm^{-2}$), which were significantly lower than those made using iron nitrate, either the 21 layer (0.029 M iron nitrate) or 3-layer (0.2 M iron nitrate), which gave photocurrent densities of 0.05 $mAcm^{-2}$ and 0.07 $mAcm^{-2}$, respectively. Both ethoxide electrodes displayed partial delamination on the edges of the film, during the measurements. This was potentially due to the increased number of annealing-cooling cycles required to make the electrodes leading to repeated expansion and contraction of the films. It should be noted that the delamination of the ethoxide-derived electrodes was significantly less than those reported in Section 5.5.

5.10.2.6 – Investigation of stability of film formation following photo-electrochemical measurements.

To assess whether or not there was an appreciable change in film composition, Raman spectroscopic analysis was conducted after photo-electrochemical measurements and compared to results in fig. 5.47.

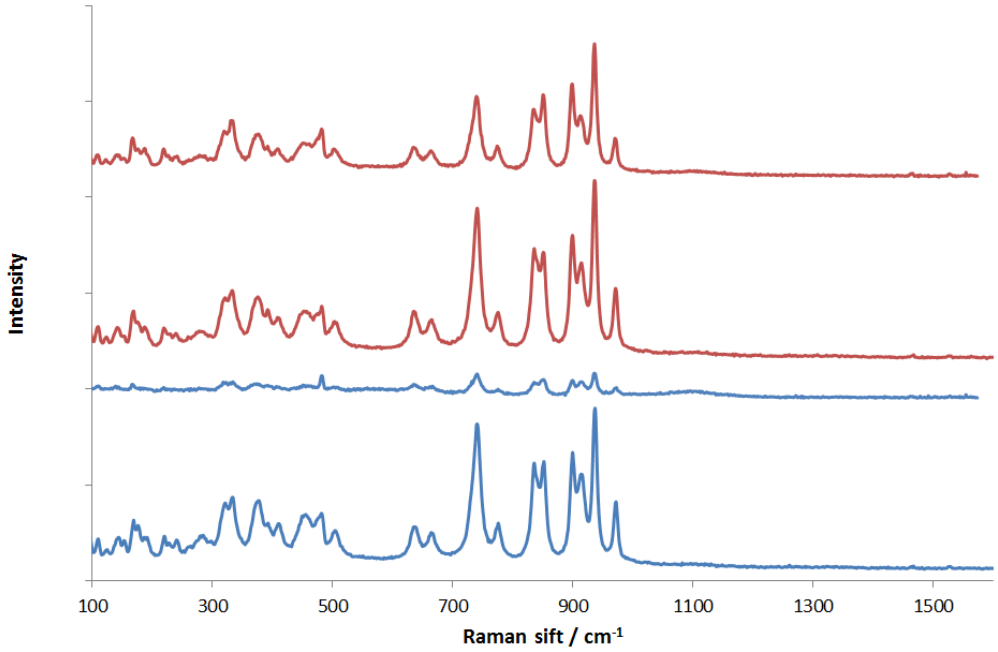

Fig. 5.51 – Representative Raman spectra of the two 21-layer iron vanadate films made using iron ethoxide at 600 °C, annealed for 10 minutes per layer (red and blue), after photo-electrochemical measurements.

There are two main observations from the above Raman spectra. Firstly, all of the peak heights seem to decrease slightly overall compared to their spectra before photo-electrochemical measurements, and secondly, the baselines decrease too, possibly indicating the loss of some material from the surface. It can also be seen that there is a degree of heterogeneity within the films, shown by the two representative spectra for each film (red and blue), possibly indicating degradation or delamination of the film.

Although the Raman spectra remain comparatively unchanged, elemental analysis was also performed by EDX. Overall this revealed a decrease in vanadium content after photo-electrochemical measurements. Indeed, the iron-vanadium ratio was much closer to 1:1 after the photo-electrochemical measurement than before, which was 3:2, V:Fe ratio. Indeed, the vanadium:iron ratio varied throughout the film, dependent on location, from 5:4 to 4:5. By comparison, the EDX of the electrodes made using iron nitrate, showed that the ratios were still close to 1:1. This suggests that electrodes prepared from iron ethoxide precursor sols yielded vanadium-rich films, possibly due to the presence of vanadium-containing compounds un-detectable by Raman microscopy that were dissolved during the photo-electrochemical measurements.

5.10.2.7 – Effect of applying an additional annealing step.

The decreased intensity observed in the Raman spectra after photo-electrochemical measurements, may have been due to a loss of crystallinity. To investigate this, an electrode containing 21 layers prepared from an iron ethoxide precursor was annealed at 600 °C for 3.5 hours, to see if this increased crystallinity and improved the photocurrents under AM1.5 illumination. The effect of this additional annealing step can be seen in the Raman spectra in fig 5.52.

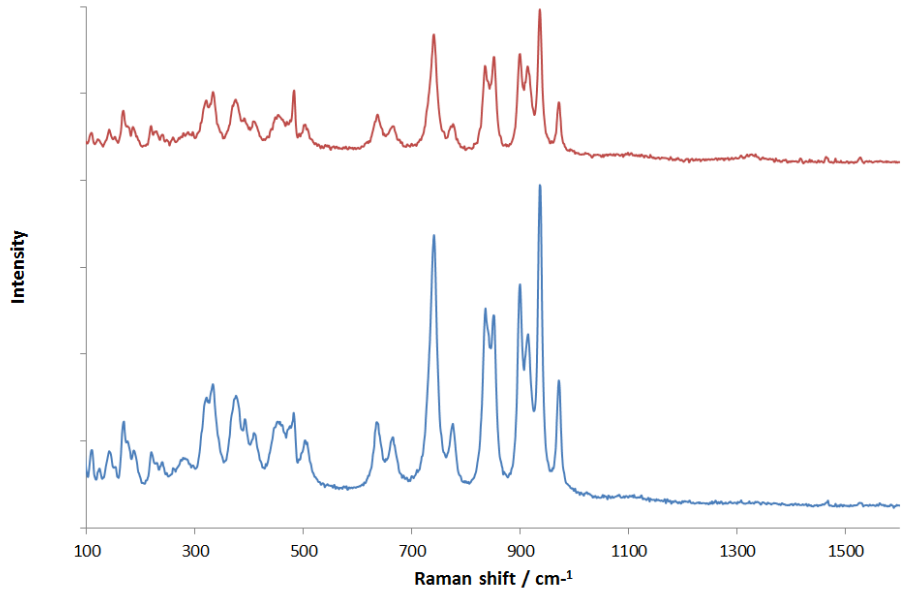

Fig. 5.52 – Representative Raman spectra of the 21-layer iron vanadate film made using iron ethoxide based precursor before (blue) and after (red) additional annealing after PEC at 3.5 hours of annealing at 600 °C.

The Raman spectra shown in figure 5.52 show that there is a significant decrease in peak intensity after the additional annealing step of 3.5 hours at 600 °C.

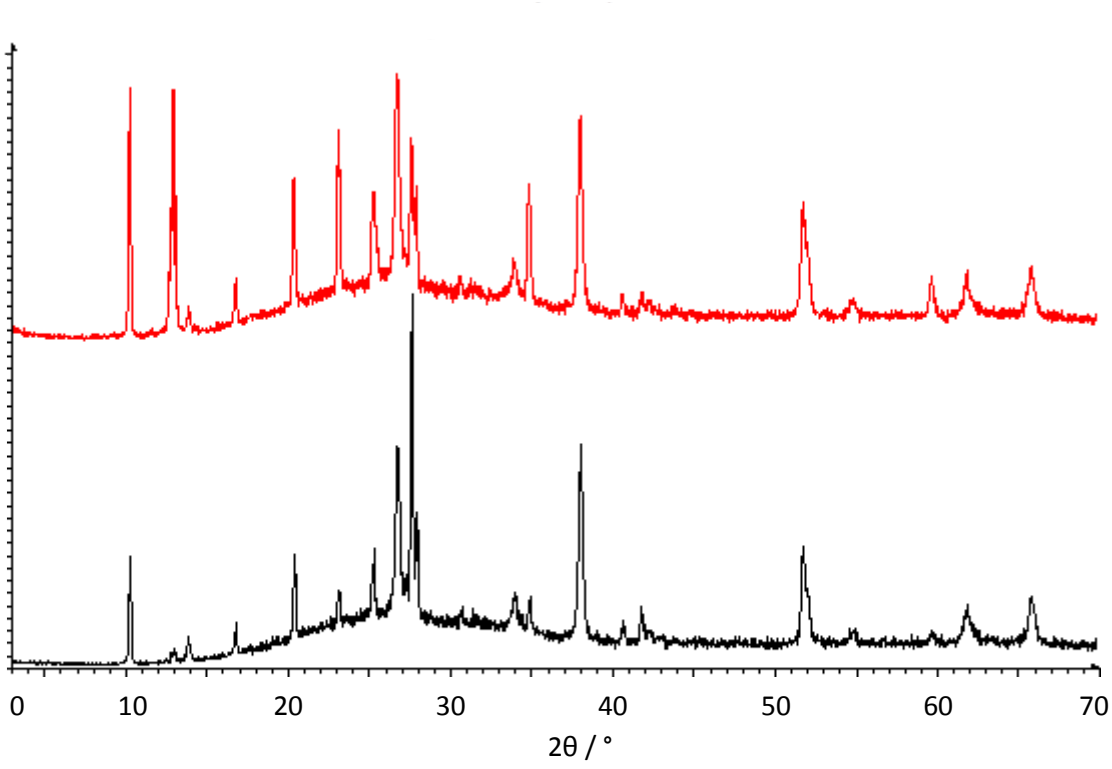

Fig. 5.53 – XRD patterns of the iron vanadate film made using iron ethoxide, after photo-electrochemical measurements (black) and then following an additional 3.5 hours of annealing at 600 °C (*red*).

On the above XRD patterns, the iron ethoxide derived electrode that was subject to an additional annealing step after photo-electrochemical measurements (*red*), showed a clearer signal from triclinic iron vanadate than in the pattern of the electrode film that was not re-annealed after photo-electrochemistry, indicating that the additional annealing increased the crystallinity of the film. Another very noticeable difference was the reduction in intensity of the peak at *ca.* 13° 2θ when not re-annealed. As explained earlier, there is a possibility that this peak may correspond to monoclinic $Fe_2V_4O_{13}$, which could explain the excess vanadium, found in the EDX analysis, as discussed in Section 5.10.2.3. The significant decrease of this peak after photo-electrochemical measurements, to a point where it is barely noticeable, does seem to also coincide with the decrease on the vanadium.

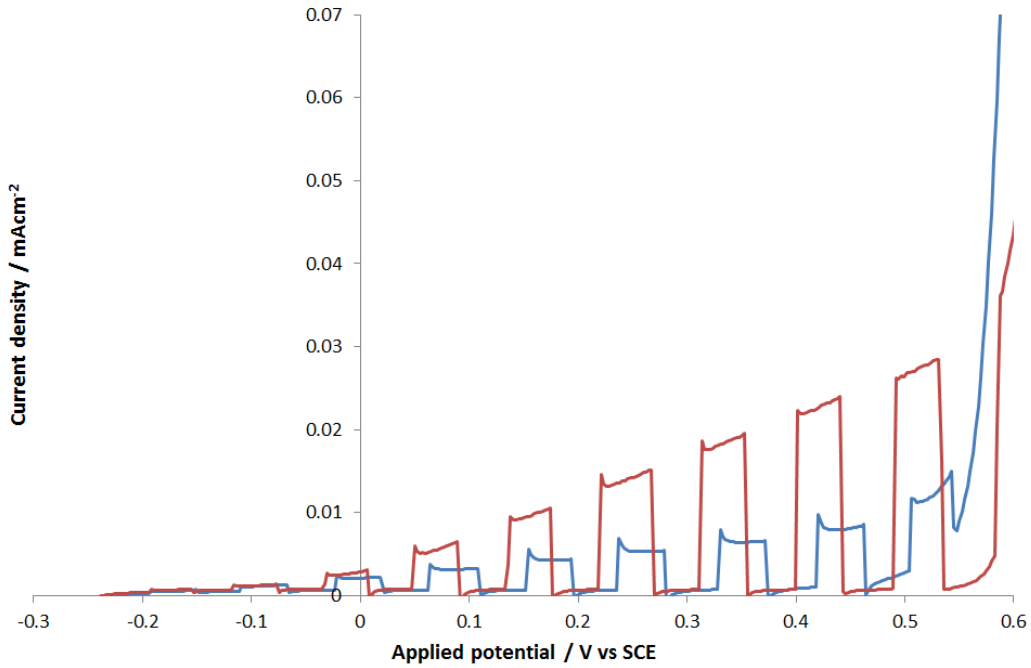

Fig. 5.54 – *j/v* plots for 21-layer iron vanadate films made using the (0.029 M) iron ethoxide based precursor. Electrodes were initially made following the annealing of each layer at 600 °C for 10 minutes in oxygen (blue). The effect of an additional annealing step of 600 °C for 3.5 hours is shown (red). Measurements were taken under exposure to AM1.5 light, in 0.5 M NaOH electrolyte, at a scan rate of 0.01 Vs^{-1}.

It is observed from the *j/v* plots above, that there is an increase in current density from the film that was subjected to the additional annealing step, compared to the original electrode (fig. 5.50), from 0.02 to 0.03 $mAcm^{-2}$at 0.5 V vs. SCE, and a decrease from the electrode which was not annealed, from 0.02 to 0.01 $mAcm^{-2}$, compared to the original electrode (fig. 5.50). Both films were subject to delamination during these measurements. Further XRD analysis of these two electrodes showed that the peak at *ca.* 13° 2θ, proposed to be from $Fe_2V_4O_{13}$[40] had diminished completely from the electrode that was subjected to an additional annealing step.

5.11 – Conclusions

The synthesis of $FeVO_4$ used herein was adapted from a reported method for $BiVO_4$.[31] Once an optimum electrode production method was established, (three layers, gelled for 10 minutes each and annealing for 10 minutes each in oxygen) investigations were undertaken to observe the film properties and performance. It was demonstrated that there is an increase in photocurrent density with annealing temperature up to

0.12 $mAcm^{-2}$ at 0.5 V vs. SCE, when annealed at 650 °C, higher than that seen for the previous films made from the iron vanadate suspension, of 0.09 $mAcm^{-2}$ at 0.5 V vs. SCE when annealed at 700 °C. It has also been shown, that these films are much more chemically and mechanically more stable than the films made in the previous chapter, but performance does decrease over 1.5 hours of constant illumination. IPCE demonstrated that a 3-layer electrode was more efficient than a 6-layer electrode, with efficiencies of up to 5.6 % compared to 3.5 % for the 6-layer film. These efficiencies are also within a similar region as reported values for $BiVO_4$ and $InVO_4$. Various factors were shown to affect the performance of the resultant film, including annealing time, sol pH, iron source, film thickness and annealing temperature. Film thickness increased fairly linearly with applied layers, however, this linearity decreased with films containing 12 and 24 layers, which also delaminated during photo-electrochemical measurements. Although there does appear to be an increase in crystallinity with applied layers, and resultantly photo-activity, the photocurrents produced from the 3-layer film (320 nm thick) and the 6-layer film (650 nm thick) were fairly similar throughout this investigation, indicating that this may be the optimum performance thickness range. Band gaps for the most crystalline films were indirect, and were in the range 2.0-2.1 eV.

5.12 – References

1. D. L. A. de Faria, S. V. Silva and M. T. de Oliveira, *Journal of Raman Spectroscopy*, 1997, **28**, 873-878.
2. S. Bencic, B. Orel, A. Surca and U. L. Stangar, *Solar Energy*, 2000, **68**, 499-515.
3. A. S. Vuk, B. Orel, G. Drazic, F. Decker and P. Colomban, *Journal of Sol-Gel Science and Technology*, 2002, **23**, 165-181.
4. M. Nohair, D. Aymes, P. Perriat and B. Gillot, *Vibrational Spectroscopy*, 1995, **9**, 181-190.
5. G. S. Li, D. Q. Zhang and J. C. Yu, *Chemistry of Materials*, 2008, **20**, 3983-3992.
6. D. L. A. de Faria and F. N. Lopes, *Vibrational Spectroscopy*, 2007, **45**, 117-121.
7. V. C. Farmer, *The Infrared Spectra of Minerals*, Mineralogical Society, Middlesex, UK, 1974.

8. C. D. Morton, I. J. Slipper, M. J. K. Thomas and B. D. Alexander, *Journal of Photochemistry and Photobiology A: Chemistry*, 2010, **216**, 209-214.

9. M. Kurzawa and E. Tomaszewicz, *Spectrochimica Acta Part a-Molecular and Biomolecular Spectroscopy*, 1999, **55**, 2889-2892.

10. L. C. Klein, *Sol-Gel technology for thin films, fibers, preforms, electronics, and specialty shapes*, Noyes Publications, New Jersey, USA, 1988

11. V. M. Sellitto, R. B. A. Fernandes, V. Barron and C. Colombo, *Geoderma*, 2009, **149**, 2-9.

12. A. A. Tahir, K. G. U. Wijayantha, S. Saremi-Yarahmadi, M. Mazhar and V. McKee, *Chemistry of Materials*, 2009, **21**, 3763-3772.

13. K. Sivula, R. Zboril, F. Le Formal, R. Robert, A. Weidenkaff, J. Tucek, J. Frydrych and M. Gratzel, *Journal of the American Chemical Society*, 2010, **132**, 7436-7444.

14. K. Sivula, F. Le Formal and M. Graetzel, *Chemsuschem*, 2011, **4**, 432-449.

15. *On Solar Hydrogen & Nanotechnology*, John Wiley & Sons, Chichester, UK, 2009.

16. R. van de Krol, Y. Q. Liang and J. Schoonman, *Journal of Materials Chemistry*, 2008, **18**, 2311-2320.

17. R. Solarska, B. D. Alexander and J. Augustynski, *Comptes Rendus Chimie*, 2006, **9**, 301-306.

18. G. Tian, H. Fu, L. Jing and C. Tian, *Journal of Hazardous Materials*, 2009, **161**, 1122-1130.

19. J.-W. Jeon, D.-W. Jeon, T. Sahoo, M. Kim, J.-H. Baek, J. L. Hoffman, N. S. Kim and I.-H. Lee, *Journal of Alloys and Compounds*, 2011, **509**, 10062-10065.

20. R. Elilarassi and G. Chandrasekaran, *Materials Chemistry and Physics*, 2010, **121**, 378-384.

21. Y. P. Xie, G. Liu, L. Yin and H.-M. Cheng, *Journal of Materials Chemistry*, 2012, **22**, 6746-6751.

22. L. Xu, X. Li, Y. Chen and F. Xu, *Applied Surface Science*, 2011, **257**, 4031-4037.

23. F. K. Urban Iii and D. Barton, *Thin Solid Films*, 1997, **308–309**, 31-37.

24. K. Joong Kim, K. T. Park and J. W. Lee, *Thin Solid Films*, 2006, **500**, 356-359.

25. Q. Zhang, X. Li and G. Li, *Thin Solid Films*, 2008, **517**, 613-616.

26. H.-L. Chen, Y.-M. Lu and W.-S. Hwang, *Thin Solid Films*, 2006, **498**, 266-270.

27. A. Zhong, J. Tan, H. Huang, S. Chen, M. Wang and S. Xu, *Applied Surface Science*, 2011, **257**, 4051-4055.

28. A. R. Shetty and A. Karimi, *Applied Surface Science*, 2011, **258**, 1630-1638.

29. H. Horvath, *Journal of Quantitative Spectroscopy & Radiative Transfer*, 2009, **110**, 787-799.

30. C. S. Enache, D. Lloyd, M. R. Damen, J. Schoonman and R. V. de Krol, *Journal of Physical Chemistry C*, 2009, **113**, 19351-19360.

31. K. Sayama, A. Nomura, T. Arai, T. Sugita, R. Abe, M. Yanagida, T. Oi, Y. Iwasaki, Y. Abe and H. Sugihara, *Journal of Physical Chemistry B*, 2006, **110**, 11352-11360.

32. M. T. Li, L. A. Zhao and L. J. Guo, *International Journal of Hydrogen Energy*, 2010, **35**, 7127-7133.

33. S. Sakka, *Handbook of sol-gel science and technology: processing, characterization and applications*, Springer, New York, USA, 2005.

34. C. J. Brinker and G. W. Scherer, *Sol-gel science: the physics and chemistry of sol-gel processing*, Gulf Professional Publishing, Oxford, UK, 1990.

35. W. Chen, L. Mai, J. Peng, Q. Xu and Q. Zhu, *Journal of Solid State Chemistry*, 2004, **177**, 377-379.

36. A. S. Tracey and D. Catharina Crans, *Vanadium compounds: chemistry, biochemistry, and therapeutic applications*, ACS, Washington DC, USA, 1998.

37. C. J. Sartoretti, M. Ulmann, B. D. Alexander, J. Augustynski and A. Weidenkaff, *Chemical Physics Letters*, 2003, **376**, 194-200.

38. C. J. Sartoretti, B. D. Alexander, R. Solarska, W. A. Rutkowska, J. Augustynski and R. Cerny, *Journal of Physical Chemistry B*, 2005, **109**, 13685-13692.

39. A. S. Vuk, B. Orel and G. Drazic, *Journal of Solid State Electrochemistry*, 2001, **5**, 437-449.

40. PDF-2 Release 2008, Kabekkodu, S.N., Ed.; International Centre for Diffraction Data: Newtown Square, PA, 2008.

6 – CONCLUSIONS

The aim of this project was to investigate the potential of a novel material for solar hydrogen production via photocatalysis. This project has involved many stages required to observe the characteristics of the new material, testing its potential for solar hydrogen generation through photo-electrochemical measurements, and attempting to alter its structure in order to improve this. Iron vanadate powder was successfully made using a low temperature aqueous synthesis, characterised using Raman spectroscopy, IR spectroscopy, XRD, UV/Vis spectroscopy and SEM and the effect of post-synthesis annealing conditions was fully investigated using the same methods. Crystallinity, band gap and particle size of the material increased with annealing temperature. At lower annealing temperatures the material is amorphous but contains VO_4 tetrahedra. At higher annealing temperatures (600-700 °C) the material was more crystalline and appeared to contain VO_4 tetrahedra, FeO_5 distorted trigonal bipyramids, FeO_6 octahedra and afforded Raman spectra that corresponded to triclinic iron vanadate. Small quantities of Fe_2O_3 were also observed in certain samples. The material annealed at these higher temperatures had an indirect band gap of *ca.* 2.00 eV.

The iron vanadate powders were applied to electrode substrates in order to observe their photocatalytic activity under simulated solar illumination. These measurements showed a significant increase in current with illumination. This photocurrent increased with annealing temperature to *ca.* 0.09 $mAcm^{-2}$ at 0.5 V vs. SCE upon annealing at 700 °C. However, these photo-active films were mechanically unstable during these measurements, indicated by significant decrease in intensity of Raman spectra recorded after photo-electrochemical measurements.

It was hypothesised that synthesising the iron vanadate directly onto the electrode may improve stability and performance. A sol containing iron and vanadium was applied to the electrode and annealed at specific temperatures. It was shown that there is an increase in photocurrent density with annealing temperature up to 0.12 $mAcm^{-2}$ at 0.5 V vs. SCE at 650 °C, higher than that seen for the previous films made from the iron vanadate suspension. It was demonstrated that the films made at the higher temperatures were more stable than previously observed, but performance decreased over 1.5 hours of

constant illumination and applied voltage. The efficiency of the films was dependent on the number of layers applied, with a 3 layer electrode being more efficient than a 6 layer electrode. IPCE measurements indicated that this efficiency decreased with increasing wavelength of applied light but, overall, was more efficient than $InVO_4$ and some $BiVO_4$ films. The production and performance of these films was dependant of a number of factors, including annealing time, sol pH, iron precursor, film thickness and annealing temperature.

Iron vanadate is a promising photo-active material with a low band gap of 2.0 eV (corresponding to a wavelength of 620 nm) which is potentially useful for solar hydrogen production. This represents the first known study of the photocatalytic potential of iron vanadate, and as a result, although preliminary measurements have shown that photocurrents and IPCE values are low compared to known photocatalysts such as TiO_2 and WO_3, with further work it will be possible to further increase the photocatalytic efficiency.

7 – FUTURE WORK

7.1 – Dopants

As stated in the conclusions, there is still scope for improvement of the photo-electrochemical response of iron vanadate, such as improved conductivity, determination of band positions and even stability. Addition of dopant elements into the precursor, and therefore the resultant film have been previously known to improve photocatalytic activity in iron oxide, by acting as hole or electron donors or traps, improving conductivity, as well as influencing band positions. The effect of adding dopants to the iron vanadate precursor on the film properties and performance could be investigated, by adding different concentrations of different elements into the sol, and observing the influence on measured photocurrents and band gap.

7.3 – Gas production

It would be interesting to observe the products formed as a result of any photochemical reactions at the surface of the films. This would be done using the same photo-electrochemical setup used for all measurements in this project, however the gas inside the sealed cell would be collected using a gas syringe. The collected gas would then be quantified via gas chromatography (GC), in order to observe and hydrogen or oxygen produced. The ratio of these gasses would indicate the stoichiometry, or otherwise, of the reaction and allow additional mechanistic data to be collated.

7.4 – Band structure

It would be interesting to determine the band energies of iron vanadate, in order to compare them to other semiconductors. This may be done using photoemission spectroscopy (PES), which can be used to analyse the density of electronic states in the material, *i.e.* probe the band structure. Computational chemistry may also be used to afford information that may otherwise be difficult to obtain experimentally. For example, density functional theory could be used, and has been previously used (by Sayama *et al. Journal of Physical Chemistry B*, 2006, **110**, 11352-11360, among others), in order to determine the composition of the valence and conduction bands.

7.5 – Role in hybrid solar cells

A solar cell converts light into electricity, as the structure of the cell causes generated electrons in the material to flow in one direction, producing a current. This structure involves an n-type semiconductor in contact with a p-type semiconductor, creating a potential difference. The two most important components of the system are for light absorption and charge transport. Hybrid cells incorporate organic polymer materials in order to improve either light absorption or charge transport. It would be interesting to implement iron vanadate into the system instead of materials with known charge transport and light absorption properties.

CONFERENCES ATTENDED

- March 2009 - *7th Spring meeting of the International Society of Electrochemistry*, Szczyrk, Poland.

  Poster presentation - Synthesis and characterisation of Iron Vanadate for solar hydrogen production

- January 2010 - *Young and Early career Researchers meeting 2010, Photochemistry group*, Durham, UK

  Oral presentation - Iron Vanadate as an alternative Photo-sensitive semi-conductor for hydrogen production

- April 2010 - *3rd Semiconductor Photochemistry Conference (SP3),* Glasgow, UK

  Poster presentation - Iron Vanadate films for Solar Hydrogen Production

- September 2010 - *TYC Energy Materials Workshop*, London, UK

  Poster presentation - Characterisation and photo-electrochemical performance of iron vanadate thin films.

- September 2010 - *SCI Photocatalysis 2010*, London, UK

  Poster presentation - Characterisation and photo-electrochemical performance of iron vanadate thin films.

- January 2011 - *UK Semiconductor Photochemistry Network Meeting*, London, UK

  Oral presentation - Characterisation and photo-electrochemical performance of iron vanadate thin films.

- May 2011 – *Colloids and Materials 2011*,
  Amsterdam, The Netherlands

  Oral presentation - Novel nanoparticulate thin film photocatalysts for solar hydrogen production.

PUBLICATIONS

C. D. Morton, I. J. Slipper, M. J. K. Thomas and B. D. Alexander, *Journal of Photochemistry and Photobiology A: Chemistry*, 2010, **216**, 209-214.